جامعة سيدي محمد بن عبد الله بفاس
UNIVERSITÉ SIDI MOHAMED BEN ABDELLAH DE FES



كلية العلوم ظهر المهراز فاس
FACULTE DES SCIENCES DHAR EL MAHRAZ FES

Order N°:56/2022

Doctoral school : Materials Sciences and Industrial Processes

Discipline : Materials Sciences

Specialty: Nanomaterials and Renewable Energy

Laboratory of Solid-state Physics

DOCTORAL DISSERTATION

Presented by

Radouane EN-NADIR

Optical Absorption in InGaN/GaN Single and Multiple Quantum Wells for Optoelectronic Applications

---

Publicly defended on 19/11/2022
in front of the review board

Jury

Pr. Izeddine ZORKANI	**USMBA, Faculty of sciences, Fez**	**President**
Pr. Ahmed SALI	**USMBA, Faculty of sciences, Fez**	**Reporter**
Pr. Khalid RAHMANI	**ENES, Rabat**	**Reporter**
Pr. Khalid BOUZIANE	**UIR, International University, Rabat**	**Reporter**
Pr. Abdellah REZZOUK	**USMBA, Faculty of sciences, Fez**	**Examiner**
Pr. Hamdi ŞÜKÜR KILIÇ	**SÜ, Faculty of sciences, Konya (Turkey)**	**Examiner**
Pr. Haddou EL-GHAZI	**UH-II, ENSAM, Casablanca**	**Co-supervisor**
Pr. Anouar JORIO	**USMBA, Faculty of sciences, Fez**	**Supervisor**
Pr. Mimouna BAITOUL	**USMBA, Faculty of sciences, Fez**	**Guest**

Academic year: 2022-2023

Acknowledgements

This thesis work was carried out in the Solid-state Physics Laboratory (LPS). I would like to thank **Pr. Anouar JORIO** and **Pr. Izeddine ZORKANI** for welcoming me to the solid-state physics laboratory and giving me the opportunity to work in an excellent team within the Nanomaterials and Renewable Energies Group (NREG) of the Physics Department of the Faculty of Sciences and for their advice and guidance during the preparation of this thesis.

I am delighted to express my sincere gratitude to **Pr. Haddou EL-GHAZI** who mentored this thesis with competence and availability. His imagination and curiosity, combined with a very broad and high cutting-edge scientific culture, allowed me to work on innovative and exciting subjects. I also thank him for giving me the opportunity to work with him. The many discussions we had, in addition to being most sympathetic and of his human character, always provided the answer to many questions that I had been asking myself for a long time.

My warmest thanks to Professors **Ahmed SALI**, **Khalid BOUZIANE** and **Khalid RAHMANI** for accepting to proofread this thesis and to be rapporteurs.

I would like to especially thank my dear Professors **Pr. Mme. Maimouna BAITOUL**, **Pr. Abdellah Rezzouk** and **Pr. Hamdi ŞÜKÜR KILIÇ** for their interest in my work by participating in the jury of this thesis and being among the examiners.

I also like to address my thanks to my dear colleagues **Walid BELAID** and **Mohamed EL-GAHOUCHI** for being always behind their screens for great scientific discussions. Thanks to the doctoral students of the laboratory of solid-state for the good atmosphere and for their sympathy, and good luck for the next ones.

My heartfelt thanks also go to the entire physics department, solid-state laboratory as well as to the FSDM/USMBA staff and administrators.

Finally, I would like to express my gratitude to my parents and my family who have always encouraged and supported me not only during my thesis, but throughout my previous years of study. I do not forget either my friends who brought me moral and intellectual support.

Absorption optique dans les puits quantiques InGaN/GaN pour l'optoélectronique

Résumé : Ce travail est consacré à l'étude des effets des excitations internes et externes (Ex: la température, la pression, l'impureté, la composition, la dimension de la structure, la géometrie du système et les champs électriques et magnétiques appliqués) sur les coefficients d'absorption optique linéaires et non linéaires (OACs) dans les puits quantiques simple et multiples à base de matériaux semiconducteurs du groupe III-V (semiconducteurs à large bande interdite: GaN, InGaN). Pour atteindre cet objectif, nous avons utilisé la méthode numérique des éléments finis (MEF) pour résoudre l'équation de Schrödinger dans les nanocristaux en tenant compte des différentes perturbations. Dans cette étude, nous avons considéré un potentiel de confinement quantique fini afin de rendre nos résulats plus réalistiques. La première partie de ce travail est consacrée à la présentation de l'état de l'art et du cadre théorique de cette étude. Cependant, dans la deuxième partie, nous avons exploré l'effet de la structure, de la taille et de la composition d'indium et de la position d'impuretés dans la structure sur l'absorption optique pour deux type de transitions optiques sous-bande(ISB) et inter-bande, BV-BC (BTB). Ensuite, nous avons montré l'effet de la température, de la géometrie du système et des champs électriques et magnétiques, et du nombre de puits quantiques par structure sur les coefficients d'absorption optique linéaire et non linéaire dans les doubles puits quantiques. Nous avons constaté que la position et l'amplitude des coefficients d'absorption optique linéaires et non linéaires dans les puits quantiques simples et doubles sont fortement influencées par les paramètres mentionnés ci-dessus. Les même résultats montrent que la structure optimale pour une grande absorption est celle des puits quantiques rectangulaires doubles (RDQW). Cependant, la plage d'énergie absorbée peut être ajustée en changeant la structure en une structure à double puits quantique parabolique ou triangulaire. De plus, il est très important de remarquer qu'un simple puits quantique parabolique inversé peut absorber plus qu'un simple puits aquatique triangulaire inversé. Cette étude sera un plus pour le dévelopement des despositifs optiques en raison que les nanostructures à double puits quantiques (DQWs) sont conçues comme étants des cavités couplées, elles consistes en l'amplification du gain optique des dispositifs à plusieurs niveaux car dans ces systèmes les fonctions d'onde se couplent pour former des mini-bandes. En raison de leur nature quasi-bidimensionnelle (2D), les électrons dans les puits quantiques ont une densité d'états en fonction de l'énergie qui a des étapes distinctes, par rapport à une dépendance de racine carrée lisse que l'on trouve dans les matériaux massifs. De plus, la masse effective des trous dans la bande de valence (m_t^*, BV) est modifiée pour correspondre plus étroitement à celle des électrons dans la bande de conduction (m_e^*, BC). Ces deux facteurs, associés à la quantité réduite de matière active dans les puits quantiques, conduisent à de meilleures performances dans les dispositifs optiques tels que les diodes laser. En conséquence, les puits quantiques sont largement utilisés dans les lasers à diode, y compris les lasers rouges pour les DVD et les pointeurs laser, les lasers infrarouges dans les émetteurs à fibre optique ou dans les lasers bleus. Ils sont également utilisés pour fabriquer des HEMT (transistors à haute mobilité électronique), qui sont utilisés dans l'électronique à faible bruit. Les photodétecteurs infrarouges à puits quantiques sont également basés sur des puits quantiques et sont utilisés pour l'imagerie infrarouge.

Mots clés : Nanosctructure, Paramètres externs, Puits quantique, Confinement quantique, Impureté-hydogènoide donneur, InN, GaN, InGaN, Transition intra-sous-bande, Transitions inter-bandes, Absorption optique.

Optical Absorption in InGaN/GaN Single and Double Quantum Wells for Optoelectronics

Abstract : This work is devoted to the study of the effects of internal and external parameters (e.g., temperature, pressure, impurity, composition, structure dimension, nanostructure shape and electric and magnetic fields) on the linear and non-linear optical absorption coefficients in single and double quantum wells based on group III-N materials. To achieve this objective, we have used the numerical method of finite elements to solve the Schrodinger equation in the nanocrystals taking into account different disturbances. In this study, we considered a finite quantum confinement potential. The first part of this work is devoted to the presentation of the state of the art and the theoretical framework of this study. However, in the second part, we explored the effect of impurity structure and size and temperature on optical absorption related to sub-subband (ISB) and inter-band (BTB) transitions.). Then, we showed the effect of the shape of the structure and of the electric and magnetic fields, and of the number of quantum wells per structure on the linear and nonlinear optical absorption coefficients in the double quantum wells. We have found that the position as well as the amplitude of linear and nonlinear optical absorption coefficients in single and double quantum wells are greatly influenced by the parameters mentioned above. The same obtained results show that the optimal structure for a large absorption is that of double rectangular quantum wells (RDQW). However, the range of energy absorbed can be adjusted by changing the structure to a double parabolic or triangular quantum well structure. In addition, it is very important that a simple inverted parabolic quantum well can absorb more than a simple inverted triangular aquatic well. This study will be a plus for the development of optical devices because the double quantum well nanostructures (DQWs) are designed as a coupled cavity, which consists of the amplification of the optical gain of the devices at several levels because in these systems the wave functions couple to form mini-bands. Due to their quasi-two-dimensional (2D) nature, electrons in quantum wells have a density of states as a function of energy that has distinct steps, with respect to a smooth square root dependence found in massif materials. Additionally, the effective mass of holes in the valence band (m_h^*, VB) is changed to more closely match that of electrons in the conduction band (m_e^*, CB). These two factors, together with the reduced amount of active material in quantum wells, lead to better performance in optical devices such as laser diodes. As a result, quantum wells are widely used in diode lasers, including red lasers for DVDs and laser pointers, infrared lasers in fiber optic transmitters, or in blue lasers. They are also used to make HEMTs (high electron mobility transistors), which are used in low noise electronics. Quantum well infrared photodetectors are also based on quantum wells and are used for infrared imaging.

Keywords : Nanosctructure, External parameters, Quantum well, Quantum confinement, Impurity-donor hydogènoide, InN, GaN, InGaN, Intra-subband transition (ISB), Band-to-band transition (BTB), Optical absorption.

Contents

Acknowledgements iii

Introduction and context 1

1 Wide-band-gap semiconductors and the theory of optical transitions in QWs 9
1.1 Introduction . . . 11
1.2 Structural proprieties . . . 11
1.2.1 Crystalline structure . . . 11
1.2.2 Band structures of GaN and InN . . . 13
1.2.3 Band-gap parameters . . . 13
1.3 Piezo-electric and spontaneous polarization in III-N semiconductors . . . 15
1.3.1 Spontaneous polarization . . . 15
1.3.2 Piezo-electric polarization . . . 17
1.3.3 Total polarization . . . 18
1.4 From bulk material to low-dimensional systems . . . 18
1.5 Elaboration methods for III-nitrides growth . . . 20
1.5.1 Metallo-organic vapor phase epitaxy (MOCVD) . . . 21
1.5.2 Molecular beam epitaxy (MBE) . . . 21
1.6 Theory of quantum confinement in QWs . . . 22
1.6.1 Quantum confinement . . . 23
1.6.2 Quantum wells (QWs) . . . 23
1.6.3 Theoretical model of a single QW . . . 25
1.6.4 Optical transitions in QW . . . 28
1.6.5 Envelope function approximation . . . 28
1.7 Optical absorption coefficient . . . 29
1.8 Conclusion . . . 31

2 BTB and ISB optical absorption in single QW: Size, In-composition and impurity effects 33
2.1 Introduction . . . 35
2.2 Theoretical framework . . . 35
2.3 Optical properties in single QW . . . 37
2.3.1 ISB and BTB electron transition energy in single QW . . . 38
2.3.2 Dipole matrix-element in single QW . . . 39
2.3.3 Optical absorption in single QW . . . 40
2.3.3.1 ISB optical absorption . . . 41
2.3.3.2 BTB optical absorption . . . 43
2.4 Optical absorption and refractive index in IPQW and ITQW . . . 45
2.4.1 Shape and In-composition effects . . . 46
2.4.1.1 Electron wave functions . . . 46
2.4.1.2 Electron transition energy . . . 47
2.4.2 Optical absorption and refractive index change . . . 48
2.5 Conclusion . . . 50

3 ISB optical absorption in RDQW: Coupling and temperature effects 53
3.1 Introduction . . . 55
3.2 Theoretical framework . . . 55
3.3 Temperature and coupling effects . . . 57
3.3.1 Electron wave functions . . . 57
3.3.2 Electron energy levels . . . 58
3.3.3 Electron transition energy . . . 60
3.3.4 The oscillator strength . . . 61
3.4 ISB total optical absorption . . . 63
3.5 Conclusion . . . 65

4 ISB optical absorption in PDQWs: The temperature, In-compositions, impurity and size effects 67
4.1 Introduction . . . 69
4.2 Theoretical background . . . 69
4.3 The effects of temperature, In-compositions, impurity and coupling . . . 70
4.3.1 Electron wave functions and energy levels . . . 70
4.3.2 Electron transition energy . . . 72
4.3.3 Dipole matrix element . . . 72
4.4 Total optical absorption coefficient . . . 73
4.5 Conclusion . . . 76

5 ISB optical absorption in DQWs: Shape, Number of QWs, Asymmetry and Electric and magnetic fields effects 77
5.1 Introduction . . . 79
5.2 Theoretical background . . . 79
5.3 Potential barrier shape effect . . . 79
5.3.1 Electron wave functions . . . 80
5.3.2 Electron transition energy . . . 80
5.3.3 ISB optical absorption coefficients . . . 81
5.4 Number of QWs per nanostructure effect . . . 82
5.4.1 Number of QWs effect on GaN-based LEDs characteristics . . . 82
5.4.2 Number of QWs per nanostructure effect on OACs . . . 84
5.4.2.1 Electron wave functions . . . 84
5.4.2.2 Transition energy and dipole matrix element . . . 85
5.4.2.3 ISB optical absorption coefficients . . . 86
5.5 Structure asymmetry effect on OACs . . . 87
5.5.1 Electron wave functions . . . 87
5.5.2 Electron transition energy and dipole matrix element . . . 88
5.5.3 ISB optical absorption coefficients . . . 89
5.6 Electric and magnetic field effects on OACs . . . 90
5.6.1 Electron wave functions . . . 90
5.6.2 Electric field effect . . . 91
5.6.2.1 Electron transition energy and dipole matrix element . . . 91
5.6.2.2 ISB optical absorption coefficients . . . 92
5.6.3 Magnetic field effect . . . 93
5.6.3.1 Electron transition energy and dipole matrix element . . . 93
5.6.3.2 ISB optical absorption coefficients . . . 94
5.7 Conclusion . . . 96

Conclusion and perspectives 97

Bibliography **101**

A Numerical method and approaches **113**
A.1 Finite difference method or FDM 113
A.2 Numerical solution of the uni-dimensional Schrodinger's equation 114
A.2.1 Case 1: In the barrier region (GaN) 115
A.2.2 Case 2: In the well region (InGaN) 116
A.2.3 Case 3: At the interface between well/barrier (GaN/InGaN) . . . 117
A.3 Software: *Python* 119

List of publications and conferences **121**
I Publications 121
Articles in peer-reviewed journals 121
Articles in peer-reviewed conference proceedings 122
II Conferences 123
Oral Presentations 123
Presentations by Poster 125

List of Figures

1 Band gap versus lattice constant of group III- Nitride material systems[91]. 2

1.1 Mondeliev's periodic table: showing different III-N compound(original version has been modified) [83]. 11
1.2 (a) Wurtzite and (b) zinc-blende crystallographic structures of GaN [55]. 12
1.3 (a) Wurtzite unit cell (Hexagonal) and (b) atomic structure of binary nitrides M (M = Al, Ga, In) - and N-polar [18]. 12
1.4 Calculated band structure of wurtzite binary nitrides: (a) AlN; (b) GaN; (c) InN [18]. 13
1.5 QD band gap energy for some common semiconductors versus the QD's size [43]. 14
1.6 Illustration of the polar (0001), non-polar (1-100) and (11-20), and semipolar (1-103) and (11-22) planes (modified from [14]). 15
1.7 The orientation of the plane (hkl) in the frame of the crystallographic axes of the hexagonal lattice (left) and in the Cartesian frame defined by the vectors ($\vec{U}$,$\vec{V}$,$\vec{W}$) [71]. 16
1.8 The schematic representation of the atomic planes ABAB on the direction $\vec{c}$ [11]. 16
1.9 Schematic description of the confinement effect of carriers, on the density of state and the electronic structure of bands in: (a) a 3D bulk material, (b) a 1D quantum well, (c) a 1D quantum wire, (d) a quantum dot (modified from) [90]. 19
1.10 Schematic description of band diagram and the absorption/relaxation mechanisms in: (a) Bulk material, (b) Quantum well [43]. 20
1.11 Schematic discreption of MOCVD method [77]. 21
1.12 schematic patterned growth process on a self-supporting GaN lattice by molecular beam epitaxy (MBE) [82]. 22
1.13 Representation of the different types of quantum wells [15]. 24
1.14 Schematic representation of the band diagram of a quantum well (modified from [15]). 25
1.15 Representation of a **finite** rectangular potential. 26
1.16 Profile of a quantum well formed by two different band gap energy materials **A** and **B**: On the left (interband transition); Right (intra-subband transition) [69]. 28

2.1 Schematic representation of different optical transitions in SQW with a finite potential barrier: ISB (Red narrows) and BTB (Black narrows). The excitation comes from $z = 0$. 36
2.2 The variation of the difference energies between the bound electronic-states in single QW versus the well width under the effects of the barrier width, the In-concentration, and the impurity-position in the structure [30]. 38
2.3 The dipole matrix-element as a function of the (GaN/(In,Ga)N/GaN QW thickness for two different values of the $In-$compositions, barrier's size, and impurity's position.[30]. 40

2.4 Conduction Band of a ($GaN/InGaN/GaN$) single QW structure showing the energy levels and possible ISB optical transitions (the original figure has been modified).[19]. 41
2.5 The change of the total optical absorption spectra of BTB transition as a function of the incident photon energy of InGaN/GaN single QW under the effects of In-compositions, size and impurity.[30]. 42
2.6 The change of the total optical absorption spectra of BTB transitions as a function of the incident photon energy of InGaN/GaN single QW under the effects of In-compositions, size and impurity.[30]. 44
2.7 The confinement potential profile as well as the square of lowest and two low-laying electron wave-functions versus z-axis for three different values of $\Omega = (4, 2, 1)$ considering two QW's shapes: ITQW and IPQW . 47
2.8 The variation of the lowest and two low-laying energy levels in both ITQW and IPQW versus the well width (x-axis) and temperature ($y - axis$) with a fixed barrier width ($L = 2$) and $x_{max} = 0.2$ for three different values of $\Omega = (4, 2, 1)$ 48
2.9 The variation of the optical absorption coefficients ($(\alpha^1), (\alpha^3)$ and (α^t)) versus the incident photon energy for three different values of $\sigma = (2, 1.82; 1.67)$ in single PQW taken into account the well thickness effect 49
2.10 The variation of the refractive index change (RIC) versus the incident photon energy for three different values of $\sigma = 2(1.82; 1.67)$ in single PQW taken into account the well thickness effect 49
2.11 The variation of the optical absorption coefficients ($(\alpha^1), (\alpha^3)$ and (α^t)) versus the incident photon energy for three different values of $\Omega = (2, 1.8; 1.7)$, two types of potential profile have been considered: IPQW (left) and ITQW (right) 50
2.12 The variation of the optical absorption coefficients ($(\alpha^1), (\alpha^3)$ and (α^t)) versus the incident photon energy. Two effects have been considered: Potential profile shape (a) and incident electromagnetic intensity (b) . . . 50

3.1 Schematic diagram of a symmetric unstrained GaN/InGaN SDQWs. . . . 55
3.2 Energy levels as well as their associated wave-functions in symmetric $GaN/In_xGa_{1-x}N$ coupled double quantum wells (RDQWs) as a function of the growth direction for two values of temperature: 100K (left-panel) and 500K (right-panel) with $l = 2L = 2a_b^*; W = 0.2a_b^*; x = 20\%$[29]. 58
3.3 Energy levels of lowest and five low-lying states as a function of the well width (a), Coupling barrier width (b) and extreme barriers width (c) for InGaN/GaN based DRQWs. The effect of temperature is included [Solidlines: T=100K; Doshedlines: T=500K][29]. 59
3.4 Energy difference between the allowed states as a function of the well width (a), central barrier width (b) and extreme barriers width (c) for InGaN/GaN based DRQWs. The effect of the temperature is considered. [Solidlines: T=100K; Doshedlines: T=500][29]. 60
3.5 Oscillator strength of different allowed transitions as a function of the well width (a and d), central barrier width (b and e) and extreme barriers width (c and f) for InGaN/GaN based DRQWs for two different values of the temperature. [Solidlines: T=100K; Doshedlines: T=500][29]. 62
3.6 2s-2p, 2p-3s, 3s-3p and 3p-3d related total optical absorption as a function of the photon energy for InGaN/GaN based DRQWs for two different values of temperature. The geometrical coupling barrier width impact is introduced.[29]. 64

3.7 1s-2p, 1s-3p, 2s-3p, and 2p-3d related total optical absorption according to the photon energy for InGaN/GaN based DRQWs for two different values of the temperature and two different values of the geometrical coupling barrier width. The 1s-2p and 1s-3p intesubband transitions TOAC are multiplied by 50 for more clarity.[29]. 65

4.1 The electron probability densities of the ground and first excited state versus the growth direction with $x = 0.1, l = L = 1$, the coupling and impurity effects are included: Panels (a) and (b) depicted for on center impurity and panels (c) and (d) presented for W=0.5. 70
4.2 The variation of the energy level of the fundamental $E_0(1s - state)$ and second excited electronic-state $E_2(2p - state)$ versus temperature and well thickness in symmetric InGaN/GaN PQQWs for $x = 0.1, W = 0.5, L = 2$ with the presence of an on-center impurity [28]. 71
4.3 The variation of difference energy between (E_0) and (E_2) levels as a function of temperature and well thickness in symmetric InGaN/GaN DPQWs for $x = 0.1, W = 0.5, L = 2$ with the presence of an on-center impurity [28]. 73
4.4 The variation of the square of the dipole transition element matrix between $1s$ and $2p$ as a function of the well width (a) and the indium concentration (b) in symmetric InGaN/GaN DPQWs: The effects of the coupling barrier width (a) and temperature (b) are reported. (a.u signify arbitrary unit) [28]. 74
4.5 The variation of $\alpha^{(Tot)}$ versus incident photon energy $(\hbar\omega)$ in symmetric PDQWs for $L = 2l = 2$ and $x = 20\%$: The effect of temperature is shown in panel (a) and that of coupling in panel (b) [28]. 75
4.6 The variation of $\alpha^{(Tot)}$ versus incident photon energy $(\hbar\omega)$ in symmetric PDQWs for $L = 2l = 4W = 2$ and $T = 300K$: The effect of In-composition is shown in panel (a) and that of impurity in panel (b) [28]. 76

5.1 The potential profile, $V(z)$, and the electron probability densities of the ground and two low-laying states as a function of the growth direction $(z - axis)$ for $L = 0.5, l = W = 1$ and $x = 0.2$ taking into account three different confinement profile: RDQW(left), PDQW(middle) and TDQW(right) 80
5.2 The variation of the transition energy between 1s-2p levels (E_{20}) as a function of coupling barrier with (W) for three different confinement profile: RDQW(blue), PDQW(green) and TDQW(red) 81
5.3 The variation of OACs as a function of the incident photon energy $(\hbar\omega)$ taking into account the effect of the potential profile 82
5.4 Example of the optical intensity of an LED in (In,Ga) depending on the intensity of the electric current and the number of quantum wells [59]. . 83
5.5 Dark current level at fixed bias (0.9 V) as a function of quantum well number [17]. 83
5.6 The schematic diagram of single and double QWs and the probability densities associated with the ground and two lowest-excited electronic states as a function of growth direction considering three different potential barrier: SQWs, panel (a, b, c) and DQWs, panels (d, e, f). 85
5.7 The variation of E_{20}, panel (a) and the $|M_{20}|^2$ in single and double QWs as a function of QW-thickness for three different nanostructures: The effect of number of QW per nanostructure is considered. 86

5.8 The variation of OACs versus the incident photon energy ($\hbar\omega$) for three different systems taking into account the effect of number of the QWs per nanostructure. 87
5.9 The schematic diagram of $V(z)$ and the probability densities of the ground ($1s$) and the two lowest excited electron states (i.e.,$2s, 2p$) as a function of the growth direction for three different nanostructure shapes: RDQW, PDQW and TDQW. 88
5.10 The variation of E_{20}, panel (a), and $|M_{20}|^2$, panel (b) with respect to the right QW's thickness (W) for three different nanostructure shapes: RDQW, PDQW and TDQW 89
5.11 The variation of OACs versus the incident photon energy considering the asymmetry effect for three different nanostructure shapes: RDQW, PDQW and TDQW 89
5.12 The schematic diagram of $V(z)$ and the probability densities of the ground ($1s$) and the lowest excited electron states (i.e.,$2s, 2p$) as a function of the growth direction considering the effects of the electric (μ) and magnetic (γ) fields for three different nanostructures: RDQW, PDQW and TDQW. 91
5.13 The variation of E_{20}, panel (a), and $|M_{20}|^2$, panel (b) according to the electric field intensity (μ) for three different nanostructures: RDQW, PDQW and TDQW 92
5.14 The variation of optical absorption coefficients versus the incident photon energy considering the electric field intensity effect (μ) for three different nanostructures: RDQW, PDQW and TDQW 93
5.15 The variation of E_{20}, panel (a), and $|M_{20}|^2$, panel (b) according to the magnetic field intensity (γ) for three different nanostructures: RDQW, PDQW and TDQW 94
5.16 The variation of optical absorption coefficients versus the incident photon energy considering the magnetic field intensity effect (γ) for three different nanostructures: RDQW, PDQW and TDQW 95

A.1 The finite difference method relies on discretizing a function on a grid. Ref:`https://en.wikipedia.org/wiki/Finite_difference_method` 113
A.2 A schematic representation of a single quantum well (SQW) made out of InGaN (well region) and GaN (barriers region). 114
A.3 Energy-levels of the first six-levels and their associated wave-functions in symmetric single InGaN/GaN quantum well. 119

List of Tables

1.1 Lattice parameters of bulk wurtzite GaN and InN at room temperature. [55, 60]. 12
1.2 Band-gaps and effective masses of GaN and InN at T=0K [55, 4, 52]. . . . 14
1.3 The piezoelectric coefficients for certain III-nitride(wurtzite) semiconductors [34]. 18

2.1 Band-gaps, effective masses and dielectric constants of GaN and InN at T=0K [55, 4]. 35
2.2 Table of the physical constants 46

3.1 The effect of the coupling and temperature on ISB total optical absorption coefficient. 66

5.1 The dependence of solar cell characteristics on the QW's number [17] . . 84

List of Abbreviations

ISB	**I**ntra-**S**ubband **T**ransition
BTB	**B**and-**T**o-**B**and transition
LDS	**L**ow- **D**imentional **S**ystem
QW	**Q**uantum **W**ell
SQW	**S**ingle **Q**uantum **W**ell
DQW	**D**ouble **Q**uantum **W**ell
RDQW	**R**ectangular **D**ouble **Q**uantum **W**ell
PDQW	**P**arabolic **D**ouble **Q**uantum **W**ell
TDQW	**T**riangular **D**ouble **Q**uantum **W**ell
PQW	**P**arabolic **Q**uantum **W**ell
ITQW	**I**nversed **T**riangular **Q**uantum **W**ell
IPQW	**I**nversed **P**arabolic **Q**uantum **W**ell
DCQW	**D**ouble **C**oupled **Q**uantum **W**ell
OAC	**O**ptical **A**bsorption **C**oefficient
LOAC(α^1)	**L**inear **O**ptical **A**bsorption **C**oefficient
NLOAC(α^3)	**N**onlinear **O**ptical **A**bsorption **C**oefficient
TOAC(α^{Tot})	**T**otal **O**ptical **A**bsorption **C**oefficient
RI	**R**efractive **I**ndix
MOCVD	**M**etal **O**rganic **C**hemical **V**apor **D**eposition
LPE	**L**iquid **P**hase **E**pitaxy
PLD	**P**ulsed **L**aser **D**iposition
LED	**L**ight **E**mission **D**iode
FEM	**F**inite **E**lement **M**ethod
DEM	**D**ipole **E**lectric **M**oment
N	**N**itride
In	**I**ndium
Ga	**G**allium
GaN	**G**allium **N**itride
InN	**I**ndium **N**itride
InGaN	**I**ndium **G**allium **N**itride
GaAs	**G**allium **A**rsenide
AlAs	**A**luminium **A**rsenide
GaP	**G**allium **P**hosphorus
InSb	**I**ndium **A**ntimonide
InP	**I**ndium **P**hosphorus
InAs	**I**ndium **A**rsenide

List of Symbols

T	temperature, K
P	pressure, bar
μ	electric field, V/m
γ	magnetic field, T
a	mesh parameter, m
a^*	Effective Bohr radius, nm
R^*	Effective Rydberg energy, meV
ω	pulsation, rad s^{-1}
k	wave vector, m^{-1}
λ	wavelength, m
t	time, s
m	mass, kg
z	position, m
x	concentration/composition/content/fraction/percentage %
ρ	density, kg m^{-3}
ν	frequency, Hz
k_B	Boltzmann's constant, J K^{-1}
$\hbar$	reduced Planck constante, J s
θ_D	temperature of Debye, K
q	electron charge, C
I_0	intensity of incident photons at the equilibrium, W m^{-2}
I	intensity of incident photons, W m^{-2}
τ	relaxation's time, s
L	characteristic dimension (barrier-width), m
l	characteristic dimension (well-width), m
W	characteristic dimension (coupling-barrier-width), m
$\alpha^{(1)}$	linear optical absorption coefficient, cm^{-3}
$\alpha^{(3)}$	nonlinear optical absorption coefficient, cm^{-3}
$\alpha^{(Tot)}$	total optical absorption coefficient, cm^{-3}
i	descretization-step
n	number of steps

I dedicate this thesis to my parents for their love and sacrifices...
*"**Life is either a daring adventure or nothing at all So, work smart not hard and never let your daily routine take over your real life**"*
Dr. Radouane En-nadir

Introduction and context

The semi-conductor group of III-nitrides is widely used in many areas of our modern life: lasers, ultraviolet detectors,light-emitting diodes (LEDs), high electron mobility transistors (HEMTs)... and it is only the beginning of the list of all their possible applications. Before starting the exploitation of nitride-based materials, it was necessary to deeply understand their properties and solve several material problems to create operational electronic and optoelectronic devices.

The fabrication of GaN was first reported by Johnson et al. in 1931 who heated pure gallium with ammonia to create powdered GaN[44]. In 1969, Maruska and Tietjen developed a method to grow crystalline GaN on sapphire using hydride vapour phase epitaxy (HVPE) which uses a reactor with varying temperature zones[57]. They estimated the value of its direct band gap $E_g = 3.39eV$ and carrier concentration about $n = 10^{19}cm^{-3}$ for an undoped GaN layer. Such a high value of background n−doping has been attributed throughout to a high density of nitrogen vacancies. Different methods have been used to improve the structural quality of GaN films. The most effective one was proposed by Nakamura et al. and included the growth of a GaN buffer layer at low temperature to filter the dislocations formed at the GaN/sapphire interface. This method led Nakamura et al. to achieve a very high electron mobility up to $900cm^2/V_s$ and a relatively low background electron concentration $n \approx 2 \times 10^{16}cm^{-3}$[65]. Despite the quality improvement, it was still difficult to obtain p-type conductivity in GaN-samples. This fact has been explained by the impact of hydrogen which forms acceptor-H complexes in the p-doped GaN film resulting hole compensation[62]. Post-growth thermal annealing of Mg-doped GaN samples under N_2 technique was used to destroy these complexes which makes it possible to reach a low hole mobility of $10cm^2/V_s$ and a high hole concentration $p = 3 \times 10^{17}cm^{-3}$[63]. The success of n- and p-type GaN layer growth led Amano et al. to demonstrate the first LED-based on a GaN n-p junction[2]. Later, GaN-based LED was further improved by inserting a thin

layer of InGaN between the n- and p-GaN. In 1995, Nakamura et al. demonstrated LEDs-based on a single InGaN quantum well and emitting different colors (blue, green and yellow)[64]. They have demonstrated that the colors can be adjusted by changing the In-composition from 20 to 70% in the InGaN alloy. In 2014, S. Nakamura, H. Amano and I.Akazaki have won the Nobel prize "for their invention of efficient emitting diodes which has enabled bright and energy-saving white light sources". Currently, InGaN is the most usual materials used in modern blue and green LEDs.

A long time ago, it was believed that the InN band gap is 1.9 eV. However, in 2002 several studies confirmed that the band gap is close to 0.7 eV[23, 85]. It means that InGaN-based heterostructures are one of a few systems that can provide a band gaps from 0.7 (InN) to 3.4 eV (GaN). The band gap adjustment could be realized directly by changing In-concentration in the InGaN alloys. Fig.1 shows the band gap energy variation versus lattice constant for different III-N known semiconductors. From this figure (Fig.1), it can be seen that InGaN-based systems can cover almost the entire visible spectrum. Therefore, InGaN alloys could be perfect candidates for solar cell applications. In addition to good band gap covering most of the solar spectrum, InGaN alloys have

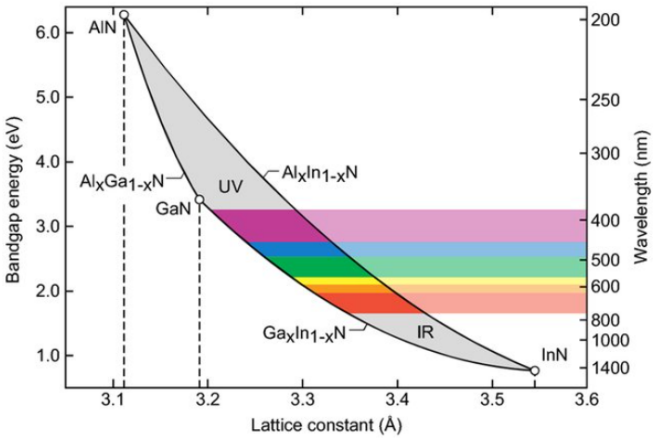


FIGURE 1: Band gap versus lattice constant of group III- Nitride material systems[91].

other advantages to be applied in solar cells. Due to a direct band gap, the absorption coefficient of InGaN alloys is very high and reaches $10^5 cm^{-1}$ for photon energy of 0.5 eV above the absorption edge for all ranges of In-compositions[85]. Moreover, Wu et al. showed that the optical and electronic properties of InGaN alloys have a significant resistance to high-energy photon irradiation (up to 2 MeV), which is much better than what is currently used in GaAs and GaInP solar cell materials [86]. This makes InGaN

a great candidate in the radiation hard-solar cells for space applications. Shen et al. demonstrated that InGaN alloys have a high thermal stability of the optical and electrical properties which makes possible the use of this material in solar cells that work under concentrated lighting[75]. In addition, Hsu et al. have shown that adding the $In_{0.46}Ga_{0.54}N$ p-n junction to the Si p-n solar cell can improve the power conversion efficiencies by over than 50% compared to a Si-only solar cell (27% vs. 17%). Moreover, the alignment of the Si valence band with the In0.46Ga0.54N conduction band avoids the need for heavy doping at the heterointerface of InGaN/Si systems[41]. Despite all the advantages listed above, the very poor quality of In-rich InGaN layers limits its evolution in the solar cell market. This degradation in quality is related to the characteristics of InGaN material listed here after.

Unfortunately, one of the most known challenge in InGaN systems is that there is no specific lattice substrate for growing InGaN III-nitrides and sapphire remains the most usually used. Nevertheless, a large lattice mismatch (29% between InN and sapphire and 14% between GaN and sapphire) creates many defects in the InN/sapphire, GaN/sapphire interfaces damaging the material quality. The thick template layer of GaN is usually developed to match different materials by dislocation bending and annihilation. Although the lattice mismatch between GaN and InN is lower (only 10%) compared to InN/sapphire and GaN/sapphire, it is still sufficient to cause stresses at the InGaN/GaN interface[56]. There is a critical thickness for InGaN layers above which stresses are released forming dislocations. This critical thickness is much lower for InGaN grown on GaN-substrate and it is less than 5 nanometers for In-compositions greater than 20%[40]. Once the critical thickness is achieved, threading dislocations are formed, damaging the device performance. These dislocations can terminate on the surface of the layer as V-defects and absorb photons above and under the InGaN bandgap, resulting in solar cell shadowing[51]. One of the possible ways to overcome this tricky problem is to replace a thick InGaN layer with multi-quantum-wells (MQWs) or superlattice (SL) keeping the QW thickness lower than the critical thickness.

Since 2010, the solar cell industry has grown rapidly at over 30% per year. But, despite the rapid increase, solar energy production represents no more than 1% of the overall energy produced. The low use of solar energy is partly related to its high cost.

The best way to reduce the cost of solar cells is to improve their performance. Currently, the photovoltaic market is dominated by crystalline silicon photovoltaic panels. However, Si-modules are limited to a maximum efficiency of 20% in production. The development of solar cells in terms of conversion efficiency has achieved great success in recent years. The highest efficiency value is obtained with III-V multi-junction solar cell under concentrated sunlight. According to the (Fraunhofer Institute for Solar Energy Systems (ISE), CEA-Leti and Helmholtz Center Berlin, Soitec,2013), the most efficient solar cell at 44.7% is owned by a four junction solar cell made of III-V semiconductors under concentrated light (297 suns). This is the closest value to the expected theoretical achievable limit of 49.5%[12]. Approaching a new record of up to 50% efficiency requires the exploration of new materials and devices design. Theoretical simulations of the multi-junction solar cells have shown that the design of four-junction device requires a material with a band gap greater than 2.5 eV[12]. Indium-gallium nitride (InGaN) has demonstrated particular properties that can be promising for its further use in photovoltaic and optoelectronic applications, in particular as a high-energy photon absorber material (>2.5 eV) in multi-junction solar cells. Despite the low quality of the InGaN layers, it slows down the development of InGaN-based photovoltaics, the electrical performance of InGaN-based solar cells can be improved by a precise choice of the design of the active region.

Due to their particular properties, coupled double quantum wells (DQWs) contain an extra degree of electronic freedom in the growth direction, giving rise to new transport phenomena not found in single-electron layers. This system holds promise for future quantum effect electronic devices, and also photonic devices based on III-V compound semiconductors InN, GaN, and InGaN. This system consists of two quantum wells separated by a narrow barrier that electrons can tunnel through. Several quantum effect devices have already been proposed for DQWs. The DQWs are no longer only promising systems for fundamental research but are definitely important for future industrial applications. On the basis of DQW systems, several nanoelectronic devices have been suggested and already realized. DQWs based on various semiconductor materials appear frequently in lasers emitting light in a wide range of wavelengths including the region 1.3-1.5 μm which is of great importance in optical communications.

DQWs are also considered effective THz detectors, see [67]. Naturally, also other applications of DQWs can be found such as InGaN-based laser diode. The purpose of this thesis is to the optimization of the optical absorption related to the ISB and band-to-band transition in single and double quantum wells by taking into account the effect of the external and internal parameters (temperature, electric field, the composition of alloys, mismatch,...) as well as the dimension and the shape of the structure and of confinement potential. The main emphasis of this work is the effect of size, In-composition, temperature, and electric field intensity on the linear and nonlinear optical absorption coefficients of single (SQW) and double coupled quantum wells (DQWs) made out of InGaN/GaN. We also, investigate the effect of the number of QWs on the linear, third-order nonlinear, and total optical absorption coefficients.
The objectives of this work are listed below:

- the optimization of the band-to-band and subband (SBT) optical transitions in InGaN/GaN single and DQWs
- the optimization of linear and nonlinear optical absorption coefficients in InGaN/GaN single and DQWs
- the investigation of the influence of the different structure designs on optical properties of InGaN/GaN single and DQWs
- the study of the influence of the different external and internal parameters (temperature, composition, electric field intensity...) on optical properties of InGaN/GaN single and DQWs
- the optimization of the effect the number of QWs on the linear, third-order nonlinear and total optical absorption coefficients
- the discussion of the possible use of this solution in different device applications

In this work, we have adopted a numerical method (i.e., Finite Element Method) to solve the Schrödinger equation as part of the effective mass approximation within these systems (MQWs). The well region was always made of InGaN while the barrier regions were made of GaN.
This manuscript is divided in five chapters:

Introduction presents a brief history of III-nitride materials and their developments in the market for LEDs and solar cells. The interest of InGaN alloys in photovoltaics and optoelectronics is explained, clarifying the main advantages and disadvantages on the way to efficient InGaN-based solar cells. The motivation and main goals of this work are also described.

Chapter 1 introduces general properties of III-nitrides materials in terms of crystal and electronic structure as well as a discussion of the origin of piezoelectric fields in III-N elements are presented. The chapter ends with the best techniques used nowadays to grow InGaN-based devices.

Chapter 2 is devoted to present the effects of the structure dimension, the In-compositions as well as the presence of a donor impurity on the optical transitions (ISB and BTB) related to the total optical absorption coefficient in InGaN/GaN single QW. We showed that the investigated parameters have a significant influence on the optical transitions in nanostructures based on III-nitride elements(In, Ga)N.

Chapter 3 shows the influence of temperature, size, coupling on ISB related to total optical absorption in InGaN/GaN double-quantum wells coupled with a finite square potential barrier. we investigated eight possible conduction optical transitions (ISB)($|1s\rangle \rightarrow 2p\rangle$, $|1s\rangle \rightarrow 3p\rangle$, $|2S\rangle \rightarrow 3p\rangle$, $|2s\rangle \rightarrow 2p\rangle$, $|2p\rangle \rightarrow 3s\rangle$, $|3s\rangle \rightarrow 3p\rangle$, and $|3p\rangle \rightarrow 3d\rangle$). It has been found that the variation of the above mentioned parameters has a significant impact on the change of the resonance peaks positions as well as their corresponding amplitudes in the studied system (DCQWs).

Chapter 4 is devoted the show the influence of temperature, In-composition, impurity and size of the ISB total optical absorption coefficient. First, we presented the theoretical framework then the impact of those physical parameters on the electron transition energy and dipole matrix element. Secondly, we shown the effect of the same parameters mentioned above on the total optical absorption coefficient and we closed the chapter with a brief conclusion.

chapter 5 is devoted to examine the influence of temperature, size, and the electric and magnetic fields intensity on the absorption spectrum in different shape double-quantum wells (DQWs). First, we overcome the theoretical background and models and then we presented the wave functions in different shaped DQWs. Secondly, we

shown the influence of those parameters on the transition energy, the dipole matrix-element and the positions of the resonance peaks and their associated amplitudes as well.

Finally, we ended this manuscript with a general conclusion in which we summarized the main obtained results in the frame of this thesis for InGaN/GaN QWs. Based on the obtained results, several perspectives for further structure optimization and parameters that were not done in this work are suggested to be considered and discussed in the future.

Chapter 1

Wide-band-gap semiconductors and the theory of optical transitions in QWs

Sommaire

1.1 Introduction . . . 11
1.2 Structural proprieties . . . 11
1.2.1 Crystalline structure . . . 11
1.2.2 Band structures of GaN and InN . . . 13
1.2.3 Band-gap parameters . . . 13
1.3 Piezo-electric and spontaneous polarization in III-N semiconductors . 15
1.3.1 Spontaneous polarization . . . 15
1.3.2 Piezo-electric polarization . . . 17
1.3.3 Total polarization . . . 18
1.4 From bulk material to low-dimensional systems . . . 18
1.5 Elaboration methods for III-nitrides growth . . . 20
1.5.1 Metallo-organic vapor phase epitaxy (MOCVD) . . . 21
1.5.2 Molecular beam epitaxy (MBE) . . . 21
1.6 Theory of quantum confinement in QWs . . . 22
1.6.1 Quantum confinement . . . 23
1.6.2 Quantum wells (QWs) . . . 23
1.6.3 Theoretical model of a single QW . . . 25
1.6.4 Optical transitions in QW . . . 28
1.6.5 Envelope function approximation . . . 28
1.7 Optical absorption coefficient . . . 29
1.8 Conclusion . . . 31

1.1 Introduction

This chapter is devoted to the presentation of the wide band gap semiconductors (III-nitride group) and the theory of optical transitions in quantum wells. First, we began with the structural properties including, crystalline structure, band structure, and the polarization as well (i.e, spontaneous and piezoelectric polarization). We also presented a brief summary of nanomaterial concepts and their properties, as well as some of the most common growth methods and technologies used today to grow materials layer by layer. Secondly, we ended this chapter by exploring the theory of quantum confinement in nanostructures and the optical absorption framework in low-dimensional systems.

1.2 Structural proprieties

1.2.1 Crystalline structure

Semiconductor materials based on III-N elements are chemical compounds constituted by the nitride (N) which is found in column V with an element of column III which is often gallium (also noted: Ga) and/or the indium (also noted: In) (see Mendeleev's table [Figure 1.1]).

Generally, Wide band-gap semiconductors are binary, ternary and quaternary com-

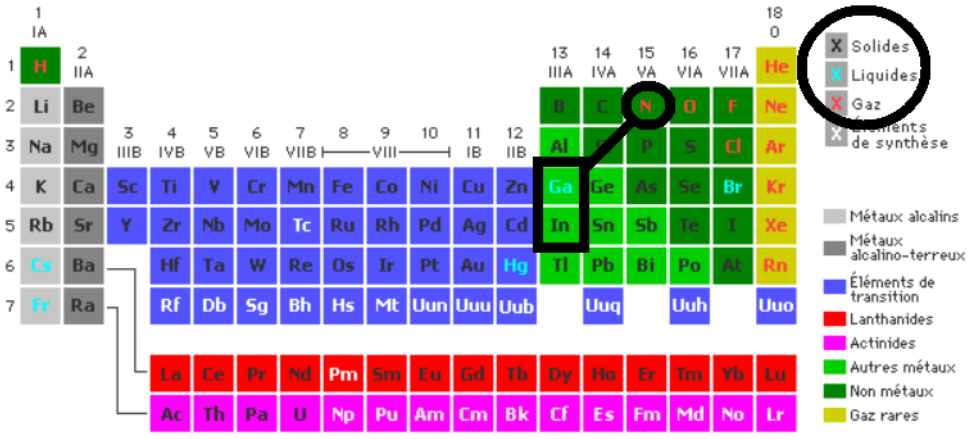


FIGURE 1.1: Mondeliev's periodic table: showing different III-N compound(original version has been modified) [83].

pounds formed from element (Ga, Al, In) and nitrogen (N). These III-N compounds can have two crystalline phases: the Zinc-Blende phase (Cubic) which consists of two face-centered cubic networks [Figure 1.2], one occupied by the elements III and the

TABLE 1.1: Lattice parameters of bulk wurtzite GaN and InN at room temperature. [55, 60].

Lattice parameter(nm)	GaN	InN	AlN
a(Å)	3.18	3.54	3.11
c(Å)	5.18	3.53	4.982
u	0.377	0.380	0.382

other occupied by the atoms of nitrogen, shifted by 1/4 of the diagonal as shown in [Figure 1.3]. In this thesis, we will focus only on the wurtzite structure properties because it is the most thermodynamically stable configuration that is usually grown by MOCVD[60]. The dependence of the length of the anion-cation bond on the nature of

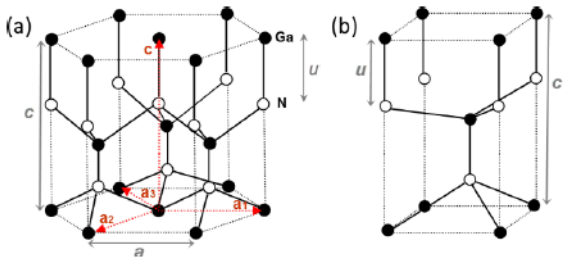


FIGURE 1.2: (a) Wurtzite and (b) zinc-blende crystallographic structures of GaN [55].

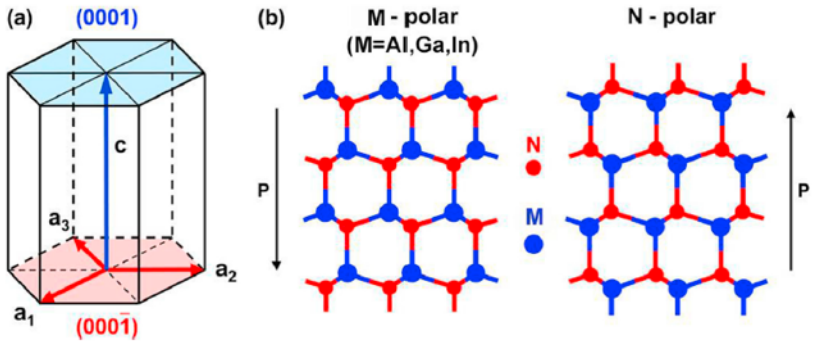


FIGURE 1.3: (a) Wurtzite unit cell (Hexagonal) and (b) atomic structure of binary nitrides M (M = Al, Ga, In) - and N-polar [18].

the cation and on the ionic radius actually causes a deviation from this ideal structure [74]. The lattice parameters GaN and that of InN at room temperature are listed in table 1.1. Regarding $In_xGa_{1-x}N$ alloys, the lattice parameter changes linearly with the composition of indium, as described by Vegard's law [79].

$$a^*_{In_xGa_{1-x}N} = xa^*_{InN} + (1-x)xa^*_{GaN} \tag{1.1}$$

where x is the composition of the indium in the ternary compound InGaN.

1.2.2 Band structures of GaN and InN

The binary materials formed by III-nitride elements such as GaN, AlN and InN are generally characterized by a direct gap (minimum of the conduction band and maximum of the valence band aligned at the center from the axis of Brillouin region). Several methods, which are the basis of many calculations, have been carried out to determine the band structure of these binaries, and particularly for GaN and InN. Figure 1.4, represents the band structures of wurtzite GaN and InN (w-GaN and w-InN) obtained by the empirical method of pseudo-potentials (energy band-gap), which is in good agreement with the experimental measurements of the gap[18]. The lateral valleys for InN and

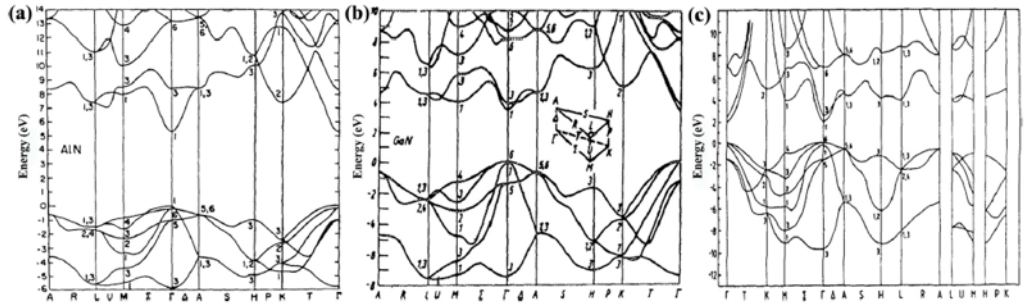


FIGURE 1.4: Calculated band structure of wurtzite binary nitrides: (a) AlN; (b) GaN; (c) InN [18].

GaN are energetically far from the band minima. So that, they are an appropriate materials for inter-subband based optoelectronic devices, to prevent inter-valley electron scattering [84].

1.2.3 Band-gap parameters

The estimated values of the band-gap energy of both GaN and InN were established in the early 1970s. The standard values used today are reported in table1.2. Due to crystal lattice expansion and electron-lattice interaction, the band-gap energy shows a temperature dependence which was first obtained experimentally by measuring the absorption [76] and the luminescence [58]. It is given by the formula (1.2) (Y. P. Varshni law):

$$E_g(T) = E_g(T=0) - \frac{\alpha T^2}{\theta_D + T} \tag{1.2}$$

TABLE 1.2: Band-gaps and effective masses of GaN and InN at T=0K [55, 4, 52].

Parameters	GaN	InN	AlN
E_g(eV)	3.18	0.72	6.28
$m_e^*(m_0)$	0.20	0.11	0.32
$m_h^*(m_0)$	1.25	1.63	0.37
α (meV/K)	0.90	0.78	-
θ_D (K)	830	370	-

where α and θ_D are respectively, the Varshni and Debye coefficients.

In ternary compounds ($In_xGa_{1-x}N$), the dependence of the band gap energy on the composition of an alloy is obtained using a quadratic polynomial whose nonlinear coefficient is called the bowing parameter b. This parameter reflects the deviation from a linear interpolation. The variation of band gap energy as a function of composition is given by the following quadratic polynomial eq . (1.3):

$$E_g(x) = xE_g^{InN} + (1-x)E_g^{GaN} - bx(1-x) \tag{1.3}$$

where the real value of the bowing parameter can varies between 1eV and 3.8 eV for InGaN[29]

In low-dimensional systems, it is very important to notice that as the dimension (size) of nanostructure (QW and/or QD) decreases the Coulomb attraction term could be neglected in the calculation because of the strong quantum confinement. Therefore, the band-gap energy decreases as the quantum well's size increases (see, Fig.1.5)[43].

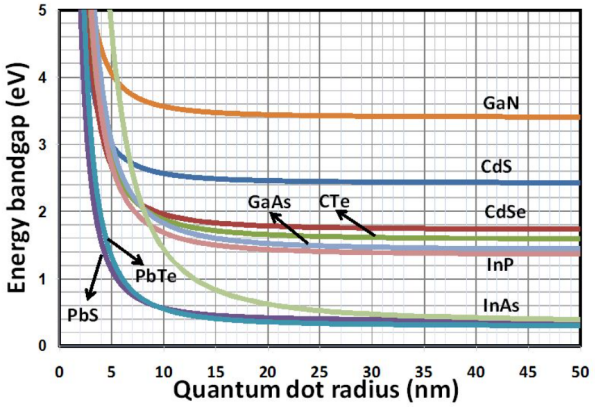


FIGURE 1.5: QD band gap energy for some common semiconductors versus the QD's size [43].

1.3 Piezo-electric and spontaneous polarization in III-N semiconductors

Due to the asymmetry of the w-GaN-based semiconductor heterostructures, an intense polarization field along the growth direction $< 0001 >$ exist in the GaN-based semiconductor. However, the barycenters of the positive and negative charges in a unit cell do not necessarily coincide, which results in the creation of an electric field along the growth direction $< 0001 >$. GaN-based semiconductor hetero-structures can being either polar, semi-polar and non-polar structures depending on the crystallographic orientations(see [Figure 1.6]). Spontaneous and piezoelectric polarization have analog values to each other for wurtzite type semiconductors[11].

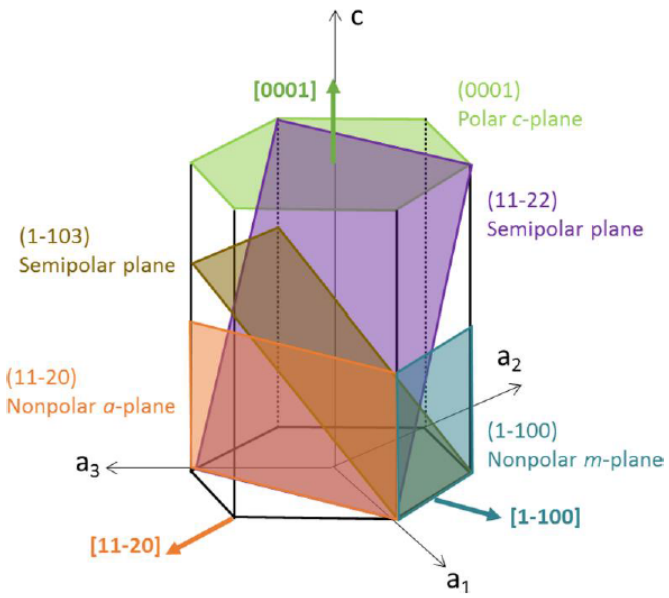


FIGURE 1.6: Illustration of the polar (0001), non-polar (1-100) and (11-20), and semi-polar (1-103) and (11-22) planes (modified from [14]).

1.3.1 Spontaneous polarization

In the absence of any constraint, the macroscopic polarization of a wurtzite type semiconductor is not zero. Its origin is the non-superposition of the barycenter of the loads carried by cations and anions. These centers are located in different reticular planes, which generates the creation of electric dipoles in the crystal in the direction perpendicular to the plane (0001) (crystallographic direction $\vec{c}$ of the hexagonal lattice). Wurtzite

is the crystal structure of highest symmetry allowing the existence of this spontaneous phenomenon[11]. The atomic planes along the [0001] direction consist of a successive stack of cation and anion planes, denoted ABAB stack, as illustrated in figure 1.8. The value of spontaneous polarization is mainly due to the chemical nature of the bonds in the crystal, which depends on the specific stacking of the different atoms. Measurement of this resulting polarization is impossible for massive crystals because of the polar nature of the surface which compensates the existing electric field due to the surface effects. This effect is related to the atomic states of cations and anions [80, 35]. To identify the crystallographic planes in the hexagonal lattice, we use the traditional notation system (hkl) proposed by Williams H. Miller. These indices are defined as specific intersections of the crystallographic plane with the fundamental axes of the crystal. By definition, the plane (hkl) closest to the origin intersects the axes $\vec{a_1}$, $\vec{a_2}$ and $\vec{c}$ of the lattice in a/h, a/h and c/l, as shown in figure 1.7.

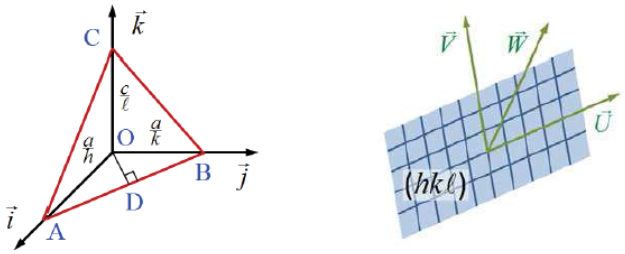


FIGURE 1.7: The orientation of the plane (hkl) in the frame of the crystallographic axes of the hexagonal lattice (left) and in the Cartesian frame defined by the vectors ($\vec{U}$,$\vec{V}$,$\vec{W}$) [71].

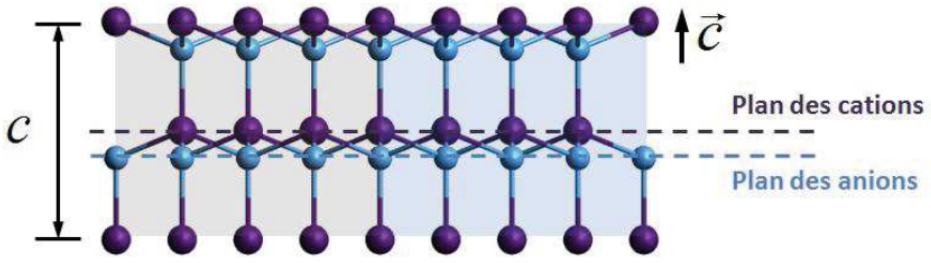


FIGURE 1.8: The schematic representation of the atomic planes ABAB on the direction $\vec{c}$ [11].

Besides ($\vec{U}$,$\vec{V}$) unit vectors, a third unit vector $\vec{W}$ normal to the plane (*hkl*) can be determined. The coordinates of these three unit vectors on the hexagonal basis ($\vec{i}$,$\vec{j}$,$\vec{k}$) are

given by the following expression (1.4).

$$\begin{bmatrix} \vec{U} \\ \vec{V} \\ \vec{W} \end{bmatrix} = \begin{bmatrix} -AK & Ah & 0 \\ -AalB_{ac}(2h+K) & -AalB_{ac}(2h+K) & 2c\frac{B_{ac}}{A} \\ \frac{2}{\sqrt{3}}cB_{ac}(2h+K) & \frac{2}{\sqrt{3}}cB_{ac}(2h+K) & \sqrt{3}laB_{ac} \end{bmatrix} \begin{bmatrix} \vec{i} \\ \vec{j} \\ \vec{k} \end{bmatrix} \tag{1.4}$$

The coefficients of equation (1.4), as well as the expressions for A and B_{ac}, depend on the values of the three Miller indices (hkl) and the ratio of the lattice parameters c/a [34, 13]. where $A = \frac{1}{\sqrt{h^2+hk+k^2}}$ and $B_{ac} = \frac{1}{\sqrt{3l^2a^2+4c^2(h^2+hk+k^2)}}$.
In the case of reticular lattice planes of arbitrary orientation (*hkl*), the components of the spontaneous polarization vector, P^{sp}, in the frame defined by ($\vec{U}$,$\vec{V}$,$\vec{W}$) are obtained from expression (1.5) which connects this to the international system ($\vec{x}$,$\vec{y}$,$\vec{z}$) :

$$\begin{bmatrix} P^{sp}_{\vec{U}} \\ P^{sp}_{\vec{V}} \\ P^{sp}_{\vec{V}} \end{bmatrix} = \begin{bmatrix} -\frac{\sqrt{3}}{2}AK & \frac{1}{2}A(2h+K) & 0 \\ -\frac{\sqrt{3}}{2}AalB_{ac}(2h+K) & -\frac{3}{2}AalkB_{ac} & 2c\frac{B_{ac}}{A} \\ AcB_{ac}(2h+K) & \sqrt{3}AckB_{ac} & \sqrt{3}lakB_{ac} \end{bmatrix} \begin{bmatrix} 0 \\ 0 \\ P^{sp} \end{bmatrix} \tag{1.5}$$

1.3.2 Piezo-electric polarization

The application of a mechanical constraint leads to the change of the parameters of the crystalline structure (c/a and u) under the effect of the deformation field. The deformation polarizes the structure electrically. In the case of wurtzite structures, a piezoelectric polarization induced by the deformation field is then superimposed on the spontaneous polarization. The components of this piezoelectric polarization are calculated from the deformation (ϵ_{ij}) and the piezoelectric coefficients (e_{ij}) of the crystal, they are expressed in the orthogonal coordinate system ($\vec{x}$,$\vec{y}$,$\vec{z}$) by the Eq. (1.6) [38, 70].

$$\begin{bmatrix} P_x \\ P_y \\ P_z \end{bmatrix} = \begin{bmatrix} 0 & 0 & 0 & 0 & 2e_{15} & 0 \\ 0 & 0 & 0 & 2e_{15} & 0 & 0 \\ 2e_{13} & 2e_{13} & 2e_{33} & 0 & 0 & 0 \end{bmatrix} \begin{bmatrix} \epsilon_{xx} \\ \epsilon_{yy} \\ \epsilon_{zz} \\ \epsilon_{yz} \\ \epsilon_{xz} \\ \epsilon_{xy} \end{bmatrix} \tag{1.6}$$

The values of the coefficients (e_{ij}) are listed in table 1.3 for the some main III-nitride elements.

TABLE 1.3: The piezoelectric coefficients for certain III-nitride(wurtzite) semiconductors [34].

Material	$e_{13}(cm^{-2})$	$e_{33}(cm^{-2})$	$e_{15}(cm^{-2})$
AlN	-0.533	–0.623	–0.351
GaN	–0.338	–0.372	–0.167
InN	–0.413	–0.454	–0.112

In the same way as for spontaneous polarization, it is possible to write the components of the piezoelectric polarization vector in the coordinate system of the reticular plane (hkl) characterized by the coordinate system ($\vec{U}$,$\vec{V}$,$\vec{W}$) from the following expression (see Eq. (1.7)):

$$\begin{bmatrix} P^{pz}_{\vec{U}} \\ P^{pz}_{\vec{V}} \\ P^{pz}_{\vec{V}} \end{bmatrix} = \begin{bmatrix} -\frac{\sqrt{3}}{2}AK & \frac{1}{2}A(2h+K) & 0 \\ -\frac{\sqrt{3}}{2}AalB_{ac}(2h+K) & -\frac{3}{2}AalkB_{ac} & 2c\frac{B_{ac}}{A} \\ AcB_{ac}(2h+K) & \sqrt{3}AckB_{ac} & \sqrt{3}lakB_{ac} \end{bmatrix} \begin{bmatrix} P_x \\ P_y \\ P_z \end{bmatrix} \tag{1.7}$$

1.3.3 Total polarization

The total polarization (to the first order) according to the direction of growth, direction orthogonal to the plane ($hk.l$), of a strained layer is the sum of the projection on this direction of the spontaneous polarization ($P^{sp}_{[hk.l]}$) and piezoelectric polarization (see Eq. (1.8)) [71]:

$$P^{tot}_{[hkl]} = B_{ac}\{2Ace_{15}\left((2h+k)\epsilon_{xz}+\sqrt{3}k\epsilon_{yz}\right)+a.l\left(e_{13}(\epsilon_{xx}+\epsilon_{yy})+e_{33}\epsilon_{zz}\right)\}+P^{sp}_{[hkl]} \tag{1.8}$$

1.4 From bulk material to low-dimensional systems

In a bulk semiconductor crystal, the charge carriers are free to move in the three directions of space while in low-dimensional systems such as quantum well (QW), quantum well wire (QWW), and quantum dot (QD) the electron is allowed to move in 2D, 1D and 0D spaces, respectively.

The mesh of the reciprocal lattice, allows us to see that the electrons (and the holes) will populate bands of energy following different forms dispersion (E(k)) as it can be shown

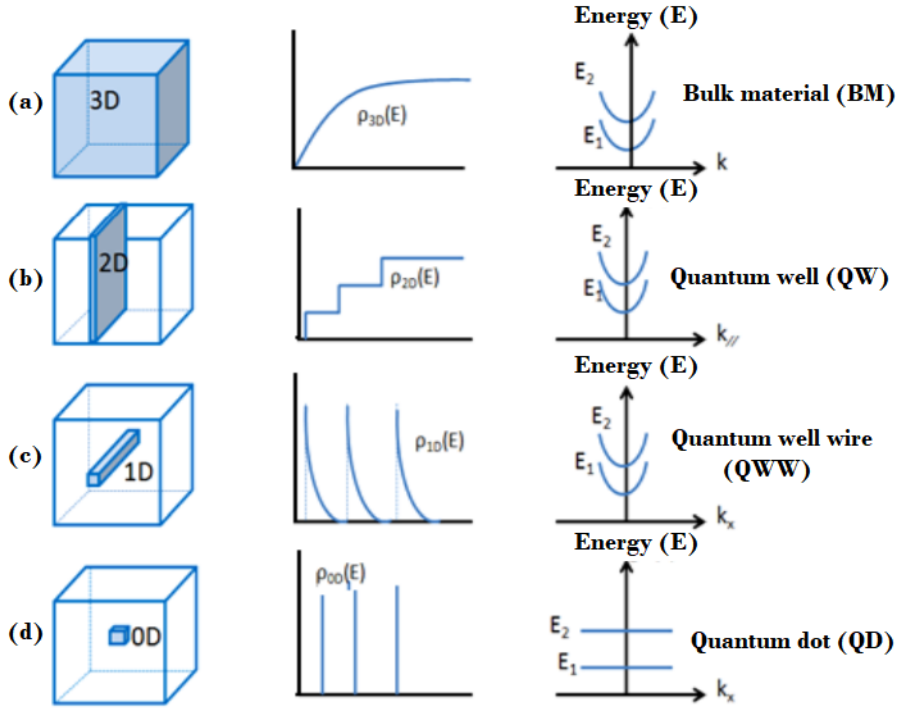


FIGURE 1.9: Schematic description of the confinement effect of carriers, on the density of state and the electronic structure of bands in: (a) a 3D bulk material, (b) a 1D quantum well, (c) a 1D quantum wire, (d) a quantum dot (modified from) [90].

in the Fig.1.9 . The density of state (DOS) versus the energy can be given as (Eq.1.9):

$$\rho(E)^{DOS} = \begin{cases} \rho_{3D}(E) \propto \sqrt{E}, & \text{Bulk material (BM);} \\ \rho_{2D}(E) \propto \text{Constant}, & \text{Quantum well (QW);} \\ \rho_{1D}(E) \propto \frac{1}{\sqrt{E}}, & \text{Quantum well wire (QWW);} \\ \rho_{0D}(E) \propto \delta(E), & \text{Quantum dot (QD).} \end{cases} \tag{1.9}$$

As shown in the Fig.1.10, unlike bulk semiconductors such as crystalline silicon, quantum wells can generate multiple excitons (electron-hole pairs) after absorbing a photon with energy greater than or equal to the band gap energy. In the case of a bulk semiconductor, the absorption of a photon whose energy exceeds the band gap excites an electron from the valence band to a higher level in the conduction band. Such generated electrons are called hot carriers. The excited electron (hot carrier) undergoes many non-radiative relaxations (thermalisation: multi-phonon emission) before reaching the bottom of the conduction band. However, in a quantum well, the hot carrier is subject to a process of impact ionization (multiplication of the carriers). Therefore, the absorption

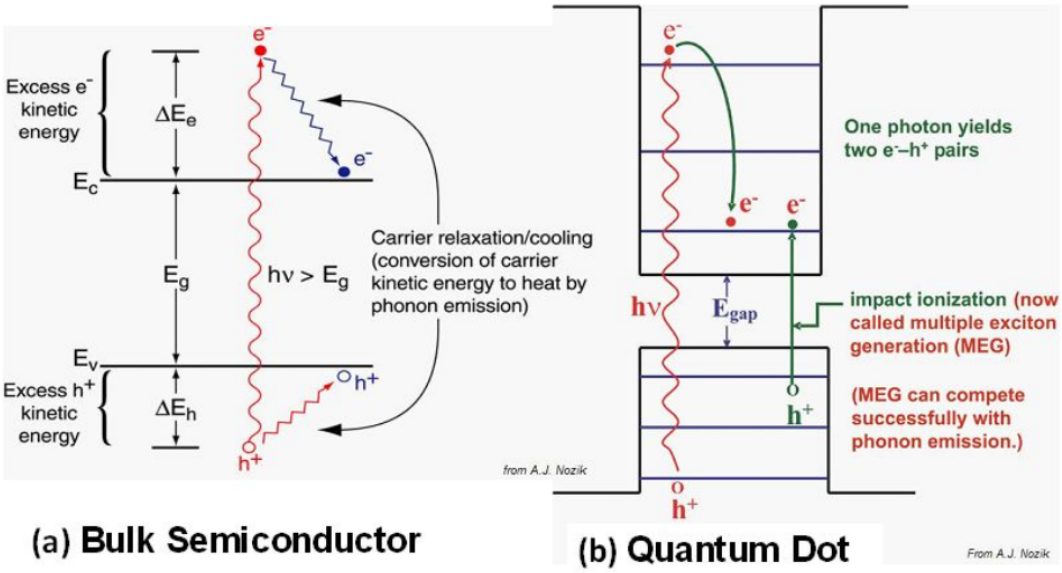


FIGURE 1.10: Schematic description of band diagram and the absorption/relaxation mechanisms in: (a) Bulk material, (b) Quantum well [43].

of a single photon generates multiple electron-hole pairs. Therefore, the absorption of UV photons in quantum wells produces more electrons than near-infrared photons[43].

1.5 Elaboration methods for III-nitrides growth

Unlike in the case of semiconductors such as silicon or GaAs, the difficulty of growth is largely related to the lack of suitable substrates for epitaxial growth. As well as the difficulty in obtaining this type of crystals comes from its very high melting point and the strong saturating vapor pressures of the compounds. Massive single crystals have been successfully produced at high pressure, but the available surface area is 100 mm^2 for 200 hours of growth. So growing single crystals is not easy [6]. Several approaches and different substrates are used to produce III nitrides, among these substrates we find silicon carbide (SiC), sapphire (Al2O3), silicon, which represent a mesh mismatch with III nitrides like GaN with a hexagonal structure, unlike the cubic structure of the substrates which we mentioned previously, consequently constraints are appearing and therefore defects in the material.To manufacture electronic and optoelectronic devices from nitrides, the development of good quality thin films is necessary. Nitride epitaxy is generally carried out by very specific processing techniques such as MBE, EPVH, PLD, and MOCVD, so on. In this section, we will explore juste MBE and MOCVD

methods.

1.5.1 Metallo-organic vapor phase epitaxy (MOCVD)

Organometallic vapor phase epitaxy (MOCVD) is the primary growth technique for III nitrides. Its flexible implementation, the possibility of epitaxy over large areas and its low cost compared to MBE make it widely used for manufacturing components in the semiconductor industry [10]. MOCVD is based on a property of organometal-

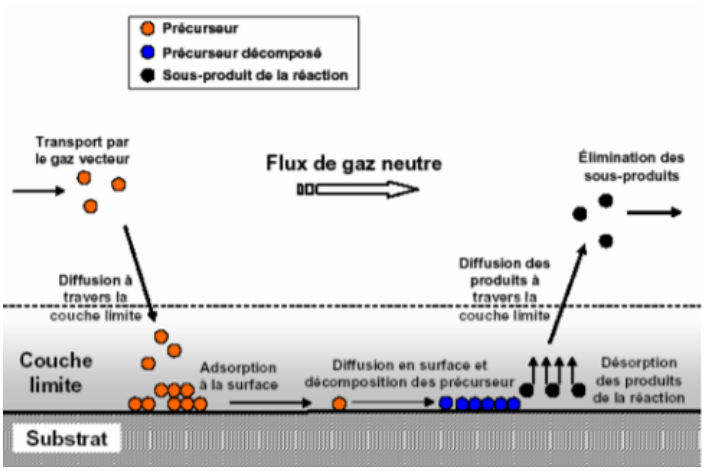


FIGURE 1.11: Schematic discreption of MOCVD method [77].

lic compounds which is the strong temperature dependence of their vapor pressure. This method consists of a pyrolysis one of organometallic compounds and hydrides (NH3, SiH4) transported by a gas (nitrogen or hydrogen) in the vicinity of the substrate brought to high temperature. The streams of the sources used are stabilized, then mixed just before their introduction into the reactor (see [Figure 1.11]). For gallium, triethylgallium or trimethylgallium are the main compounds used. The growth of GaN takes place at a temperature between $1000°C$ and $1150°C$. The growth rates depend on the deposition conditions but remain substantially close to a few microns per hour. Since the desired structures are always less than ten microns thick, a few hours are enough to achieve them [20].

1.5.2 Molecular beam epitaxy (MBE)

During growth by MBE, the constituent elements of the material to be epitaxied have just deposited on a substrate brought to high temperature. These elements resulting

from the evaporation or sublimation of solid sources are transported to the substrate in the form of molecular jets. This technique therefore requires the implementation of an ultra-vacuum in the frame. The particles arriving with a certain energy are adsorbed on the surface, on which they will be able to move (see [Figure 1.12]).

The time during which the atoms remain on the surface of the substrate depends on the temperature of the latter: too high a temperature will promote the desorption of the atoms. Atoms on the surface move to join either another small group of atoms and form a nucleus, or an existing edge. The nuclei continue to form (nucleation phase) to reach a critical density from which we see the formation of small islets. The islets will then coalesce to form an epitaxial monolayer. The process repeated in this way gives the final epitaxial film.

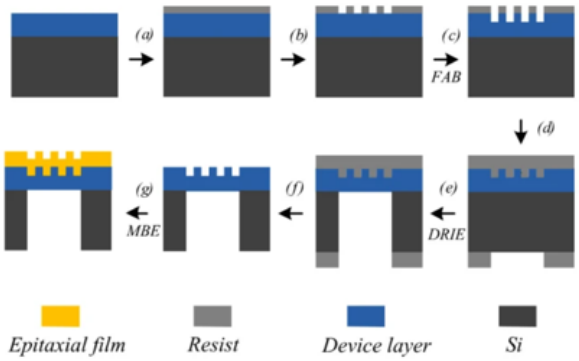


FIGURE 1.12: schematic patterned growth process on a self-supporting GaN lattice by molecular beam epitaxy (MBE) [82].

In the case of nitrides, gallium and indium atoms are obtained by sublimation from solid sources. Nitrogen is obtained from a gaseous precursor which can be either ammonia (NH_3) or the N_2 molecule. In the latter case, the chemically very stable N_2 molecule is dissociated either by radio frequency (RF nitrogen source) or by electron-cyclotron resonance (ECR). The substrate temperature for the deposition of nitrides by MBE is conventionally between $450°C$ and $850°C$ [82].

1.6 Theory of quantum confinement in QWs

Quantum confinement of the charge carriers in more than one dimension in quantum wire (QWR) and quantum dot (QD) heterostructures has been predicted to yield

improved static and dynamic performance of semiconductor lasers as compared with quasi-two-dimensional (2D) quantum well (QW) devices[45]. Because of quantum confinement, the electronic levels are discretized in structures of a few nanometers, compared to the Bohr radius. The simplest case to model is the electronic behavior in QWs.

1.6.1 Quantum confinement

We speak of quantum confinement when at least one dimension of a crystal is less than a characteristic size a_0, the Bohr radius. If you illuminate a semiconductor with radiation of energy greater than the band-gap energy, exciton is created. In other words electron-hole pair bounded by a Coulomb interaction is created. The size of this exciton is then called the Bohr radius. Moreover, it defines the average distance between the generated electron-hole pairs. The analytical expression of a_0 is given by the Bohr model (see Eq. (1.10)).

$$a_0 = \frac{4\pi\varepsilon_0\varepsilon_r^*\hbar^2}{m_0 m_{e,h}^* e^2} \tag{1.10}$$

Where ε_r^*, m_e^*, m_h^* are respectively, the relative dielectric constant of the considered material, and the electron, and the hole's effective masses.

Now, if a dimension of the crystal is reduced below the Bohr radius, the excitons are confined. The system is then equivalent to a quantum well (confinement in one dimension), or a quantum wire (confinement in two dimensions), or a quantum box (or quantum dot, confinement in three dimensions). The main consequence of this confinement is that the optical band-gap energy increases. This is the major interest of small dimension semiconductors [69].

1.6.2 Quantum wells (QWs)

A quantum well (QW) is a nanoscale layer that can confine (quasi)particles (usually electrons or holes) in the dimension perpendicular to the layer's surface, while their movement in the other dimensions is unrestricted. Confinement is a quantum effect. It has profound effects on the density of states for confined particles. For a quantum well with a rectangular profile, the density of states is constant in certain energy intervals. This system (QW) is often made with a thin layer of a semiconductor medium, embedded between other semiconductor layers of wider band-gap energy. The thickness of

such a quantum well is typically 1 to 20 nm. Depending on the confinement of carriers, there are different types of quantum structures, the two main configurations are represented in Fig 1.13.

In the case of a **Type-I** structure, the electrons and holes are confined in the well

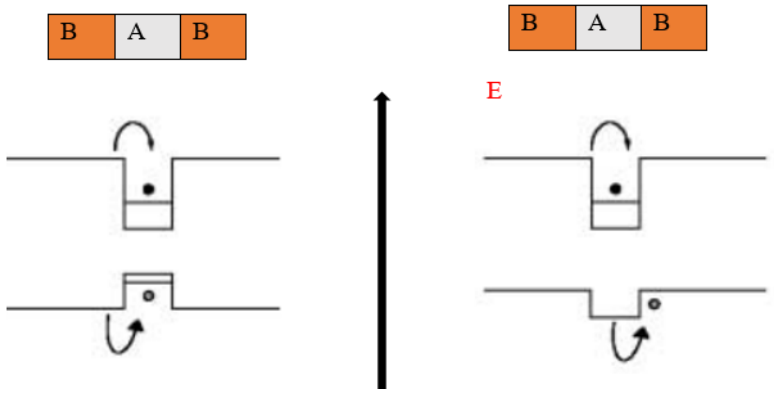


FIGURE 1.13: Representation of the different types of quantum wells [15].

represented by semiconductor **A**, while they are spatially separated in the **Type-II** configuration. In quantum well systems (bi-dimensional), the movement of the electron is free only in the plane of the well layer but it is restricted in the direction of growth and the energy levels are quantified along this direction. In this work, we are only interested on the **Type-I** where the electrons and the holes are confined in the same semiconductor **A**. If the width of this well is wide enough, the charge carriers will in practice have the same properties as in a crystal of infinite volume (see [figure 1.14]). On the other hand, if L_z is the order of magnitude of the De Broglie wavelength associated with the electron given by Eq. (1.11), the carriers undergo the effects of the potential barriers and the energy spectra of these are quantified.

$$\lambda_{DeBroglie} = \frac{h}{p} = \frac{h}{2mk} \tag{1.11}$$

If two quantum wells are combined with a barrier that is wide enough so that the wave functions in adjacent wells do not overlap, it is called a double quantum well (DQW). On the other hand, if the barrier is small enough to allow recovery, we say we have a super-lattice. Additionally, semiconductor quantum wells are commonly used in the active region of laser diodes, solar cells and LEDs...they are growth between two wider layers with higher bandgap energy. If the difference in bandgap energy is large enough,

these claddings act as waveguides, while electrons and holes are efficiently trapped (individually confined) by the quantum wells. Quantum wells are also used as semiconductor saturable absorber mirrors (SESAM: are saturable semiconductor absorbers, used as nonlinear mirrors, they are mainly used for passive mode locking of lasers, "Dr.R.Paschotta") and for electro-absorption modifiers as well . Multiple quantum wells (MQWs) can also be used if large optical gain or absorption is required, usually with a sufficiently large spacing to avoid overlapping of the corresponding wave functions.

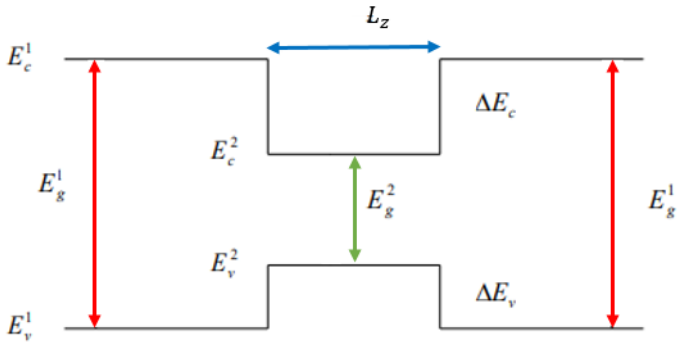


FIGURE 1.14: Schematic representation of the band diagram of a quantum well (modified from [15]).

1.6.3 Theoretical model of a single QW

In the effective mass approximation, the Schrödinger's equation associated with an electron in a nanocrystal is given as follows:

$$H|\Psi(r)>=E|\Psi(r)> \tag{1.12}$$

In the effective-mass approximation, the energy level of an electron quantum well subjected to a uniform magnetic field $B = (0, 0, B)$, is given by the solution of the Schrodinger equation with the Hamiltonian as [73]:

$$\hat{H} = \frac{\hat{p}^2}{2m^*} + V_c(z) - \frac{e^2}{\varepsilon_0 r} + \frac{\omega_c L_z}{2} + \frac{m^*\omega_c^2}{8}(x^2 + y^2) - eFz \tag{1.13}$$

where r, e and m^* denote the position, the charge and the effective-mass of the electron, respectively. $\omega_c = eB/m^*c$ is the cyclotron frequency of a free carrier in the magnetic field B, and L_z, is the z-component of the orbital angular momentum $(\mathbf{L})$. F is the electric field strength. $V_c(z)$ is the confinement potential. For a single quantum well of

thickness L, it is given by the following expression (1.14),

$$V_c(z) = \begin{cases} 0, & \text{for} |z| \leq \frac{L_z}{2}, \\ V_0, & \text{for} |z| > \frac{L_z}{2}. \end{cases} \tag{1.14}$$

The minimum of the conduction band is taken as the origin of the energies located at the center of Brillouin zone(k=0). Without perturbation, the Schrodinger equation given by Eq.1.15:

$$H_0 \phi_0(z) = E_z \phi_0(z) \tag{1.15}$$

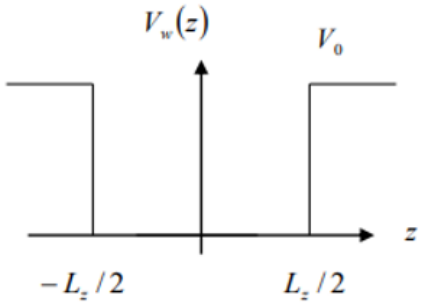


FIGURE 1.15: Representation of a **finite** rectangular potential.

The boundary conditions impose the continuity of $\phi(z)$ and its first derivative at $|z| = \frac{L_z}{2}$.

- **In the case of an infinite confinement potential ($V_c \to \infty$)**:

  Equation (1.15) becomes:

$$\begin{cases} -\frac{\hbar^2}{2m^*} \frac{\partial^2}{\partial z^2} \phi(z) = E_z \phi(z), & \text{for} |z| < \frac{L_z}{2}, \\ \phi(z) = 0, & \text{for} |z| > \frac{L_z}{2}. \end{cases} \tag{1.16}$$

The n^{th} state is characterized by:

$$\begin{cases} \phi_{2n+1} = \cos\left[(2n+1)\frac{\pi z}{2}\right] \to E_z^{2n+1} = \frac{\hbar^2 \pi^2 (2n+1)}{2m^* L_z^2}, & \text{for even states,} \\ \phi_{2n+2} = \cos\left[(2n+2)\frac{\pi z}{2}\right] \to E_z^{2n+2} = \frac{\hbar^2 \pi^2 (2n+2)}{2m^* L_z^2}, & \text{for odd states.} \end{cases} \tag{1.17}$$

We notice that the wave functions are either even or odd along z, which reflects the

symmetry of the potential. Then, the total energy will be expressed as follows:

$$E = E_{nz} + \frac{\hbar^2}{2m^*}(k_x^2 + k_y^2) \tag{1.18}$$

- **In the case of a finite confinement potential ($V_c = V_0$):**

We have a discrete spectrum of localized states, with energies between 0 and V_0, followed by a continuum above V_0. The Schrodinger's equation is given by the following expression:

$$\begin{cases} -\frac{\hbar^2}{2m^*}\frac{\partial^2}{\partial z^2}\phi(z) = E_z\phi(z), & \text{Inside the QW,} \\ -\frac{\hbar^2}{2m^*}\frac{\partial^2}{\partial z^2}\phi(z) = (E_z - V_0)\phi(z), & \text{outside the QW.} \end{cases} \tag{1.19}$$

The wave functions can be written in the following form:

$$\phi(z) = \begin{cases} A\cos(Kz), & \text{for} |z| \leq \frac{L_z}{2}, \\ Be^{-K^{'}|z|}, & \text{for} |z| > \frac{L_z}{2}. \end{cases} \tag{1.20}$$

where K and $K^{'}$ are respectively given by the following expressions:
$K = \sqrt{\frac{2m^*E_z}{\hbar^2}}$, $K^{'} = \sqrt{\frac{2m^*(V_0 - E_z)}{\hbar^2}}$.
Based on the boundary conditions, the eigen-values are obtained via the following implicit equation.

$$K^{'} = K\tan(K\frac{L_z}{2}) \tag{1.21}$$

Which determines a sequence k_n giving discrete particle (electron, hole) energy levels in the form:

$$E_{zn} = \frac{\hbar^2}{2m^*}k_n^2 \tag{1.22}$$

In the case of the finite potential high, there is an added purely tunnel quantum effect, i.e. the probability outside the well is not zero. However, for many semiconductors, the top of the valence band consists of two degenerate bands correspond to different effective masses [39].

1.6.4 Optical transitions in QW

The growth of nanoscale layer of semiconductor (A) with band gap energy (E_g^A) between two layers of another semiconductor (B) with a larger band gap energy (E_g^B) leads us to obtain a QW. For small well thickness, the quantum size effect becomes to be appear and then the particle's movement becomes restricted along the growth direction. This 1D-dimensional quantification of energy levels result in the formation of subbands in the conduction and valence bands.

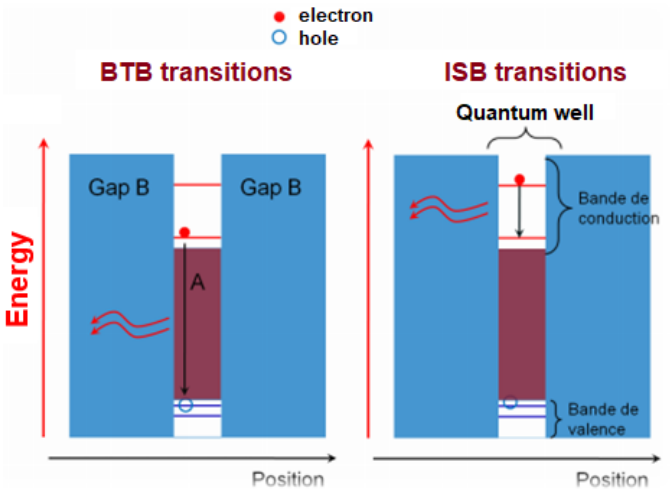


FIGURE 1.16: Profile of a quantum well formed by two different band gap energy materials **A** and **B**: On the left (interband transition); Right (intra-subband transition) [69].

1.6.5 Envelope function approximation

For an heterostructure made up of two materials A and B, the approximation of the envelope function consists of writing the electronic wave function $\psi(r)$ at Γ-point as the product of the Bloch function $U_v(r)$ rapidly variable at the elementary scale cell, by a slowly variable envelope function $f_n(r)$ [16, 7, 9]:

$$\psi(r) = f_n(r) \times U_v(r) \tag{1.23}$$

Based on the assumption that the rapidly varying functions $U_v(r)$ are not only independent of k, but also the same in both materials A and B.

$$U_v^A(r) \approx U_v^B(r) \tag{1.24}$$

In the quantum well, the potential of the heterostructure depends only on z and then the crystal invariant being conserved in the plane (xOy). The envelope function can therefore be written [7]:

$$f_{n,k}(r) = \frac{1}{\sqrt{S}}\Phi_n(z)e^{ik_{//}\rho} \tag{1.25}$$

where $k_{//} = (k_x, k_y)$ is the wave vector in the plane (xOy), S is the normalization surface and ρ corresponds to the projection of the vector $\vec{r}$ on the plane (xOy). Therefore, the total energy is then can be given as the following expression:

$$E_{n,k} = E_n + \frac{\hbar^2 k_{//}^2}{2m^*} \tag{1.26}$$

To obtain the final wave function, we must solve this equation in each material and use the continuity relations at the interface ($z = z_{AB}$) of the wave functions and the probability currents according to [8].

$$\Phi_n^A(z_{AB}) = \Phi_n^B(z_{AB}) \tag{1.27a}$$

$$\frac{1}{m_e^A}\frac{\partial}{\partial z}\Phi_n^A(z_{AB}) = \frac{1}{m_e^B}\frac{\partial}{\partial z}\Phi_n^B(z_{AB}) \tag{1.27b}$$

1.7 Optical absorption coefficient

The study of electronic states in quantum wells requires quantum mechanical concepts. The description of electromagnetic fields (frequency ω and wave vector $\vec{q}$) is done classically many years ago by Maxwell's equations. Therefore, the most commonly used interacting Hamiltonian in solids in the Coulomb gauge is given by Eq. (1.28).

$$H_{int} = \frac{e}{m^*}(\vec{A}.\vec{P}) \tag{1.28}$$

where $\vec{A}$ is the magnetic potential vector $\left(\vec{A} = -\frac{\partial \vec{E}}{\partial t}\right)$, and the electric field is written as fellows:

$$\vec{E}(r,t) = E_0\vec{e}\cos(\vec{q}.\vec{r} - wt) \tag{1.29}$$

Considering the expression of the electric field, the magnetic potential vector becomes:

$$\vec{A}(r,t) = \frac{E_0\vec{e}}{\omega}\sin(\vec{q}\vec{r} - \omega t) \tag{1.30}$$

where $\vec{q}$ is the propagation vector and $\vec{e}$ is the polarization vector. So the transition probability can be written as follows (Eq. (1.31)):

$$W_{if} = \frac{2\pi}{\hbar}\frac{e^2E_0^2}{4m^{*2}\omega^2}|\langle\psi_f|\mathbf{e.p}|\psi_i\rangle|^2\delta(E_f - E_i - \hbar\omega) \tag{1.31}$$

Using the expression of the envelope functions given before (first section: Eq. (1.25)), the matrix element $\langle\psi_f|\mathbf{e.p}|\psi_i\rangle$ can be divided into two parts. Due to the slow variation of the envelope function f_n compared to that of the Bloch function u_v, the matrix element expressed as follows:

$$\langle\psi_f|\mathbf{e.p}|\psi_i\rangle = \mathbf{e}.\langle u_v|\mathbf{p}|u_v^{'}\rangle\langle f_n|f_n^{'}\rangle + \mathbf{e}.\langle u_v|u_v^{'}\rangle\langle f_n|\mathbf{p}|f_n^{'}\rangle \tag{1.32}$$

The first term of this equation is non-zero only for states from different bands ($v \neq v^{'}$) which gives rise to inter band transitions. The functions u and v being orthogonal ($\langle u_v|u_{v'}\rangle$=1), the second term couples only the states resulting from the same band. It describes inter subband transitions. Thus, the matrix element is given by the following expression:

$$\langle f_{n,k}|e.p|f_{n',k'}\rangle = \frac{1}{S}(\int \mathrm{d}^3re^{-ikr}\Phi_n^*(z))[e_xp_x + e_yp_y + e_zp_z]e^{ik'r}\Phi_n'(z) \tag{1.33}$$

Due to the particular form of the envelope functions, the integrals along x and y are zero, only the term proportional to e_z is non-zero. This selection rule means that only the component of the electric field perpendicular to the plane of the layers couples to the inter-subband transitions. So the whole problem boils down to calculating the dipole:

$$\langle n|p_z|n'\rangle = (\int dz\Phi_n^*(z)p_z\Phi_n'(z)) \tag{1.34}$$

The absorption coefficient (α) is therefore defined as the ratio between the energy absorbed per unit volume and per unit of time, and the incident energy. For a transition between the i^{th} and f^{th} subbands states, it is given by[32],

$$\alpha(\omega) = \frac{S}{\Omega}\frac{\pi(E_i - E_f)^2(\varepsilon M_{if})}{\hbar^2\omega nc}(n_i^s - n_f^s)\delta(E_f - E_i - \hbar\omega) \tag{1.35}$$

In real quantum wells, the Dirac function $\delta(E)$ must be replaced by a spectral broadening function $g(E)$ which reflects the finite width of the absorption line. This function is introduced in a phenomenological way. In the particular cases of purely homogeneous or pure inhomogeneous enlargement, $g(E)$ corresponds to a function of Lorentzian or Gaussian type, respectively. It is given respectively by:

$$g(E) = \frac{\hbar\Gamma}{\pi}\frac{1}{(E_f - E_i - \hbar\omega)^2 + (\hbar\Gamma)^2} \tag{1.36a}$$

$$g(E) = \frac{1}{\sqrt{\pi}\hbar\Gamma}e^{-\frac{(E_f - E_i - \hbar\omega)^2}{(\hbar\Gamma)^2}} \tag{1.36b}$$

On the other hand, the inter-subband absorption coefficient of the transition $E_{fi} = E_f - E_i$ is the product of the effective absorption section $\sigma(\omega)$ by the population difference between the initial and finale subbands per unit of volume. It is written as:

$$\alpha(\omega) = \frac{(n_i^s - n_f^s)}{L}\sigma(\omega) \tag{1.37}$$

From equations given above, we deduce the expression for the effective absorption cross-section:

$$\alpha(\omega) = \frac{\pi(E_i - E_f)^2 M_{if}^2 \sin(\theta)^2}{\hbar^2 nc\omega c\cos(\theta)}g(E_f - E_i - \hbar\omega) \tag{1.38}$$

Another often used quantity called oscillator strength which describes the initial and final overlapping is given as:

$$f_{if} = \frac{2m_0(E_i - E_f)}{e^2\hbar}\mu_{fi}^2 \tag{1.39}$$

So the absorption cross-section is written as fellows:

$$\sigma(w) = \frac{e^2\pi(E_i - E_f)^2}{2m_0 nc\omega\varepsilon_0}f_{if}\frac{\sin^2(\theta)}{\cos(\theta)}g(E_f - E_i - \hbar\omega) \tag{1.40}$$

1.8 Conclusion

In this chapter, we presented the the main characteristics of wide-band-gap semiconductors (III-nitride group) and the theory of optical transitions in quantum wells. First,

we gave an overview of the structural properties of those particular materials including, crystalline structure, band structure, and the polarization as well. We also presented a brief summary of the difference between nano and bulk materials. We presented some of the most common growth methods and technologies used today to grow materials layer by layer as well. Finally, we ended this chapter by exploring the theory of quantum confinement in nanostructures and the optical absorption in low-dimensional systems (e.g, QD and QWs).

Chapter 2

BTB and ISB optical absorption in single QW: Size, In-composition and impurity effects

Sommaire

2.1 Introduction . . . 35
2.2 Theoretical framework . . . 35
2.3 Optical properties in single QW . . . 37
2.3.1 ISB and BTB electron transition energy in single QW . . . 38
2.3.2 Dipole matrix-element in single QW . . . 39
2.3.3 Optical absorption in single QW . . . 40
2.4 Optical absorption and refractive index in IPQW and ITQW . . . 45
2.4.1 Shape and In-composition effects . . . 46
2.4.2 Optical absorption and refractive index change . . . 48
2.5 Conclusion . . . 50

2.1 Introduction

Intra-subband (ISB) and band-to-band (BTB) optical transitions in nanostructures have been intensively studies in several works. Recently, theoretical investigation of the optical absorption coefficients (e.g., linear, third-nonlinear and total) related to ISB and BTB transitions have been the subject of many reported work in literature[1, 24, 66, 42]. Through this chapter, we investigate of the optical absorption related to ISB and BTB optical transitions. We show the influence of the size, indium concentration and impurity position within the QW. First, we started with investigation of the impact of size, In-composition and impurity's position on the electron transition energy (ΔE_{fi}), the square of dipole matrix-element ($|M_{fi}|^2$) and total optical absorption coefficient ($\alpha^{(Tot)}$) related to ISB. Secondly, we examined the effect of the same parameters mentioned above on the electron transition energy (ΔE_{fi}) and on the total optical absorption coefficient related to BTB.

2.2 Theoretical framework

The studied configuration represents one of the simplest systems used to study the optical and electrical proprieties of quantum wells2.1. In this structure, we consider GaN as the barrier material of thickness L while InGaN alloy is the QW material with thickness l. Within the effective mass approximation, the electron Hamiltonian of the studied system is the same as that in the previous chapter. The necessary physical parameters and constants used to perform this study (E_g^i, m_i^*, and ε_i^*) are given in table2.1. To ensure the continuity of the electron wave function at the interfaces between InGaN/GaN, the effective mass and dielectric constant mismatches are taken into account. For the interfaces, the effective-mass and relative dielectric constant are adopted respectively as: $\sqrt{m_b^* m_w^*}$ and $\sqrt{\varepsilon_b^* \varepsilon_w^*}$ where b and w refer to barrier and well, respectively.

TABLE 2.1: Band-gaps, effective masses and dielectric constants of GaN and InN at T=0K [55, 4].

Parameters	GaN	InN
E_g(eV)	3.18	0.72
$m_e^*(m_0)$	0.20	0.11
$m_h^*(m_0)$	1.25	1.63
$\varepsilon_r^*(\varepsilon_0)$	8.9	11

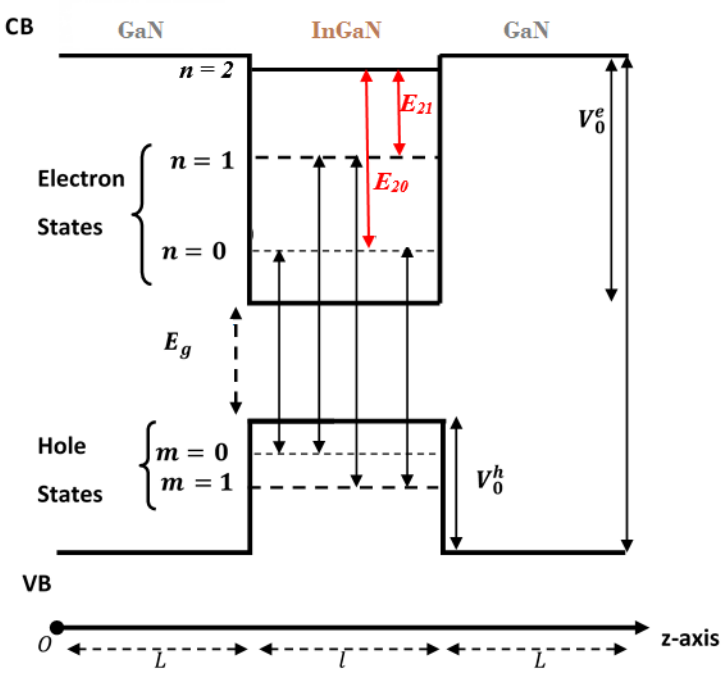


FIGURE 2.1: Schematic representation of different optical transitions in SQW with a finite potential barrier: ISB (Red narrows) and BTB (Black narrows). The excitation comes from $z = 0$.

Along this chapter, we consider an unstrained w-GaN/(In,Ga)N structure. The indium-dependent growth direction confinement potential barrier, $V_c(z)$, is given as:

$$V_c(z) = \begin{cases} 0, & \text{Inside the QW} \\ Q\Delta E_g(x), & \text{Outside the QW} \end{cases} \tag{2.1}$$

where $Q(= 0.7)$ is the conduction band-offset parameter, and $\Delta E_g(x) = E_g^{GaN} - E_g^{InGaN}$. The indium-dependent band-gap energy of ternary alloy (InGaN) is given by the Vegard's law below:

$$E_g^{In_xGa_{(1-x)}N}(x) = xE_g^{InN} + (1-x)E_g^{GaN} - b(1-x) \tag{2.2}$$

where x is the indium fraction and $b(= 1.43eV)$ represents the bowing parameter according to[3]. The same law (Vegard's low) is applied to obtain indium-dependent effective-mass and the dielectric constant (see Eq.(2.3a),(2.3b)):

$$m^*_{In_xGa_{(1-x)}N}(x) = xm^*_{InN} + (1-x)m^*_{GaN}, \tag{2.3a}$$

$$\varepsilon^*_{In_xGa_{(1-x)}N}(x) = x\varepsilon^*_{InN} + (1-x)\varepsilon^*_{GaN}, \tag{2.3b}$$

The energy-levels and their associated wave functions can be obtained by solving numerically the Schrödinger equation using finite element method (FEM). The continuity of the wave functions and the probability current according to Ref.[8] are given by the Eqs.(2.4a),(2.4b) and (2.5a),(2.5b) (for more detail, see Appendix A):

$$\Phi_n^{GaN}(z=l) = \Phi_n^{InGaN}(z=l), \tag{2.4a}$$

$$\Phi_n^{GaN}(z=l+L) = \Phi_n^{InGaN}(z=l+L), \tag{2.4b}$$

$$\frac{1}{m_e^{GaN}}\frac{\partial}{\partial z}\Phi_n^{GaN}(z=l) = \frac{1}{m_e^{InGaN}}\frac{\partial}{\partial z}\Phi_n^{InGaN}(z=l), \tag{2.5a}$$

$$\frac{1}{m_e^{GaN}}\frac{\partial}{\partial z}\Phi_n^{GaN}(z=l+L) = \frac{1}{m_e^{InGaN}}\frac{\partial}{\partial z}\Phi_n^{InGaN}(z=l+L), \tag{2.5b}$$

2.3 Optical properties in single QW

Based on the framework of the compact density matrix, the linear (α^1), third-order nonlinear (α^3) and total optical absorption coefficients (α^{Tot}) are given analytically by the following expressions [28]:

$$\alpha(\omega)^{(1)} = \omega\sqrt{\frac{\mu}{\varepsilon_0\varepsilon_r^*}}\frac{\Gamma_{fi}|M_{fi}|^2\rho}{(E_{fi}-\hbar\omega)^2+(\hbar\Gamma_{fi})^2}, \tag{2.6}$$

$$\alpha(\omega,I)^{(3)} = -\omega\sqrt{\frac{\mu}{\varepsilon_r^*}}\left(\frac{I}{2ncn_r^*\varepsilon_0}\right)\frac{4\Gamma_{if}\hbar\rho|M_{fi}|^4}{\left[(E_{fi}-\hbar\omega)^2+(\hbar\Gamma_{fi})^2\right]^2}\times, \tag{2.7a}$$

$$\left[1-\frac{|M_{ff}-M_{ii}|^2}{4|M_{fi}|^4}\frac{3E_{fi}^2-4\hbar\omega E_{fi}+(\hbar\omega)^2-(\hbar\Gamma_{if})^2}{E_{fi}^2-(\hbar\Gamma_{if})^2}\right], \tag{2.7b}$$

$$\alpha^{total}(\omega,I) = \alpha(\omega)^{(1)} + \alpha(\omega,I)^{(3)} \tag{2.8}$$

The incident electromagnetic wave intensity, the relaxation time between implied-states, and the electron density in the well region used in this study are given by $I = 8.10^{10}Wm^{-2}, \Gamma_{fi} = \frac{1}{\tau_{fi}} = 5.10^{12}s^{-1}$, and $\rho = 2.10^{22}cm^{-3}$, respectively.

2.3.1 ISB and BTB electron transition energy in single QW

In low-dimensional systems, the optical absorption is related to two types of transitions: ISB and BTB optical transitions. The variation of the electron transition's energy (ΔE_{fi}) associated with both transitions is depicted in Fig. 2.2. To simplify our numerical calculations, we used the effective units, i.e, the effective Bohr radius $\left(a_b^* = \frac{\varepsilon_0 \hbar^2}{m_b^* e^2}\right)$ as the unit of the width ($\approx 2.27nm$). Fig. 2.2 displays the energy difference between implied states

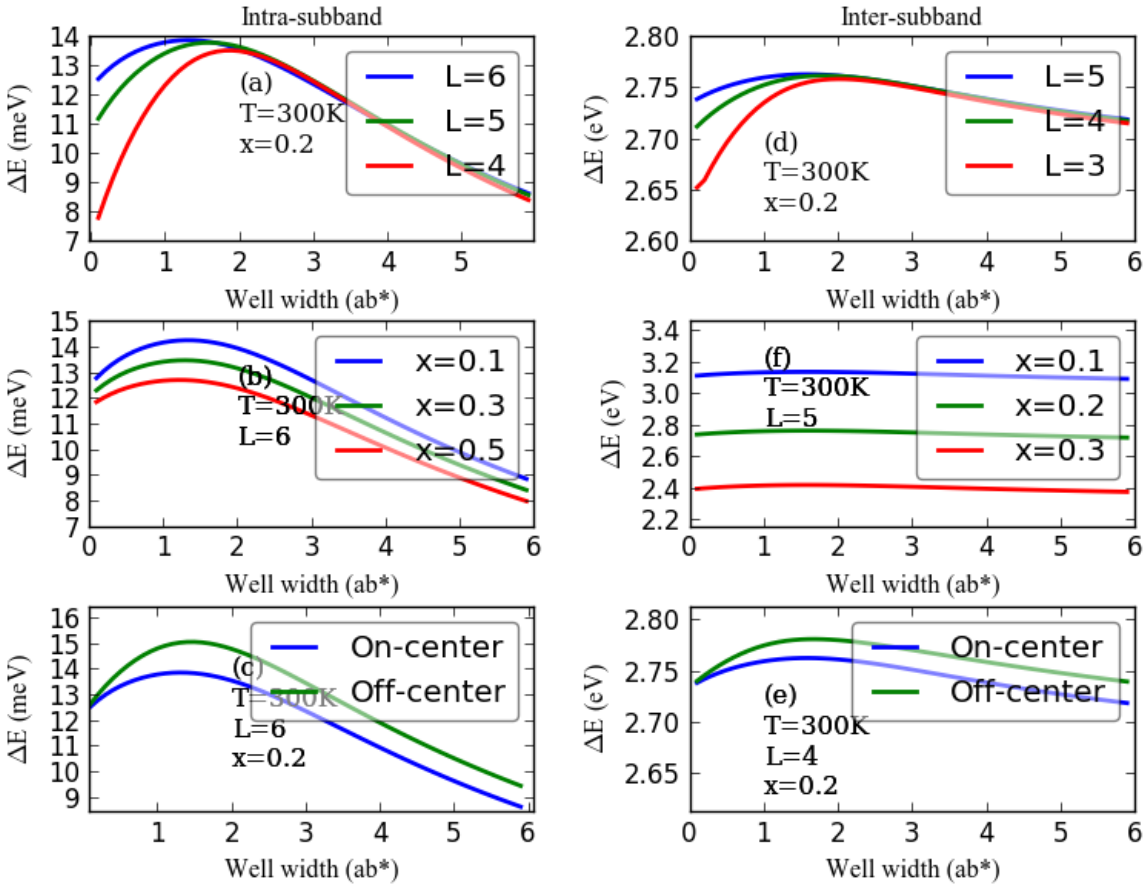


FIGURE 2.2: The variation of the difference energies between the bound electronic-states in single QW versus the well width under the effects of the barrier width, the *In*-concentration, and the impurity-position in the structure [30].

as a function of the QW thickness for two different values of the Indium concentration, the barrier region width and the impurity's position for both transitions. Two cases are investigated concerning the ISB ($1s-2p$), and electron-hole ($1s_e-1s_h$) transitions. For all transitions, it is clear that with increasing the well size the difference energy presents two behaviors limiting by a critical value of the thickness structure.Regardless all the parameters, the the critical value is obtained around the effective Bohr radius. One can

observe from panels (a and b) that for fixed values of chemical structure and well size, ΔE is more affected for the thin well corresponding to strong regime confinement. Also, it is important to mention that with increasing the barrier size the difference energy increases too. For instance, the enhancement rate is about $5 - 10$ meV for narrower well. It appears from panel (b) that as the Indium concentration inside the well increases, ΔE is dropped for a fixed value of the barrier size and for all well size. This can be explained by the fact that with increasing the Indium fraction the potential barrier augments which improves the confinement phenomena and then ΔE can only decreases. Notice that for the BTB transition panel (f), the drop is masked by the band gap energy. For this reason, ΔE appears to be non sensitive to the well size. The same figure (c and e) shows that the displacement of the impurity has a great impact on the electronic states for all well size. It is shown that as the impurity is moved away along the growth axis from the center, ΔE revealed an important improvement.

2.3.2 Dipole matrix-element in single QW

The transition dipole matrix-element or transition moment, usually denoted M_{fi} or $(D.M.E)$ for a transition between an initial state (i), and a final state (f), represents the electric-dipole-moment associated with the transition between the two different states. Generally, the dipole matrix-element is a complex vector quantity that includes the phase factors related with the two implied states. Its direction provides the polarization of the possible transition, which determines how the system will interact with an electromagnetic wave of a given polarization, while the square of the magnitude gives the strength of the interaction due to the distribution of charges within the system. According to the expressions of the optical absorption coefficients, we can make sure that the dipole matrix element is one of the important parameter involved in the optical absorption phenomena and it is the key ingredient in estimation of emission and/or absorption. The results regarding $|M_{fi}|$ as function of the QW thickness concerning the composition, barrier width, and impurity's position are presented in Fig. 2.3. Notice that the same result is obtained for $|M_{fi}|$ corresponding to BTB optical transitions. A previous study has showed that the square of dipole matrix element increases versus the QD radius and that this physical parameter is more important in large dot than in small dot. For a fixed QD radius, $|M_{fi}|$ decreases nonlinearly and with increasing the

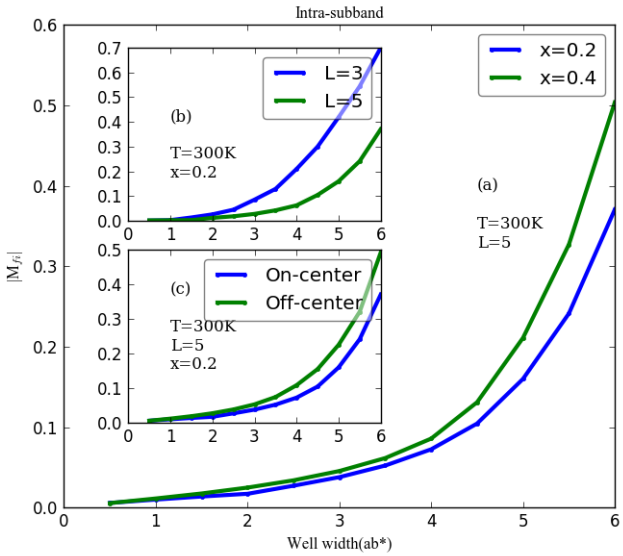


FIGURE 2.3: The dipole matrix-element as a function of the (GaN/(In,Ga)N/GaN QW thickness for two different values of the $In-$compositions, barrier's size, and impurity's position.[30].

dot's radius, this quantity tends a saturation regime corresponding to the (In;Ga)N bulk limit[24]. The main characteristic is that $|M_{fi}|$ increases versus the well width for all values of compositions, barrier width, and impurity positions. As the Indium composition increases, $|M_{fi}|$ is found to be enhanced, whereas, it is dropped with increasing the barrier size. It is also shown that $|M_{fi}|$ is improved as the impurity is moved far away from the center of structure, which is due to the improvement in the overlapping between electron states within the QW.

2.3.3 Optical absorption in single QW

According to the equations (2.6;2.7a; 2.7b; 2.8), the variation of the energy difference (ΔE_{fi}) as well as the dipole matrix-element between the bound electronic states (M_{fi}) under the effect of the size of the structure, the composition of indium in the ternary alloy $(In_xGa_{1-x}N)$ would lead directly to the change of the the ISB and BTB transition energies and consequently the OACs. I.Karabulut et al. have demonstrated that an increase of the position of the impurity and/or the quantum dot radius red-shifts the peak positions of the total absorption coefficient and drops the maximum of the total OAC [46].

2.3.3.1 ISB optical absorption

The study of ISB transitions in QWs has been an interesting subject of investigation. This significant interest is due to their important and fundamental characteristics such as: a large dipole moment, an outstanding tunability of the transition wavelengths, and an ultra-fast relaxation time between electron energy levels.

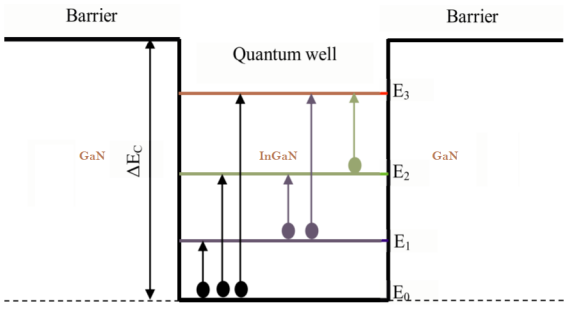


FIGURE 2.4: Conduction Band of a $(GaN/InGaN/GaN)$ single QW structure showing the energy levels and possible ISB optical transitions (the original figure has been modified).[19].

The total optical absorption coefficient (α^{Tot}) related to ISB transitions as a function of the incident photon energy ($\hbar\omega$) is reported in Fig. 2.5. The effects of structure size, impurity position and In-compositions in the ternary alloy have been investigated. According to this figure, the main result is that the $\alpha^{(Tot)}$ is not monotonic and presents a maximum value for a critical incident photon energy governed by the above cited parameters.

It is shown that with increasing the well width ($l : 0.5 \rightarrow 1.5$) and the barrier width ($L : 3 \rightarrow 5$), a considerable jump up of $\alpha^{(Tot)}$ amplitudes of the ISB transitions is observed(see panels(a) and (b)). This can be explained by the competition of two parameters. (M_{fi}) increases which enhancing the amplitude while (ΔE_{fi}) increases also which induces a diminishing of the amplitude. These parameters act in the opposite sense but our results depict that impact of (ΔE_{fi}) is masked by that of $|M_{fi}|$. We can also affirm that the third order nonlinear optical absorption coefficient is also responsible of this behavior. In addition, as we can see from panel (c) that, the both the amplitudes as well as the positions of the $\alpha^{(Tot)}$ have been affected with the increase of the Indium compositions in $(In_xGa_{1-x}N)$ $(x : 10\% \rightarrow 30\%)$. It can be observed also that the increasing of the In-concentration inside the well induces a strong red-shift of the absorption spectra

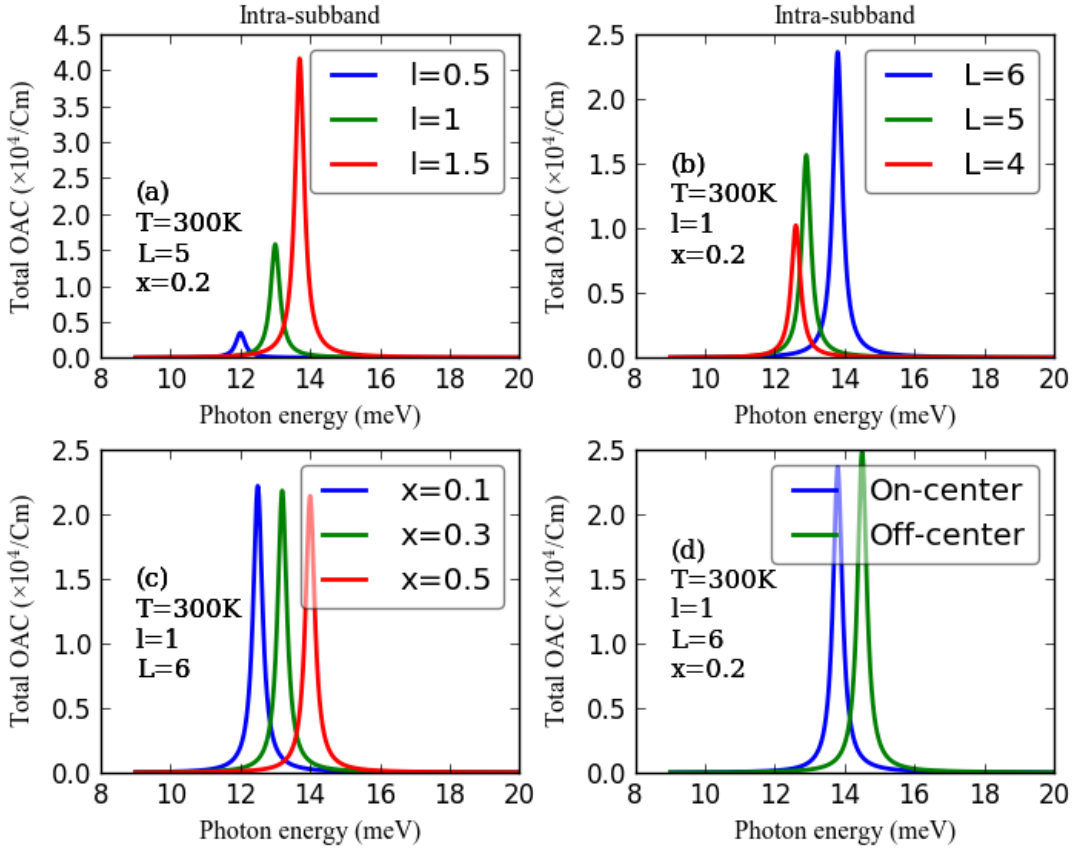


FIGURE 2.5: The change of the total optical absorption spectra of BTB transition as a function of the incident photon energy of InGaN/GaN single QW under the effects of In-compositions, size and impurity.[30].

and a slight drop of their amplitude. These results are in perfect conformity with those presented above related to ΔE_{fi} and $|M_{fi}|$. This is can be explained by the fact that with increasing the indium-compositions, the quantum confinement inside the well becomes important and then the transition's energy increases. However, the same panel (d) reveals also that the absorption phenomenon is more marked for the off-center impurity than for the on-center one. This can be assigned to the fact that as the impurity is moved far away the structure center the Coulomb interaction can only diminish and then the electron less attracted can be excited by the absorption of the incident photon more that the on-center one. Consequently, It can be seen that the In-concentration in the ternary has a great influence on the absorption spectra. As can be seen from panel(c), the absorption spectra are redshifted according to the In-composition. The physical reason is that when the In-fraction increases, the band gap energy dropped.

For instance, this latter is almost 3.42 eV and 2.67 eV for $x = 0.1$ and $x = 0.2$ respectively. On the other hand, it is clearly seen that the amplitude diminishes as a function of the In-composition. It should be notice that as the In-composition is enhanced $|M_{fi}|$ increases and ΔE_{fi} decreases which induces an amplitude enhancement but our results show a behavior contrary to that expected. The only explanation of this behavior can be assigned to the augmentation of the third nonlinear component of the absorption coefficient. Panel (d) reveals a weak dependence of the absorption coefficient on the impurity displacement. One can see that as the impurity is displaced far away the structure center the absorption spectra are slightly affected. This is in good agreement with the results in Fig.2.2 and Fig.2.3.

2.3.3.2 BTB optical absorption

This optical recombination mechanism in optoelctronic devices can be affected by the presence of an impurity atom (donor or acceptor), the chemical compositions in the quantum wells and/or the shape, and QW's thickness. BTB optical absorption as a function of the incident photon energy ($\hbar\omega$) in Fig. 2.6. According to this figure, the principle result is that the $\alpha^{(Tot)}$ is not monotonic and presents a maximum value for a critical incident photon energy governed by the above cited parameters as we discussed before in case of ISB optical transitions. It is shown that with increasing the well width ($l : 0.5 \rightarrow 1.5$) a slight blue-shift is reported in panel(a). This result can be explained by fact that the particle energies are masked by the band-gap energy. A considerable jump up of α^{Tot} amplitude is also observed. This can be explained by the competition of two parameters as we discussed in the previous subsection. $|M_{fi}|$ increases which enhances the amplitude while ΔE_{fi} increases also which induces a diminishing of the amplitude. These parameters act in the opposite sense but our results depict that the impact of ΔE_{fi} is masked by that of $|M_{fi}|$. We can also affirm that the third non-linear absorption coefficient is also one of the main responsible of this behavior. The same figure, panel(d) reveals also that the absorption phenomenon is more marked for the off-center impurity than for the on-center one. This can be assigned to the fact that as the impurity is moved far away the structure center the Coulomb interaction can only diminish and then the electron less attracted can be excited by the absorption of the incident photon more that the on-center one. From panel(c), it can be observed also that the increasing of

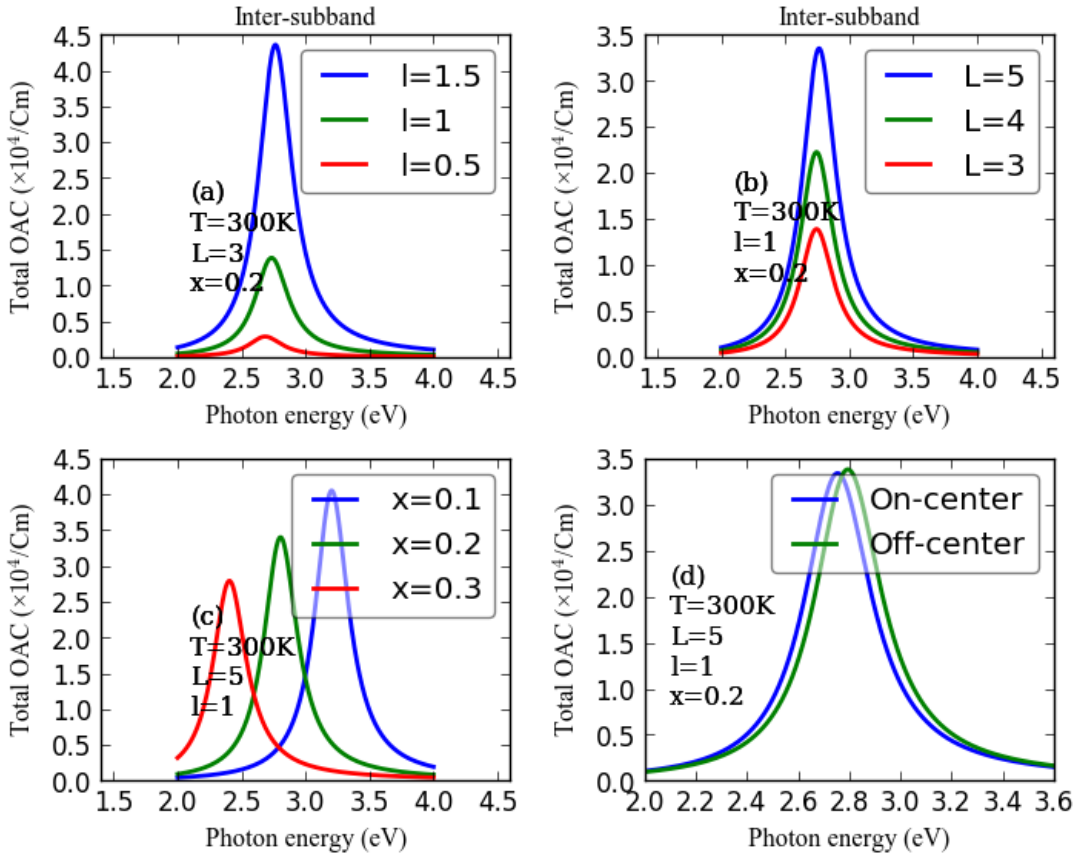


FIGURE 2.6: The change of the total optical absorption spectra of BTB transitions as a function of the incident photon energy of InGaN/GaN single QW under the effects of In-compositions, size and impurity.[30].

the In-concentration inside the well induces a strong red-shift of the absorption spectra and a slight drop of their amplitude. These results are in perfect conformity with those presented above related to ΔE_{fi} and $|M_{fi}|$. The same figure, panel(b) shows that the barrier width has also a great influence on the absorption spectra. It is obvious that the optical absorption spectra are red-shifted according to the barrier width accompanied with a noticeable enhancement of their amplitude. In addition, It can be seen that the well width has a great influence on the absorption spectra. As can be seen from panel(a), the absorption spectra are blue-shifted according to the In-composition. The physical reason is that when the In-fraction increases, the band gap energy dropped. For instance, this latter is almost 12 meV and 14 meV for $l = 0.5$ and $l = 1.5$ respectively. On the other hand, it is clearly seen that the amplitude enhanced as a function of the well/barrier widths (panels (a) and (b)). It should be notice that as the In-composition is enhanced $|M_{fi}|$ increases and ΔE_{fi} decreases which induces an amplitude enhancement

but our results show a behavior contrary to that expected. The only explanation of this behavior can be assigned to the augmentation of the third nonlinear component of the absorption coefficient. However, the absorption spectra are blue-shifted according to the In-composition. This can be understood as follows: with increasing the In-compositions in the well region, the quantum confinement inside the well increases as well which leads to a blue-shift. Also, panel(d) reflects a weak dependence of the absorption coefficient on the impurity displacement. One can see that as the impurity is displaced far away the structure center the absorption spectra are slightly affected (blue-shifted) and the amplitude are enhanced as well as it is expected.

2.4 Optical absorption and refractive index in IPQW and ITQW

Quantum confinement potential shape such as inverted triangular QW (ITQW) and inverted parabolic QW (IPQW) can have a crucial role in the change of optical absorption in nanostructures. To modulate the influence of confinement on the optical absorption in those systems, we have chosen a parameter (i.e., Ω, σ) that depends on the percentage of In-composition in the well region. This In-compositions dependence of this parameter is given by $\Omega(\sigma) = \frac{x_{max}}{x_c}$. where x_c is the critical value and the x_{max} is the maximal value of indium in the well. For a single quantum well of thickness l and the barrier thickness L. The parabolic confinement potential is given by the following expression,

$$V_p(z) = \begin{cases} \frac{4V_0}{\Omega \times l^2}\left(z - L - \frac{l}{2}\right)^2, & L \leqslant z \leqslant L + l \\ V_0, & \begin{cases} 0 \leqslant z < l \\ L + l < z \leqslant l + 2L \end{cases} \\ \infty, & \begin{cases} z \leqslant 0 \\ z \geqslant 2L + l \end{cases} \end{cases} \tag{2.9}$$

The triangular confinement potential is given by the following expression,

$$V_t(z) = \begin{cases} \frac{V_0}{\Omega} \times \left[1 - \frac{2}{l}\left(z - L - \frac{l}{2}\right)\right], & L \leqslant z < L + l/2 \\ \frac{V_0}{\Omega} \times \left[1 + \frac{2}{l}\left(z - L - \frac{l}{2}\right)\right], & L + l/2 \leqslant z \leqslant l + L \\ V_0, & \begin{cases} 0 \leqslant z < l \\ L + l < z \leqslant l + 2L \end{cases} \\ \infty, & \begin{cases} z \leqslant 0 \\ z \geqslant 2L + l \end{cases} \end{cases} \tag{2.10}$$

where $V_0 = 0.7\left[E_g^{GaN}(T) - E_g^{InGaN}(T)\right]$ and $\Omega = \frac{x_{max}}{x_c}$.

TABLE 2.2: Table of the physical constants

Parameter	Value
a^*(nm)	2.73
R^*(meV)	28.4
x_{max}	0.2

The ingredients used to compute this study are the same as those used previously in table2.1. In this case, the height of the potential barrier is inversely proportional to this parameter (V_0/Ω). Thus, the increase in the composition inside the well leads directly to the decrease of Ω and then the height of the potential barrier will only increases. Consequently, the change of this parameter causes a variation in the degree of quantum confinement inside the well and therefore a deformation of the wave functions. These physical behaviors will simultaneously affect both the transition energy and the optical absorption in the studied system.

2.4.1 Shape and In-composition effects

2.4.1.1 Electron wave functions

Fig.2.7 depicts the schematic diagram of the confinement potential profile as well as the ground and the two lowest excited-states as a function of the growth direction for two different nanostructures, inverted triangular QW (ITQW) and inverted parabolic QW (IPQW). One can see from this figure that, for both ITQW and IPQW structures, the decrease in Ω has deformed the quantum confinement diagram and the wave functions

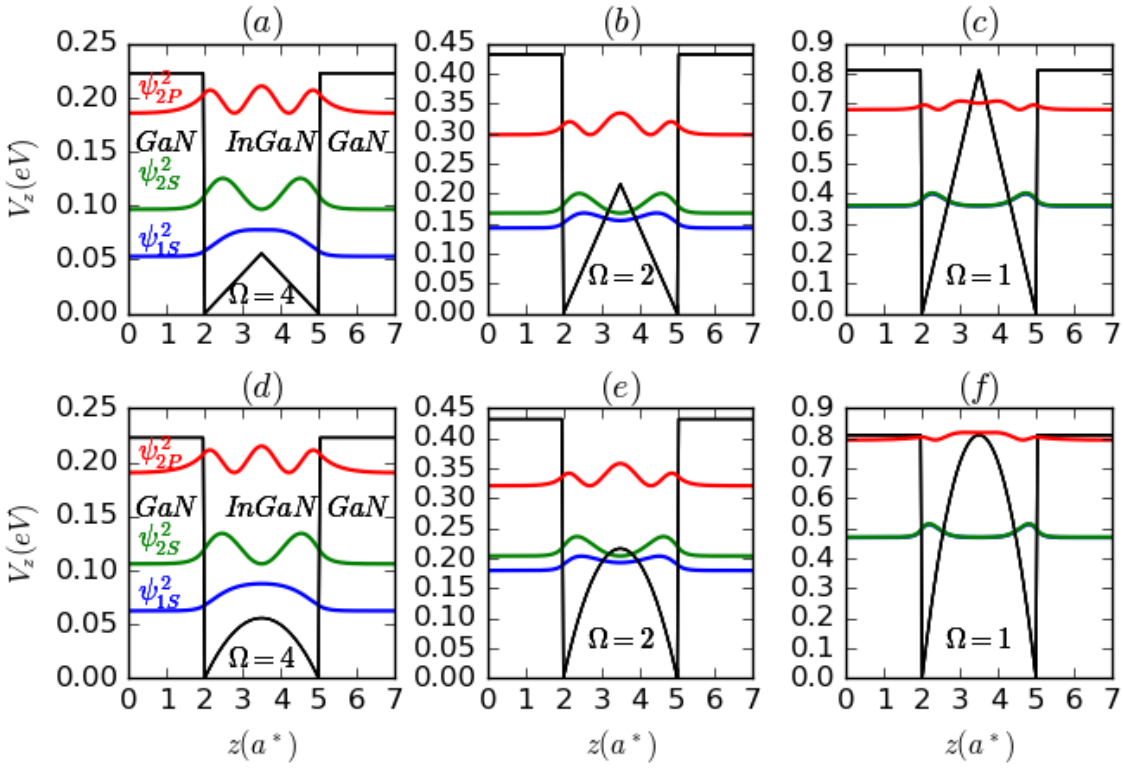


FIGURE 2.7: The confinement potential profile as well as the square of lowest and two low-laying electron wave-functions versus z-axis for three different values of $\Omega = (4, 2, 1)$ considering two QW's shapes: ITQW and IPQW

as well. It is also shown that the weaker Ω is, the higher the quantum confinement becomes, especially at the center of the wells. This forced the electron probability densities of all considered states to become more localized near the edges of the QW than at the center especially that of the corresponds to the ground-state. It is also noticed that, the decrease of Ω reduces the splitting energy between $1s$ and $2s$ states for nanostructures. This is due to the fact that, smaller Ω is, the stronger the confinement become in the QW, as a result, the interaction between electron states becomes very important.

2.4.1.2 Electron transition energy

Fig.2.8 shows the variation of electron transition energy corresponding to the transition $1s-2p$ (i.e., Δ_{20}) with respect to well's width ($x-axis$) and temperature ($y-axis$) considering two types of confinement potential profile (i.e., IPQW and ITQW). For a fixed barrier widths, it is clearly seen that, for both considered structures, with increasing the well's thickness, ΔE_{20} rises to reach a maxima in a critical well width around 1.5 then falls to reach a minima for wider QW. This is due to the fact that, with increasing the

well's width, the particle starts to feel the neighbor material (e.g., GaN) until it equals the critical width, the particle starts to penetrate in the barrier material which explains the decrease in the transition energy in both cases. However, with the increase of the In-composition (i.e., Ω), the confinement becomes stronger and then the transition energy can only augment.

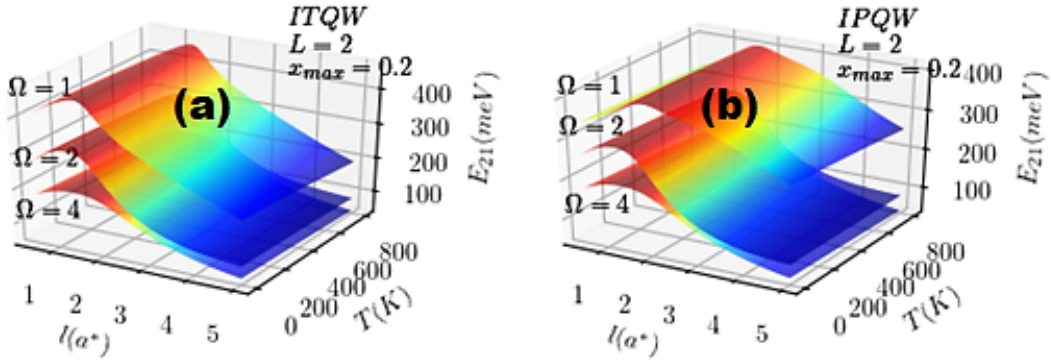


FIGURE 2.8: The variation of the lowest and two low-laying energy levels in both ITQW and IPQW versus the well width (x-axis) and temperature ($y-axis$) with a fixed barrier width ($L = 2$) and $x_{max} = 0.2$ for three different values of $\Omega = (4, 2, 1)$

2.4.2 Optical absorption and refractive index change

It is important to notice that in this study, the used parameter σ is equal to that used above ($\Omega = \frac{x_{max}}{x_c}$). It is noticed that with increasing the QW width, E_{20} demonstrates the same behavior for both IPQW and ITQW. It raises until it reaches a maximum at a critical QW width then it decreases to reach a steady state for weak quantum confinement regime (large QW). Also, it shows a slight decreases with the increase in temperature as well due to the decrease of the effective-mass and the increase of the dielectric constant. Moreover, E_{20} increases with the decrease in Ω due the increase in the quantum confinement strength with raising the percentage of indium in the well region. This can be confirmed by blue-shift of the positions of the linear, nonlinear, total optical absorption, and the refractive index change appears in Figs.2.9, 2.10 and 2.11, respectively. According to the same figures, the amplitude of the resonance peaks of both the optical absorption coefficients and the refractive index change have been improved with the decrease of the parameter Ω. This is explained by the fact that, when the In-composition increases, the dipole matrix element raises, as a result, the maximum of the resonance peaks enhanced. However, it is important to notice that,

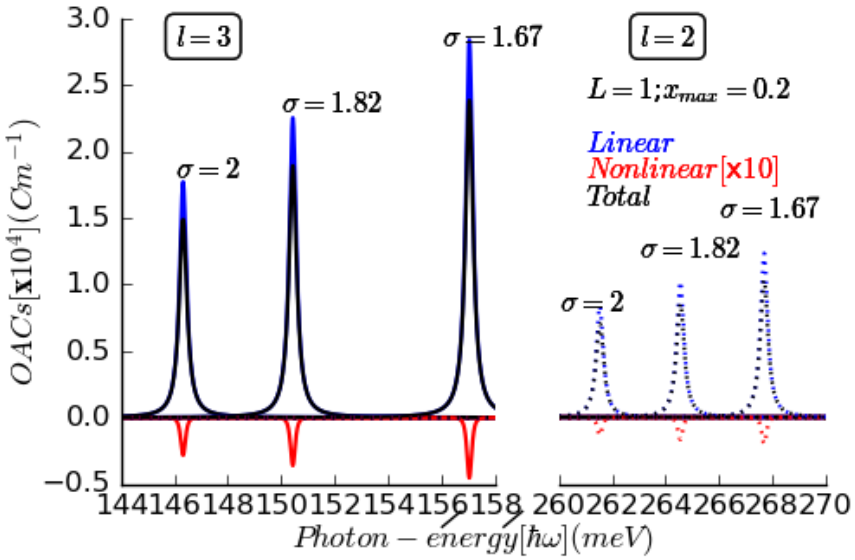


FIGURE 2.9: The variation of the optical absorption coefficients $((\alpha^1), (\alpha^3)$ and $(\alpha^t))$ versus the incident photon energy for three different values of $\sigma = (2, 1.82; 1.67)$ in single PQW taken into account the well thickness effect

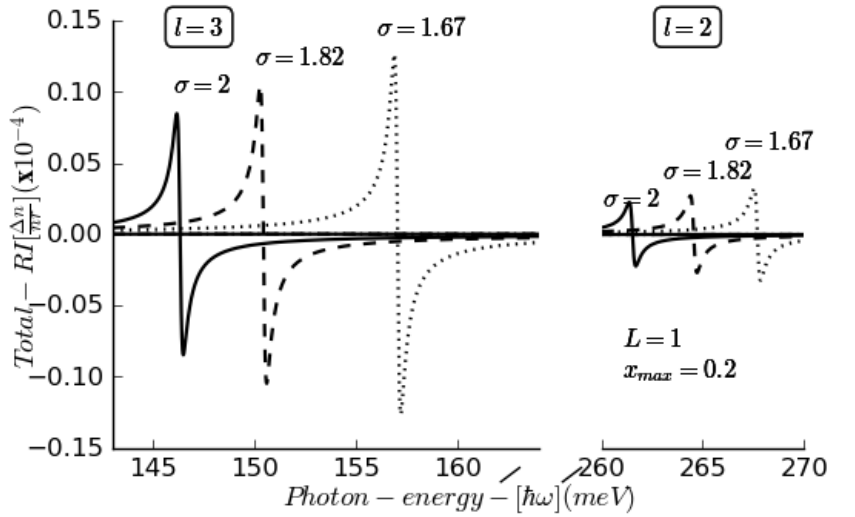


FIGURE 2.10: The variation of the refractive index change (RIC) versus the incident photon energy for three different values of $\sigma = 2(1.82; 1.67)$ in single PQW taken into account the well thickness effect

the potential profile has a significant impact on the optical properties of QWs. Panel (a) shows that referring to ITQW, IPQW OACs are red-shifted while its amplitudes are slightly decreased. In addition, Panel (b) demonstrates that, the incident electromagnetic intensity ($I = \frac{2n_r^*}{\mu_0 c}|E|^2$) has a remarkable influence on the optical properties of QW, particularly on the magnitude of the optical absorption coefficients. From the same figure, it can be seen that, for high incident electromagnetic intensity, the total optical

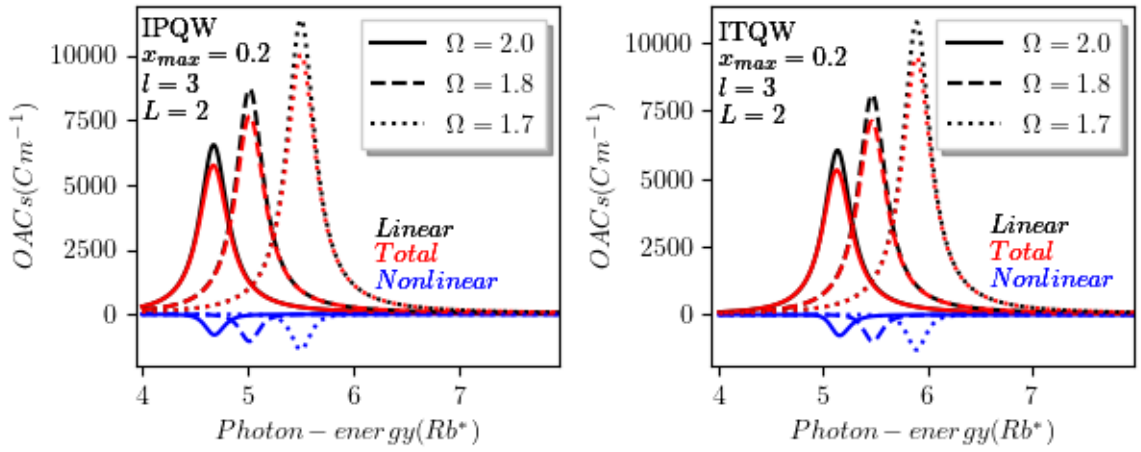


FIGURE 2.11: The variation of the optical absorption coefficients $((\alpha^1), (\alpha^3)$ and $(\alpha^t))$ versus the incident photon energy for three different values of $\Omega = (2, 1.8; 1.7)$, two types of potential profile have been considered: IPQW (left) and ITQW (right)

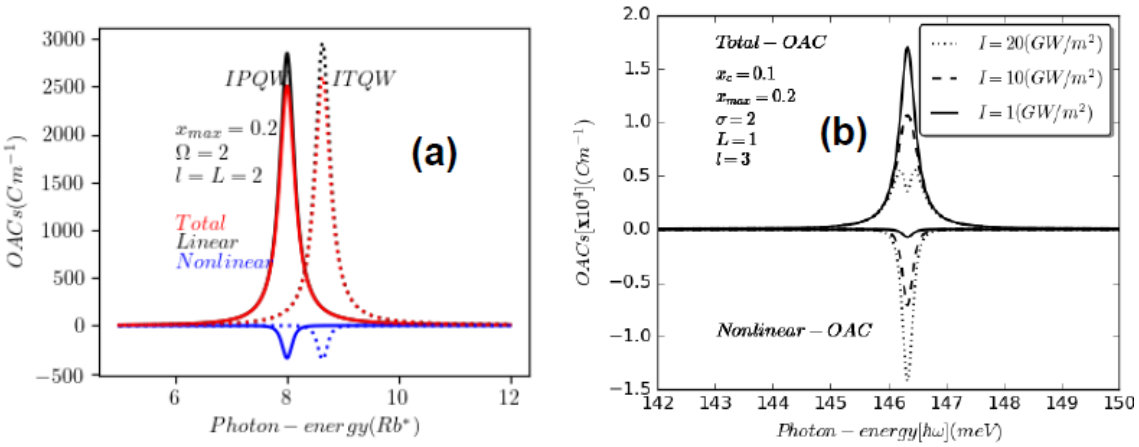


FIGURE 2.12: The variation of the optical absorption coefficients $((\alpha^1), (\alpha^3)$ and $(\alpha^t))$ versus the incident photon energy. Two effects have been considered: Potential profile shape (a) and incident electromagnetic intensity (b)

absorption peak becomes a double peaks with two resonance energy values.

2.5 Conclusion

Through this chapter, we discussed the optical absorption associated with ISB and BTB optical transitions in single QW. We explored the effect of size, indium concentration and the impurity position within the QW. We shown those parameters have a significant impact on the electron transition energy (ΔE_{fi}), the square of dipole matrix-element ($|M_{fi}|^2$) and total optical absorption coefficient ($\alpha^{(Tot)}$) related to ISB and BTB transitions. We ended the chapter by showing the influence of the shape of the potential

barrier and the incident electromagnetic intensity on the electron transition energy as well as the position and amplitude associated with the linear, nonlinear and total optical absorption coefficients.

Chapter 3

ISB optical absorption in RDQW: Coupling and temperature effects

Sommaire

3.1 Introduction 55
3.2 Theoretical framework 55
3.3 Temperature and coupling effects 57
3.3.1 Electron wave functions 57
3.3.2 Electron energy levels 58
3.3.3 Electron transition energy 60
3.3.4 The oscillator strength 61
3.4 ISB total optical absorption 63
3.5 Conclusion 65

3.1 Introduction

Double-quantum-well nonstructures (DQWs) or multi-quantum-well structures (MQWs) are widely used in optoelectronics such as solar cells and lasers because they offer the possibility of tunneling of the particle through the separation barrier[81, 89]. For these reasons, those systems have been the subject of intensive theoretical and experimental investigations especially for optical absorption coefficients[53, 68, 36]. In this chapter, we investigated the ISB optical absorption in rectangular double quantum well structure (RDQWs) taking into account the coupling and temperature effects. First, we started with the presentation of the theoretical framework and then the discussion of the results then we shown the influence of coupling and temperature on the electron energy levels as well as energy transition and the oscillator strength. Secondly, we investigated the effect of those parameters on the total optical absorption coefficient ($\alpha^{(Tot)}$) related to ISB transitions with respect to the incident photon energy.

3.2 Theoretical framework

Consider a DQWs system that consists of two QWs (i.e. QW1 and QW2) of widths l in InGaN separated by an intermediate barrier of width W and sandwiched by two side barriers in GaN d thickness L. The origin of the coordinates is chosen at the edge of the left side of the structure. A schematic illustration the band structure of the investigated system is depicted in Fig. 3.1. The ingredient used in this study (e.g., band gap energy of GaN and InN, and their effective masses and dielectric constants) are the same used before in the previous chapter.

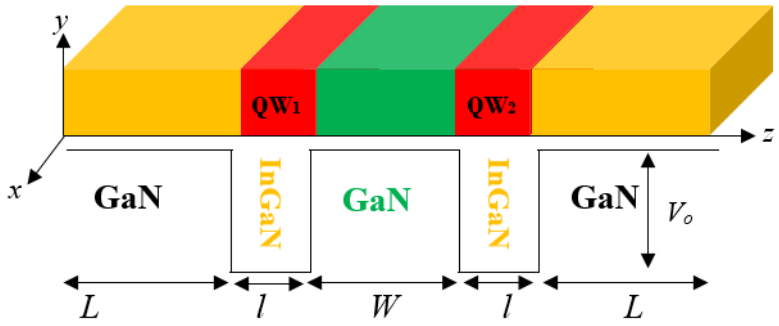


FIGURE 3.1: Schematic diagram of a symmetric unstrained GaN/InGaN SDQWs.

Within the single parabolic band effective-mass approximations, the electron Hamiltonian of the studied system is given by the same expression in the previous chapter (Chap.1: Eq. (**??**) with only the first and second terms). The variation of the the band gap energy of the ternary taking into account of the bowing parameter ($\beta = 3.8$) for 10% of indium-nitride is given as follows:

$$E_g^{In_{0.1}Ga_{0.9}N} = 0.1E_g^{InN} + 0.9E_g^{GaN} - 0.9\beta \tag{3.1}$$

The temperature dependence of the band-gaps energy of InN and GaN are expressed by the following expression:

$$E_g^i(T) = E_g(T = 0K) - \frac{\alpha T^2}{\beta + T} \tag{3.2}$$

where the index i denotes the considered materials either InN or GaN. all the ingredients used in this work are reported in the table2.1. $\alpha(meV/K)$ and $\beta(K)$ of InN(GaN) are respectively given by 0.245(0.909) and 624(830)[29]. The effective-mass and the relative dielectric constant dependence on temperature are respectively given as follows [33, 25]:

$$m^*(z,T) = \begin{cases} \frac{m_0}{1+\frac{C_w}{E_g^w(T)}}, & \text{Inside the QW} \\ \frac{m_0}{1+\frac{C_b}{E_g^b(T)}}, & \text{Outside the QW} \end{cases} \tag{3.3}$$

$$\varepsilon_r^*(z,T) = \begin{cases} \varepsilon_r^{*,GaN}(T) + 6.4x, & \text{Inside the QW} \\ \varepsilon_r^{*,GaN}(T = 300K) \times e^{\left(\frac{T-300}{T^4}\right)}, & \text{Outside the QW} \end{cases} \tag{3.4}$$

where $C_i(eV)$ is a fixed value depends on the chosen material, and it is 14.07(GaN) and 25.50(InN) according to [29].

To solve analytically the Schrödinger equation becomes in such a situation impossible and then the finite difference method (FDM) is adopted. A mono-directional mesh (calculation grid) of 5N+1 points is considered and each layer (Well, barrier) is characterized by a different discretization step. $h_w = l/N, h_c = W/N$ and $h_b = L/N$ are used to characterize respectively the well, intermediate (central) barrier and left and

right barriers. Therefore, the mesh's nodes of the studied structure are given respectively as $z_i = i * h_b, z_i = L + i * h_w, z_i = L + l + i * h_w, z_i = L + l + W + i * h_w$, and $z_i = L + 2l + W + i * h_b$ for $0 < i < N$.

Assuming the function whose derivatives are to be approximated is properly-behaved, by Taylor's theorem. In 1D the Laplace operators are approximated as:

$$\left(\frac{\partial^2 \psi(z)}{\partial z^2}\right)_{z=z_i} = \frac{\psi_{i-1} - 2\psi_i + \psi_{i+1}}{(z_{i+1} - z_i)^2}, \tag{3.5a}$$

$$\left(\frac{\partial \psi(z)}{\partial z}\right)_{z=z_i} = \frac{\psi_{i+1} - \psi_i}{(z_{i+1} - z_i)}, \tag{3.5b}$$

It is very important to notice that the total optical absorption coefficients depends essentially on the transition energy (ΔE_{fi})as well as the dipole-matrix-element ($|M_{fi}|^2$). The incident electromagnetic intensity, the relaxation time between implied states, and the electron density in the QW are given by $I = 4.10^{10} W m^{-2}, \Gamma_{fi} = \frac{1}{\tau_{fi}} = 5.10^{12} s^{-1}$, and $\rho = 2.10^{22} cm^{-3}$, respectively. The calculations are performed for an impurity located in the middle of the intermediate (central) barrier of the hetero-structure ($z_0 = L + l + \frac{W}{2}$). Without loss of generality, the structure sizes are chosen in order to have all localized bound states within the QW. Furthermore, the infinite potential height located at $z = 0$ and $z = 2L + W + 2l$ takes in consideration the real situation where DRQWs-based device is immersed in dielectric environment, air or vacuum.

3.3 Temperature and coupling effects

3.3.1 Electron wave functions

Fig.3.2 shows the probability densities of the lowest and first five excited bound states localized in RDQWs for two different temperatures. The finite potential barrier between GaN and InGaN makes the electron tunneling possible between the coupled QWs through the intermediate barrier. For more visibility, each probability density's curvature is translated to be placed on its corresponding eigen-energy. The potential barrier is equal respectively to 0.891 and 0.901 eV for T=500K and 100K. It is clearly observed that with increasing the temperature the probability densities are found to be tighter and their corresponding energies dropped. It appears that as the excited level

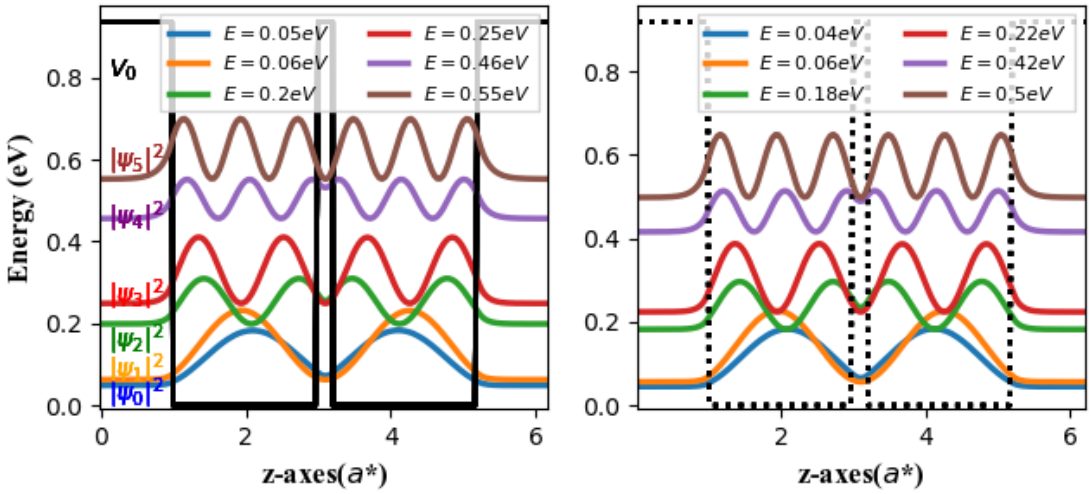


FIGURE 3.2: Energy levels as well as their associated wave-functions in symmetric $GaN/In_xGa_{1-x}N$ coupled double quantum wells (RDQWs) as a function of the growth direction for two values of temperature: 100K (left-panel) and 500K (right-panel) with $l = 2L = 2a_b^*; W = 0.2a_b^*; x = 20\%$[29].

increases the energy drop is more pronounced versus the temperature. For examples, the shrink is about 0.07 meV for the ground-state while it is 0.58 meV for the last low-lying excited state. For RDQWs with thin central barrier, the tunneling phenomenon through this later induces the degeneration of the single state into the doublet states with symmetric (ψ_0) and antisymmetric (ψ_1) states.

3.3.2 Electron energy levels

The change of the probability densities of different bound conduction-band electron states under the effect of temperature (T) and coupling barrier leads to the change in the energy levels as well as the transition's energy between implied electron-states in the conduction band and then the change in the optical absorption in RDQWs. Fig.3.3 depicts the variation of all bound states energies in the RDQWs versus the heterostructure depth for two different values of temperature. In Fig.3.3(a) are presented the results of all states according to the InGaN wells width for $L = 2$ and $W = 0.5$. As expected, the energies decrease according to the well width which can be assigned to the geometric confinement weakness. It is clearly seen that the high level excited states are more affected than the others. As the well width increases all energies tend to their InGaN bulk values corresponding to the continuum state. The influences of the central barrier is presented on the panel (b) of Fig.3.3 for $L = l = 2$. Two different behaviors limited by

a crossover value (W_c) are obtained according to the coupling barrier's thickness. For

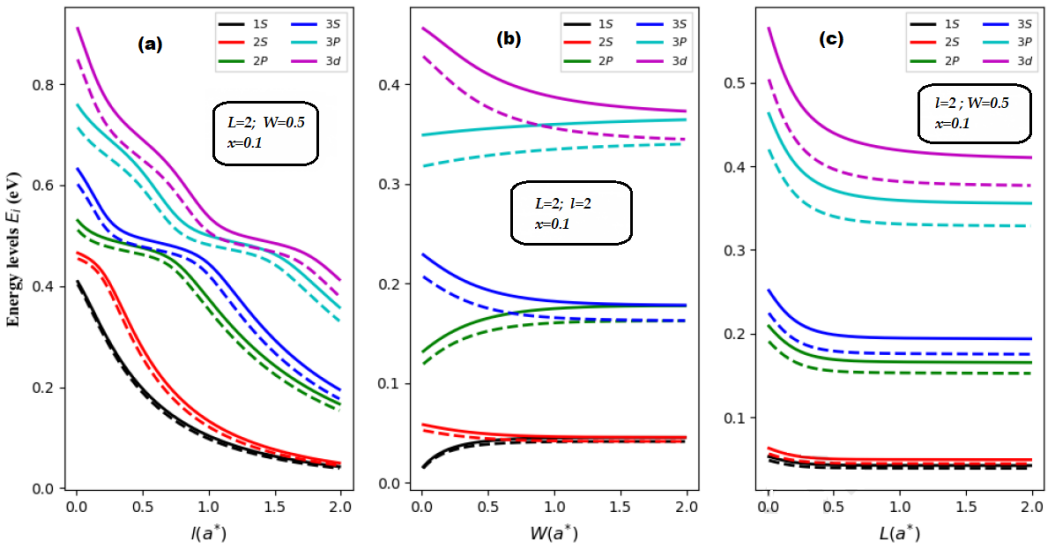


FIGURE 3.3: Energy levels of lowest and five low-lying states as a function of the well width (a), Coupling barrier width (b) and extreme barriers width (c) for InGaN/GaN based DRQWs. The effect of temperature is included [Solidlines: T=100K; Doshedlines: T=500K][29].

thick central barrier ($W > W_c$), the energy levels remain intact with increasing the coupling barrier width while for the thin ($W < W_c$), 1s, 2p and 3p (2s, 3s and 3d) energies increase (decrease) as a function of the coupling barrier size. One can observed that with increasing this latter, the energy difference between 1s-like and 2s-like (2p and 3s; 3p and 3d) states diminishes to be zero for large central barrier. Such behavior occurred when the size of the central coupling barrier increases and the coupled system tends to two separated QWs with degenerate states. With increasing W, 1s (2s), 2p-(3s) and 3p-(3d) energy states are found to be enhanced (diminished). For thick coupling barrier, the RDQWs system behaves as two independent single QWs with degenerate energies. This is in good conformity with the reported results in references[87, 50]. In panel (c) of Fig.3.3, we reported the obtained results of all state energies with respect of the extreme barriers width for $l = 4W = 2$. All energies show identical decrease converging to the independently behavior for large extreme barriers size. Also, the effect of this later is more remarkable for thin extreme barriers than for thick ones. Independently of structure size, it is obtained that as the temperature increases all states energies are found to fall. The physical reason can be explained by the fact that as the temperature

increases three main effects are obtained: (i) the effective mass decreases, (ii) the relative dielectric constant increases and the potential height decreases. The first effect is responsible of the kinetic energy drop while the second is liable of Coulomb potential enhancement. Our results show that this later is masked by the first (kinetic energy) and the third (Colombian interaction) terms in Eq.**??** given in Chap.1.

3.3.3 Electron transition energy

Based on the Fermi golden rule and the density compact approach, from which the absorption coefficients can be obtained[26], the adequate description of the linear, nonlinear and total absorption coefficient passes through the exact knowledge of the energy difference (ΔE_{fi}) and the electric dipole operator matrix element (M_{fi}) involved directly in oscillator strength expression (**??**).

In Fig.3.4 are reported the results of (ΔE_{fi}) for all implied inter-subband transitions

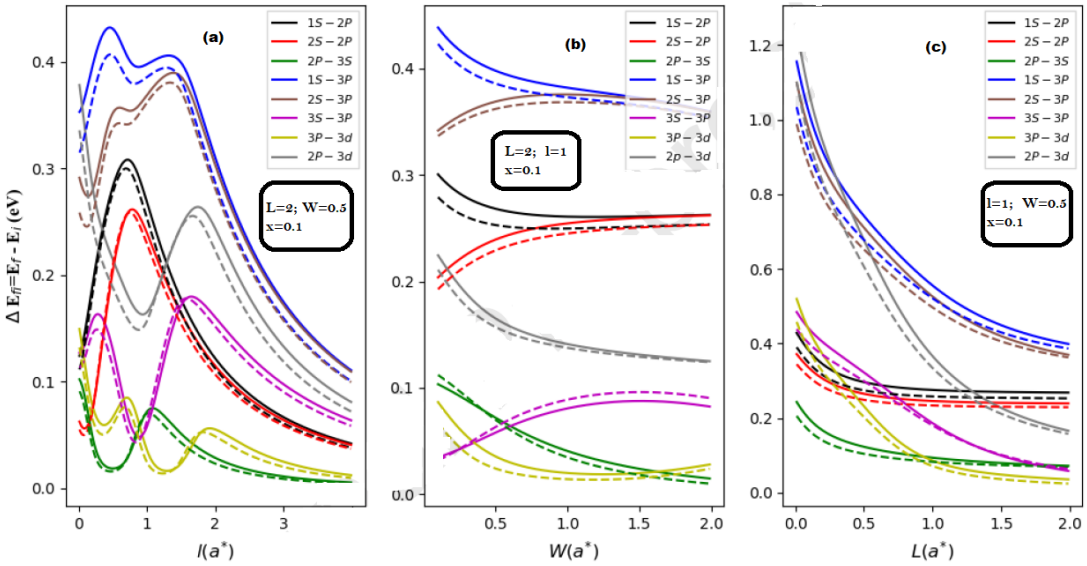


FIGURE 3.4: Energy difference between the allowed states as a function of the well width (a), central barrier width (b) and extreme barriers width (c) for InGaN/GaN based DRQWs. The effect of the temperature is considered. [Solidlines: T=100K; Doshedlines: T=500][29].

according to the hetero-structure size for two different temperatures. One can observe from panel (a) that (ΔE_{fi}) is strongly-dependent well width for both temperatures. For large well, it tends to zero which corresponds to the continuum result as expected. For instance, 1s-2p and 2s-2p transition energies reveal a maximum value for a well width

around 0.8 while 1s-3p and 2s-3p present two local maxima around 1.4 and 0.5. Incidentally, all others show an alternative sequence of minima and maxima for critical values of the well width. In addition, all transition energies are decreasing function of temperature. Two exceptions to such rule, related to (ΔE_{fi}), appeared for 3p-3d and 3S-3P transitions. It is found that in ($1.3 \rightarrow 1.8$) and ($0.9 \rightarrow 1.7$) width's ranges, they show an enhancement with respect to the temperature. These results are in good agreement with the reported ones in Fig.3.3 panel (a). Moreover, panel (b) shows the variation of ΔE_{fi} of all transitions with the change of the central barrier width for L=2l=2. As discussed above in Fig.3.3 (b), it is seen that the central barrier increasing forces the 1s, 2s and 3p levels to higher energies and the 2s, 3s and 3d-ones to lower energies. So, ΔE_{fi} for all allowed transitions can be explained based on the results presented in panel (b) of Fig.3.3. For instance, 3s-3p, 2s-2p and 2s-3p inter-subband transition related energy differences are found to be enhanced with increasing the coupling width compared to drop shown by all others. Additionally, it's observed that the main effect of the extreme (side) barrier width (L) is to reduce 3.3. For instance, it appears clearly that 2P-3d transition is the most influenced by the change of the extreme barrier width compared to all others ones.

3.3.4 The oscillator strength

The oscillator strength (P_{fi}) is one of the most important parameters for the study of optical transitions in low-dimensional systems. It allows us to quantify the probability of absorption of electromagnetic radiation between allowed energy levels. It is given analytically by the equation (3.6).

$$P_{if} = \frac{2m^*}{\hbar^2}\Delta E_{fi}|M_{fi}|^2 \tag{3.6}$$

Fig.**??** displays the variation of the oscillator strength with respect to the structure dimensions considering the influence of both coupling and temperature. The principle characteristic of its variation according to the well width is a significant enhancement except 1s-3p and 2s-3p transitions which remain approximately independent. Panels

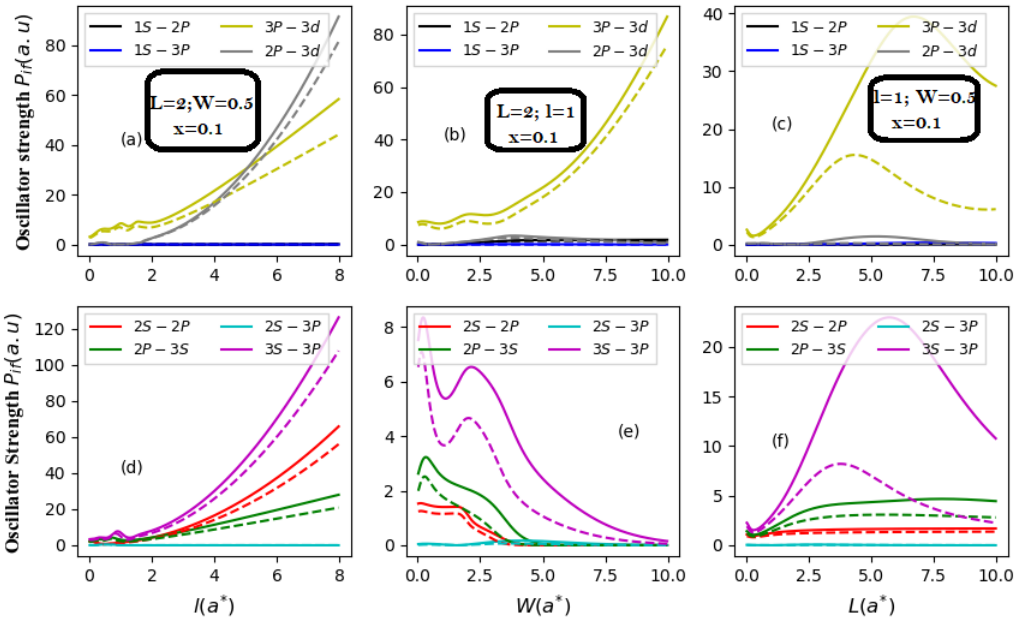


FIGURE 3.5: Oscillator strength of different allowed transitions as a function of the well width (a and d), central barrier width (b and e) and extreme barriers width (c and f) for InGaN/GaN based DRQWs for two different values of the temperature. [Solidlines: T=100K; Doshedlines: T=500][29].

(b) and (e) contain the variation of the oscillator with respect to the coupling (central) barrier width for $L = 2$ and $l = 2$ taken into account two different values of the temperature. We readily see that P_{fi} presents different behaviors, i.e., there is a multiplicity of monotonic and non monotonic variations for different involved transitions. The generally tendency is to vanish for large central barrier except 3p-3d transition. This latter result can only explained by the fact that with increasing W the augment of the dipole matrix element (M_{fi}^2) is more pronounced than ΔE_{fi} decrease. We also report in panel (c) the behavior of the oscillator strength versus the extreme barrier width (L) for $l = 2W = 2$ under the temperature effects. In this case, the general tendency is to exhibit initially a slowly increase to tend to a saturation regime for large barrier even if 3p-3d and 3s-3p transitions show a maximum for a critical value of the side barrier width. Moreover, one can observe that the main impact of the temperature is to shrink P_{fi} in particularly for non monotonic behaviors.

3.4 ISB total optical absorption

After discussing above the obtained results of the energy difference and oscillator strength which are necessary to interpret the optical properties, let us to present and investigate the optical absorption of interest according to the photon energy. For this reason, we choose an unperturbed configuration of $L = 2l = 2$ and on-center hydrogen-like impurity. Primarily, we display in Fig.3.6 the variations of $\alpha^{(Tot)}$ associated with 2s-2p, 2p-3s, 3s-3p and 3p-3d ISB transitions according to the incident photon energy for T=300K and 500K considering the coupling barrier width influences. In such study, we present how the total absorption reacts versus the temperature and coupling barrier width. It is observed that the absorption spectra are strongly depending on the temperature and geometrical coupling. On the one hand, 2s-2p and 3s-3p related-spectra are obtained to shift toward higher energies (Blue-shift) whilst 2P-3S and 3p-3d are observed to move to lower energies (red-shift). The principle reason for such resonance blue-shift (red-shift) is the enhancement (drop) of the ΔE_{fi} according to the geometrical coupling width for a fixed temperature. On the other hand, as can be seen from this figure, with increasing temperature 2s-2p, 2p-3s and 3p-3d (3s-3p) related-absorption spectra are obtained to be red-shifted (Blue-shift). Such behaviors stem from the dependence of ΔE_{fi}, where an optical transition occurs, versus the temperature.
These results are in good conformity with those reported in Fig.3.4. Moreover, from this figure, the TOAC amplitudes are notably diminished with increasing the temperature and the coupling barrier width. These characteristics can be understood based on the results reported in Fig.3.5.

Secondly, Fig.3.7 displays the results obtained for $\alpha^{(Tot)}$ related with 1s-2p, 1s-3p, 2s-3p and 2p-3d ISB transitions versus the incident photon energy considering two different values of temperature and coupling barrier width. In accordance with the results presented in panel (b), apart from 2s-3p transition all spectra are noticeably red-shifted with increasing the coupling width for all temperatures. Also, excepting 1s-3p transition, the $\alpha^{(Tot)}$ amplitudes are enhanced versus the coupling width. Moreover, it can be seen that with increasing temperature for a fixed coupling width value all

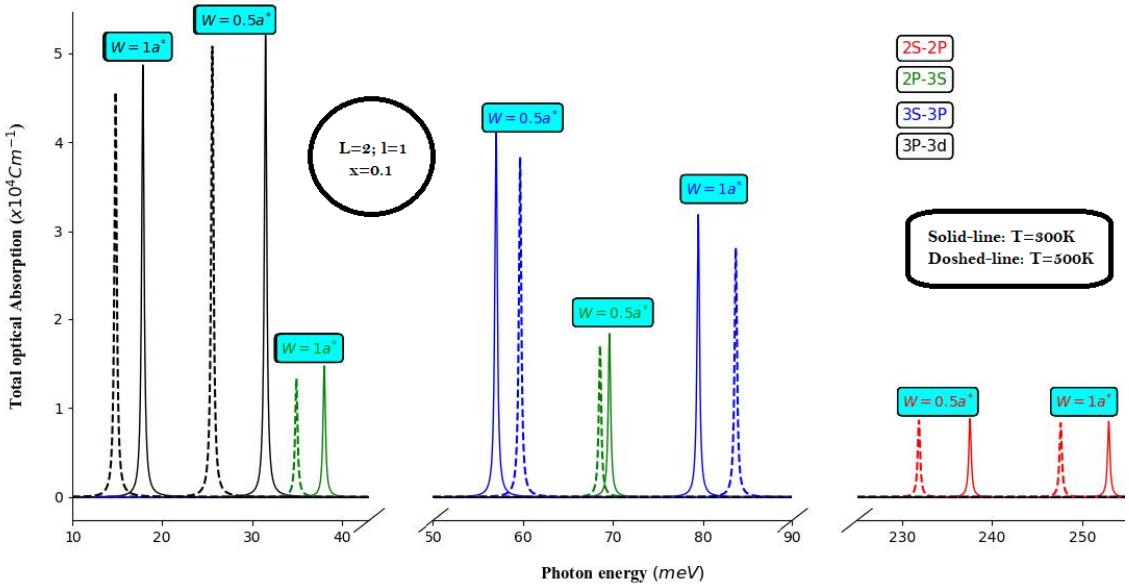


FIGURE 3.6: 2s-2p, 2p-3s, 3s-3p and 3p-3d related total optical absorption as a function of the photon energy for InGaN/GaN based DRQWs for two different values of temperature. The geometrical coupling barrier width impact is introduced.[29].

spectra are moved to lower energies showing an important red-shift. These results are in perfect accordance compared with Fig.3.4. For example, the 1s-3p red-shift is about 6.75 and 5.05 meV as the temperature changes from 300K to 500K for the coupling barrier width equals respectively to 0.5 and 1. As well, it is important to point out that $\alpha^{(Tot)}$ amplitude associated to 1S-2P and 1S-3P ISB transitions are smaller compared to all other transitions. This is in good agreement with the results represented in Fig.3.5.

Generally, our finding results show that the $\alpha^{(Tot)}$ depends quite appreciably on the ISB transition energy and the oscillator strength governed directly by temperature and nanostructure's size which can be used as adequate tools to adjust optical properties. They are in good agreement with those reported above even if some discrepancies remain due probably to intrinsic characteristic of the studied material and mathematical method used in each paper in the one hand and to the impurity ignored generally in the reported works. Related to the absorption properties, it suggested by Dakhlaoui that (Al,Ga)N/GaN-based DQWs nanostructure can be used to design of devices in the range of micrometers[22]. For us, we believe that (In,Ga)N/GaN DQWs can be utilized in the THz domain of electromagnetic spectra as electro-optical modulators, photo-detectors and all optical switches.

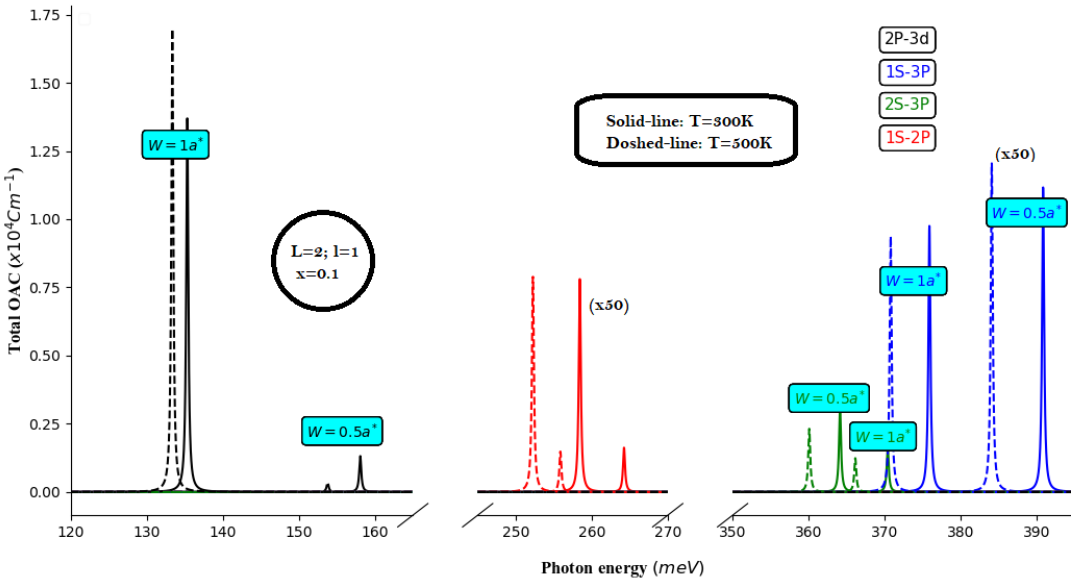


FIGURE 3.7: 1s-2p, 1s-3p, 2s-3p, and 2p-3d related total optical absorption according to the photon energy for InGaN/GaN based DRQWs for two different values of the temperature and two different values of the geometrical coupling barrier width. The 1s-2p and 1s-3p intesubband transitions TOAC are multiplied by 50 for more clarity.[29].

3.5 Conclusion

In this chapter, we have shown the ISB optical absorption in rectangular double quantum well structure (RDQWs) taking into account the coupling and temperature influences. We began with exploring the theoretical framework and then the discussion of the results. In the beginning, we started by showing the influence of coupling and temperature on the electron energy levels as well as energy transition and the oscillator strength. Then after, we investigated the impact of those parameters on the total optical absorption coefficient ($\alpha^{(Tot)}$) related to ISB transitions with respect to the incident photon energy. The obtained results have showed that, the variation of temperature and the coupling barrier have a significant impact on the optical absorption in double quantum well systems. It is also shown that, either the position or the amplitude of $\alpha^{(Tot)}$ can be shifted towards higher or lower energy range according to both coupling barrier thickness and the temperature change (see table 3.1).

TABLE 3.1: The effect of the coupling and temperature on ISB total optical absorption coefficient.

ISB TOAC	T:300K→500K		W:0.5a^*→a^*	
	position	Amplitude	Position	Amplitude
$\alpha^{(Tot)}_{2s-2p}$	Redshifted	Dropped	Blueshifted	Constant
$\alpha^{(Tot)}_{2p-3s}$	Redshifted	Dropped	Redshifted	Dropped
$\alpha^{(Tot)}_{3s-3p}$	Blueshifted	Dropped	Blueshifted	Dropped
$\alpha^{(Tot)}_{3p-3d}$	Redshifted	Dropped	blueshifted	Improved
$\alpha^{(Tot)}_{2p-3d}$	Redshifted	Improved	Redshifted	Dropped
$\alpha^{(Tot)}_{1s-3p}$	Redshifted	Improved	Redshifted	Dropped
$\alpha^{(Tot)}_{2s-3p}$	Blueshifted	Dropped	Blueshifted	Dropped
$\alpha^{(Tot)}_{1s-2p}$	Redshifted	Constant	Redshifted	Improved

Chapter 4

ISB optical absorption in PDQWs: The temperature, In-compositions, impurity and size effects

Sommaire

4.1 Introduction 69
4.2 Theoretical background 69
4.3 The effects of temperature, In-compositions, impurity and coupling . 70
4.3.1 Electron wave functions and energy levels 70
4.3.2 Electron transition energy 72
4.3.3 Dipole matrix element 72
4.4 Total optical absorption coefficient 73
4.5 Conclusion 76

4.1 Introduction

ISB optical absorption in parabolic and semi-parabolic nanostructures have attracted much interests and have been widely investigated in literature regarding its importance. Different studies have shown that the linear, third-order nonlinear and total optical absorption those systems can be affected under compositions[28], temperature[28], impurity[49] and size[47]. This chapter is devoted to investigate the influences of temperature, In-compositions, impurity and size on the electron energy levels, energy transition, the dipole matrix element and the total optical absorption coefficient (i.e., $\alpha_{1s-2p}^{(Tot)}$).First, we started to show the effect of both the coupling and impurity effects on the splitting energy between $1s$ and $2s$ electron-states and their probability densities. Secondly, we presented the theoretical framework used to perform this study and then we discussed the results obtained under the effects of the parameters mentioned above (i.e., T, x, W and λ).

4.2 Theoretical background

To be more realistic we have adopted a finite parabolic potential barrier through this study instead of an infinite one, which is the perfect and the only case that allows to induce the quantification concept. Within this chapter, we have adopted the same model and ingredients used in the previous chapter. The electron's Hamiltonian is the same used previously with the impurity presence. We only changed the potential profile to adopt a parabolic one. It is modulated analytically as follows:

$$V_c = \begin{cases} \frac{4V_0}{l^2}\left(z - L - \frac{l}{2}\right)^2, & \begin{cases} L \leqslant z \leqslant L + l \\ L + W + l \leqslant z \leqslant L + W + 2l \end{cases} \\ V_0, & \begin{cases} L + l \leqslant z \leqslant L + W + l \\ L + W + 2l \leqslant z \leqslant 2L + W + 2l \end{cases} \\ \infty, & \begin{cases} z \leqslant 0 \\ z \geqslant 2L + W + 2l \end{cases} \end{cases} \tag{4.1}$$

where $V_0 = Q\left[E_g^{GaN}(T) - E_g^{InGaN}(T)\right]$

The linear, third-order nonlinear, and total optical absorption coefficients ($\alpha^{(Tot)}$) are calculated within the framework of the compact density matrix and are given by the same expressions given before in chap.2 (2.7a, 2.7b,2.8).

4.3 The effects of temperature, In-compositions, impurity and coupling

4.3.1 Electron wave functions and energy levels

In the last chapter, changing electron probability densities, electron energy levels, and oscillator strength result in changing positions and maximum optical absorption spectra. For this reason, we will discuss below, mainly, the influence of the mentioned parameters above on the key elements that govern optical absorption spectra.

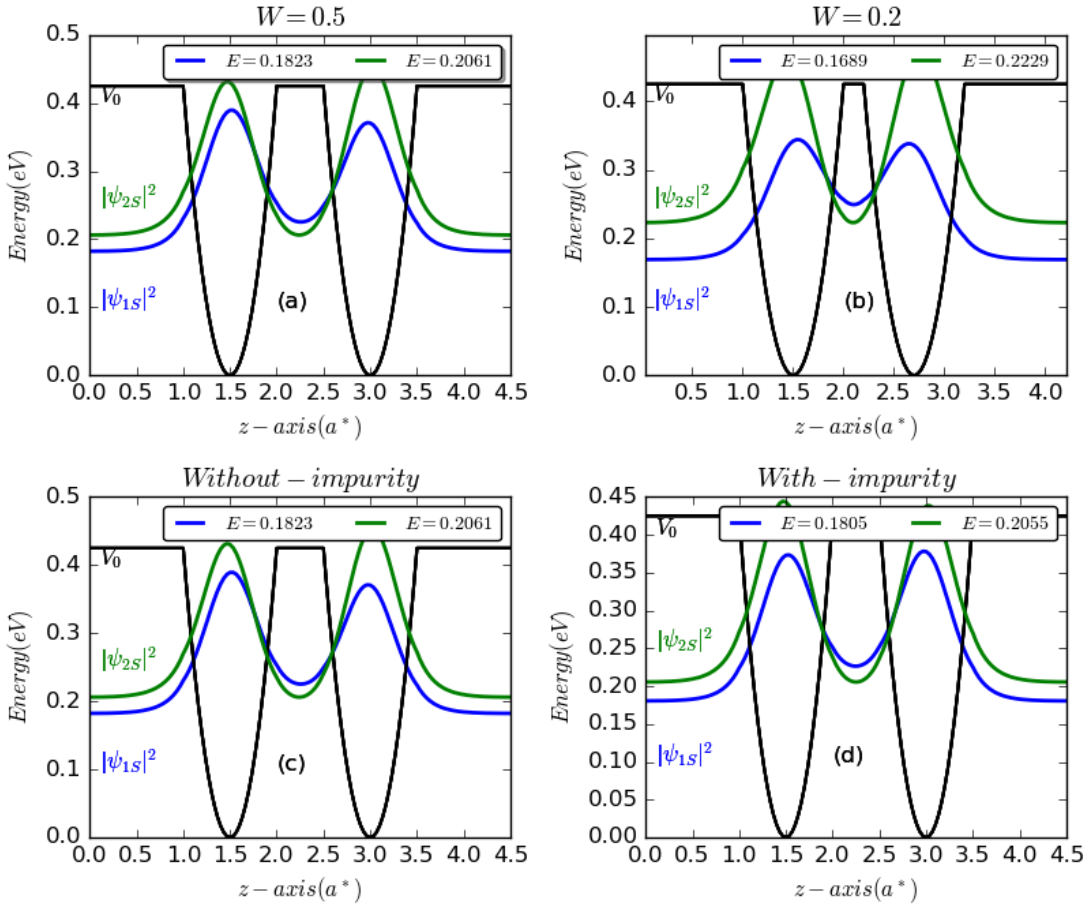


FIGURE 4.1: The electron probability densities of the ground and first excited state versus the growth direction with $x = 0.1, l = L = 1$, the coupling and impurity effects are included: Panels (a) and (b) depicted for on center impurity and panels (c) and (d) presented for W=0.5.

Fig.4.1 depicts the schematic diagram of the potential barrier as well as the ground and first-excited electron probability densities and their associated energy levels as a function of the growth direction ($z-axis$). From this figure, we can clearly see that for PDQWs consisting of two QWs separated by a thin coupling barrier layer (GaN), the tunneling phenomenon through the middle layer makes the degenerated single energy states split into the doublet corresponding to symmetric and anti-symmetric states (i.e., ψ_{1s} and ψ_{2s}, respectively). As the middle barrier thickness diminishes, the energy splitting rises by approximately 30 meV. It is also observed that all states are more localized in the well regions. Whereas, it is obvious that with inducing the impurity, the energy of splitting showed a slight increase of about 12 meV.

The variation of electron energy levels (i.e., E_{1s} and E_{2p}) versus the temperature and coupling, In-composition and the well thickness is presented in Fig.4.2.

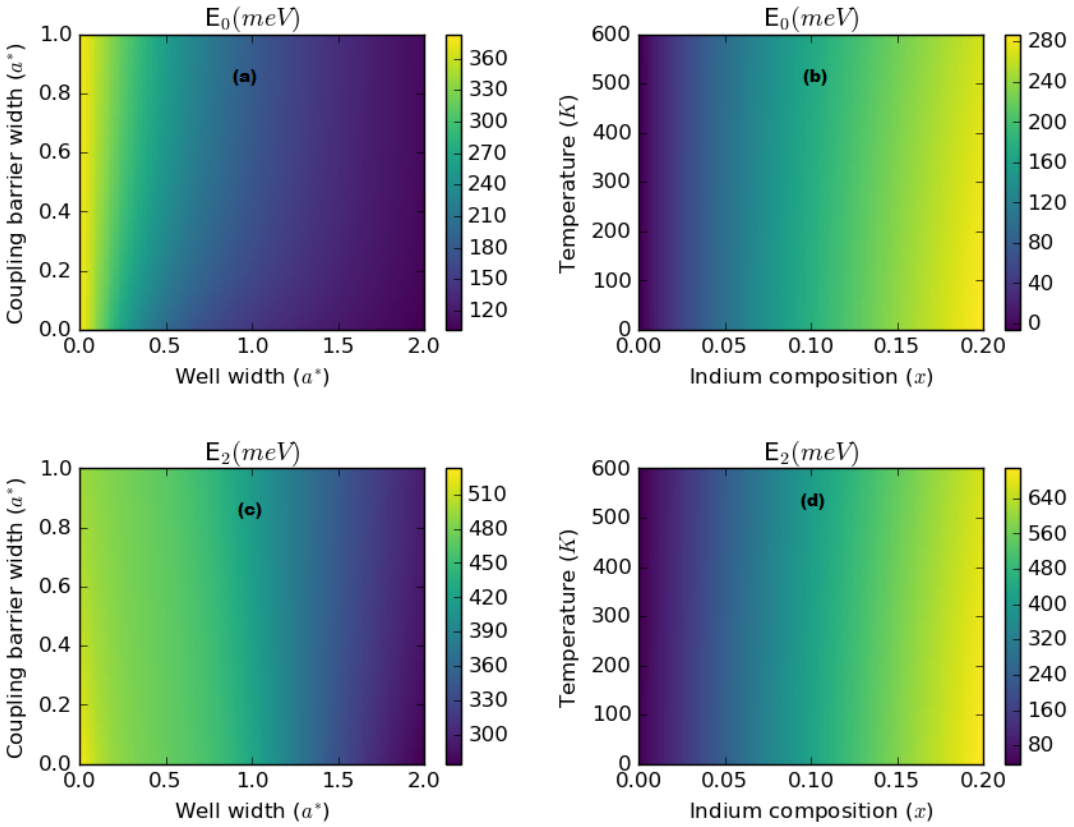


FIGURE 4.2: The variation of the energy level of the fundamental $E_0(1s-state)$ and second excited electronic-state $E_2(2p-state)$ versus temperature and well thickness in symmetric InGaN/GaN PQQWs for $x=0.1, W=0.5, L=2$ with the presence of an on-center impurity [28].

Panels (a) and (c) show the variation E_{1s} and E_{2p} with respect to the coupling and well thickness while panels (b) and (d) illustrate the variation E_{1s} and E_{2p} as a function of temperature and In-composition. It can be seen clearly from this panels that, for a fixed value of the temperature and coupling barrier, E_{1s} and E_{2p} decreased with increasing the well thickness while they rise with the increase in In-compositions. However, the variation of both temperature and the coupling barrier have almost no influence on neither E_{1s} nor E_{2p}.

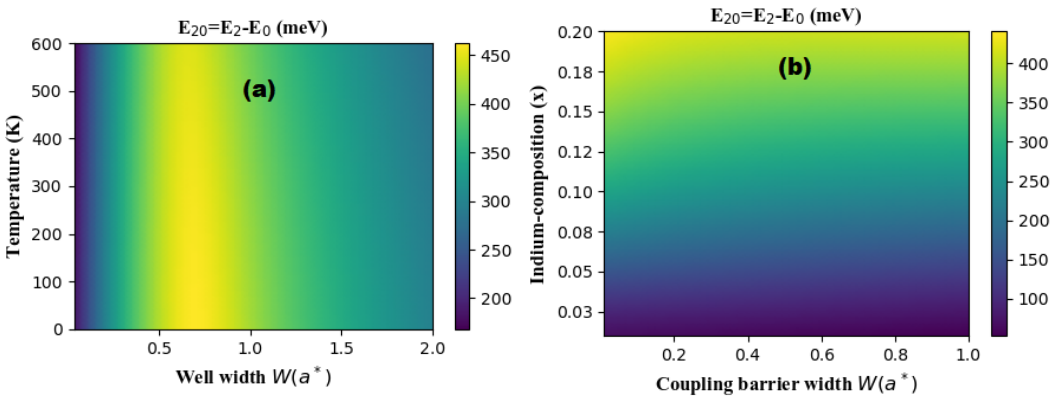
4.3.2 Electron transition energy

Fig.4.3 displays the variation of the electron transition energy (ΔE_{20}) as a function of temperature, well thickness, coupling barrier and In-compositions. Panel (a) represents the variation of ΔE_{20} as a function of temperature, well thickness while panel (b) depicts its variation as a function of coupling barrier and In-compositions. From panel (a), we can investigated two cases: strong and weak confinement regimes. For all values of temperature, with increasing the well width, ΔE_{20} rose in the strong confinement regime to reach a maximal value at a critical well thickness around 0.7 and then falls to reach a minimal value in weak confinement regime. This is due to the fact that, in weak confinement regime, the ground and the second excited states are primarily localized in the wells while in strong confinement regime, E_{2p} rises faster than E_{1s} and ΔE_{20} can only augment. However, according to panel(b), ΔE_{20} increases with increasing In-composition in the QW while the effect of the coupling barrier is almost neglected when compared with that of In-composition. This increase is due to the fact that, with the augmentation of In-concentration in InGaN, the confinement inside the QW becomes stronger and then the transition energy can only increase.

4.3.3 Dipole matrix element

Fig.4.4 shows the dipole matrix element change associated to the ground ($i = 0$) and second excited ($f = 2$) states as a function of the well thickness. Panel (a) represents the effect of the thickness of the coupling barrier on $|M_{fi}|^2$ while panel (b) shows that of the temperature.

According to both panel (a) and panel (b), the dipole matrix element increases with



(a) (b)

FIGURE 4.3: The variation of difference energy between (E_0) and (E_2) levels as a function of temperature and well thickness in symmetric InGaN/GaN DPQWs for $x = 0.1, W = 0.5, L = 2$ with the presence of an on-center impurity [28].

the increase in the QW thickness which is expected due to the increase in the interaction between the electron-states within the QW. From the same panels, it is also shown that $|M_{fi}|^2$ increases with increasing both the coupling barrier thickness and the temperature. Moreover, it is very important to mention that the effect of temperature is neglected compared to that of the coupling barrier one and that, in strong confinement regime (e.g., $l < 2$), both the coupling barrier and temperature have no influence on $|M_{fi}|^2$. Consequently, this change will have a noticeable impact on the optical absorption coefficient in the investigated system.

4.4 Total optical absorption coefficient

The investigation of linear and non-linear optical proprieties of such nanostructure requires a deep understunding of the parameters studied above (E_{20}, $|M_{fi}|^2$). So that, to present our optical properties findings, firstly we considered some of the TOAC's key qualities, which are showed previously. The resonance peak positions of the linear term is provided at $\hbar\omega = \sqrt{E_{fi}^2 + (\hbar\Gamma_{if})^2}$, and its amplitude maximum is estimated by the term $|M_{fi}|^2/\sqrt{E_{fi}^2 + (\hbar\Gamma_{if})^2}$. Given that $|M_{ff} - M_{ii}|^2/M_{fi}^2$ rate disappear quickly, leading to a minor contribution of the second term of the non-linear optical absorption coefficient given by Eq.2.7a. Then, the third nonlinear contribution reaches its maximum approximately, the same value as that of the linear one. However, the amplitude's maximum is governed by $|M_{fi}|^4/(E_{fi}^2 + (\hbar\Gamma_{if})^2)^{\frac{3}{2}}$. Assuming that $\hbar\Gamma_{if} \ll E_{fi}$ holds true

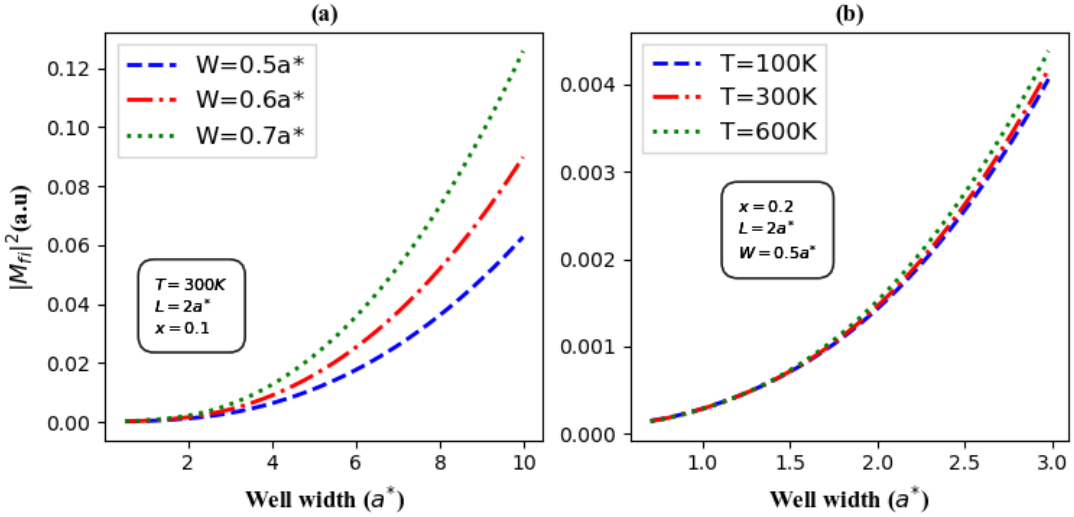


FIGURE 4.4: The variation of the square of the dipole transition element matrix between $1s$ and $2p$ as a function of the well width (a) and the indium concentration (b) in symmetric InGaN/GaN DPQWs: The effects of the coupling barrier width (a) and temperature (b) are reported. (a.u signify arbitrary unit) [28].

for all scenarios associated to Indium-composition, structure size, and temperature, total absorption should maximize around the energy difference between the bound states ($\hbar\Gamma_{if} \approx E_{fi}$). The total absorption amplitude maximum, on the other hand, is defined by two parameters that act in the opposite trend, $M_{fi}^2/E_{fi}$for linear term and M_{fi}^4/E_{fi}^3 for nonlinear one. The above-mentioned features of the optical transition energy and electric dipole matrix elements give the required data for the physical interpretation of the optical properties. Fig.4.5 presents the derived $\alpha^{(Tot)}$ data, which is an overview of how matter interacts with the electromagnetic pulse at varied coupling barrier's widths and temperature values. Panels (a) and (b) depict the modulation of $\alpha^{(Tot)}$ as a function of incident photon energy ($\hbar\omega$) in symmetric PDQWs with three different values of temperature and coupling barrier's widths (W). Here, the increment in temperature induces the $\alpha^{(Tot)}$ resonant peak position to undergo a important red-shift. This is in good agreement with that reported in Fig.4.3. In addition, with increasing temperature, it is obviously observed that the $\alpha^{(Tot)}$ amplitude maximum shown a slight change (enhancement). This can be explained by the fact that linear contribution improvement is approximately compensated by the nonlinear one. These results are in good agreement with those reported in[1].

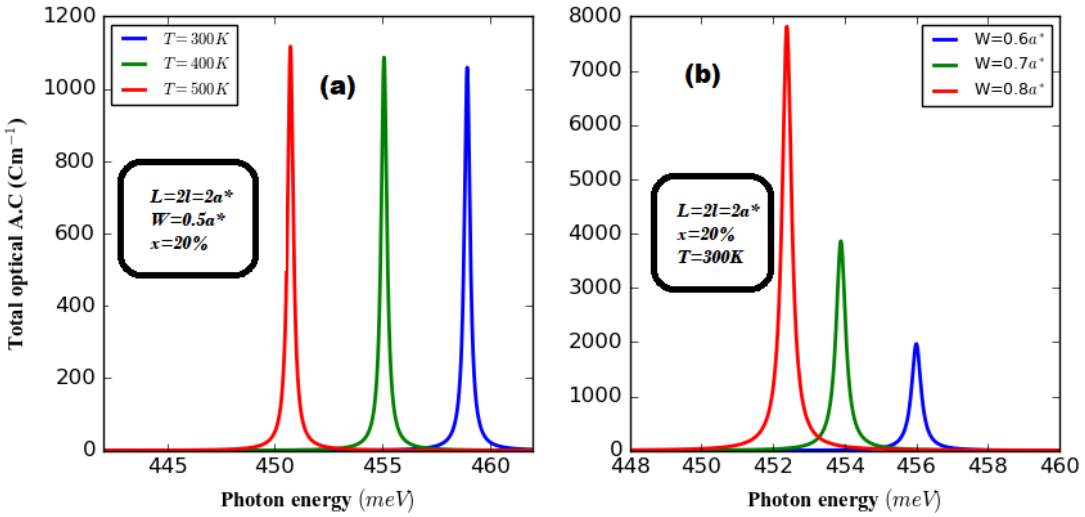


FIGURE 4.5: The variation of $\alpha^{(Tot)}$ versus incident photon energy ($\hbar\omega$) in symmetric PDQWs for $L = 2l = 2$ and $x = 20\%$: The effect of temperature is shown in panel (a) and that of coupling in panel (b) [28].

Obviously, as a consequence of the coupling barrier width increasing, the $\alpha^{(Tot)}$ resonant peak position shifts significantly toward lower energies (red-shift). Also, an noticeable nonlinear increase in the $\alpha^{(Tot)}$ maximum is revealed. For example, when the coupling barrier width changes from $0.6 \rightarrow 0.8$, the resonant peak location shifted from approximately $456 \rightarrow 452meV$, revealing a red-shift of about $4meV$, while their associate maximum increased from approximately $2000 \rightarrow 8000\ Cm^{-1}$ with an enhancement of almost 400%. The physical reasons can be found in the results presented above. In Fig.4.6, we depict the $\alpha^{(Tot)}$ change versus photon energy considering the influences of well content (x in the well) and impurity's position (λ) in the structure at room temperature in PDQWs. The major aspect of this figure is that by varying the Indium-compositions as well as impurity's location, a similar pattern is obtained. It seen that, as the well content increases, the position of $\alpha^{(Tot)}$ spectrum becomes has been shifted towards highest energies (blue-shifted). The physical reason could be linked to an increase in well composition resulting in an enhancement of the barriers height. For example, as the In-content increases from 10.1% to 10.3%, the blue-shift increased by around 5.52 meV. It is worth noting that the $\alpha^{(Tot)}$ limit yields a significant improvement according to the composition. This result is in good conformity with those reported in our previous work Ref[30]. The same figure panel (b) shows clearly that the impurity acquires a red-shifted character as it proceeds from the left band edge to the center of the structure.

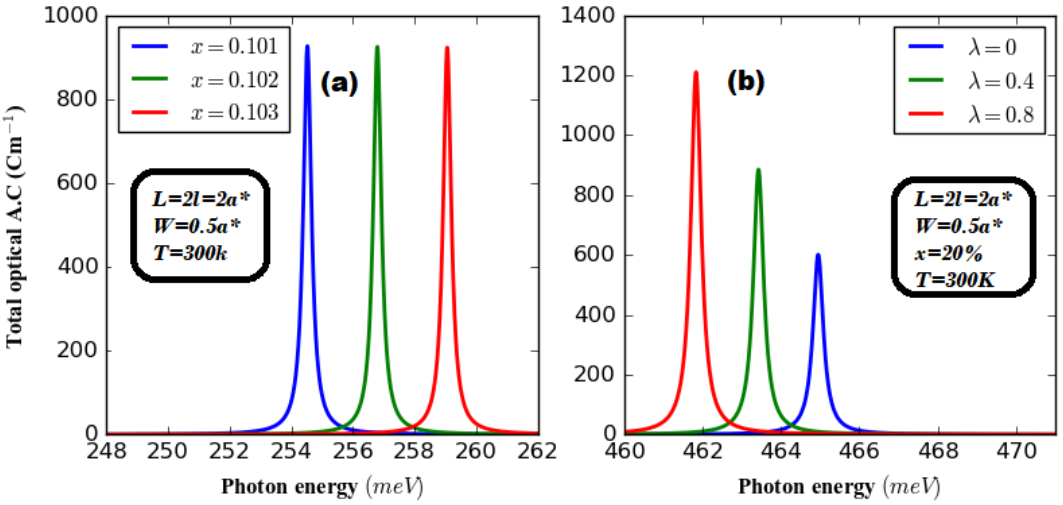


FIGURE 4.6: The variation of $\alpha^{(Tot)}$ versus incident photon energy ($\hbar\omega$) in symmetric PDQWs for $L = 2l = 4W = 2$ and $T = 300K$: The effect of In-composition is shown in panel (a) and that of impurity in panel (b) [28].

Furthermore, the closer impurity is to the center of structure, the more the positions of the resonance peak move towards low energies range. This can be explained by the fact that incrementing the linear counterpart $(|M_{fi}|^2/E_{fi})$ is more (less) pronounced than the non-linear one $(|M_{fi}|^4/E_{fi}^3)$ when the impurity is located in the left(right) edge of the left-barrier.

4.5 Conclusion

This chapter has been devoted to study the influences of temperature, In-compositions, impurity and size on the electron energy levels, energy transition, the dipole matrix element and the total optical absorption coefficient ($\alpha_{1s-2p}^{(Tot)}$).First, we started with showing the effect of both the coupling and impurity effects on the splitting energy between $1s$ and $2s$ electron-states and their associated probability densities. Secondly, we presented the theoretical framework and the theory used in our numerical calculations this study and then we discussed the results obtained under the effects of the parameters mentioned above. We shown that, the variation of the above mentioned parameters has a significant impact on the positions and the maxima of the $\alpha^{(Tot)}$'s resonance peaks. A red(blue)shifts have been obtained and a drop (improve) in the amplitude of the resonance peak have also been noticed under the change in those parameters.

Chapter 5

ISB optical absorption in DQWs: Shape, Number of QWs, Asymmetry and Electric and magnetic fields effects

Sommaire

5.1 Introduction . . . 79
5.2 Theoretical background . . . 79
5.3 Potential barrier shape effect . . . 79
5.3.1 Electron wave functions . . . 80
5.3.2 Electron transition energy . . . 80
5.3.3 ISB optical absorption coefficients . . . 81
5.4 Number of QWs per nanostructure effect . . . 82
5.4.1 Number of QWs effect on GaN-based LEDs characteristics . . . 82
5.4.2 Number of QWs per nanostructure effect on OACs . . . 84
5.5 Structure asymmetry effect on OACs . . . 87
5.5.1 Electron wave functions . . . 87
5.5.2 Electron transition energy and dipole matrix element . . . 88
5.5.3 ISB optical absorption coefficients . . . 89
5.6 Electric and magnetic field effects on OACs . . . 90
5.6.1 Electron wave functions . . . 90
5.6.2 Electric field effect . . . 91
5.6.3 Magnetic field effect . . . 93
5.7 Conclusion . . . 96

5.1 Introduction

Previous studies have shown that, electric and magnetic fields [46, 88], shape[37] and symmetry[48] have an important influence on the linear, third-nonlinear and total optical absorption related to both ISB and BTB transitions. It is also demonstrated that the number of QWs per nanostructure [17] and the shape of potential affect the optical absorption in nanostructures [5]. In the first part, we explored the theoretical background adopted after a brief introduction, then we began the discussion of our results by showing the influence of electric and magnetic fields on the OACs characteristics. In a second part, we presented the results demonstrating the impact of the potential confinement shape and the structure symmetry on the OACs including the number of QWs per nanostructure. Then we ended the chapter with a brief conclusion.

5.2 Theoretical background

The results of this chapter have been obtained using the same theoretical framework presented in previous chapters. Therefore, the electron's Hamiltonian has been given taking into account of the impurity presence. The ingredients (e.g., band-gaps, effective masses and the relative dielectric constants of GaN and InN) used in this study are the same as those used previously. This Hamiltonian has been computed within the framework of the effective mass approximation. L and l design the barrier and the well thicknesses while W represents the coupling barrier width. Finally, the analytical expressions of the linear, nonlinear and total optical absorption coefficients used to perform the calculations of this study are the same as those used in the previous chapters.

5.3 Potential barrier shape effect

It is well known that the structure's shape is one of premordial adjusting parameter playing an important role for improving the performance of optoelectronic devices. This section is carried out to show the impact of the nanostructure shape on the OAC. Thus, we consider three different nanostructures shapes to be compared in terms of optical absorption: RDQW, PDQW and TDQW.

5.3.1 Electron wave functions

Fig.5.1 depicts the schematic diagram of different DQW-nanostructures showing the electron probability densities corresponding to the ground and two lowest excited-states. To give a good picture, we have moved each wave function to be localized on its corresponding eigen-value. It is clearly seen that the structure shape has a significant influence on the electron probability densities. For RDQW, we noticed that the probability densities are more localized inside the QWs compared to that in PDQW and TDQW structures especially that corresponding to the ground-state. It is obvious that, the probability densities are more localized in the wells, especially, for RDQW compared to the others. In addition, the corresponding energy levels are greater in TDQW and PDQW compared to RDQW. For instance, the $1s(2p)$ energy levels are respectively equal to $4(14meV)$, $14(21meV)$ and , $15(21meV)$ for RDQWn PDQW and TDQW. In the same sense, it appears that the $1s$ and $2s$ splitting energy is strongly shape-dependent. This later is around of $10meV$, $6.5meV$ and $6meV$ for RDQW, PDQW and TDQW, respectively. Moreover, this quantity is much important in TDQW compared to PDQW and RDQW.

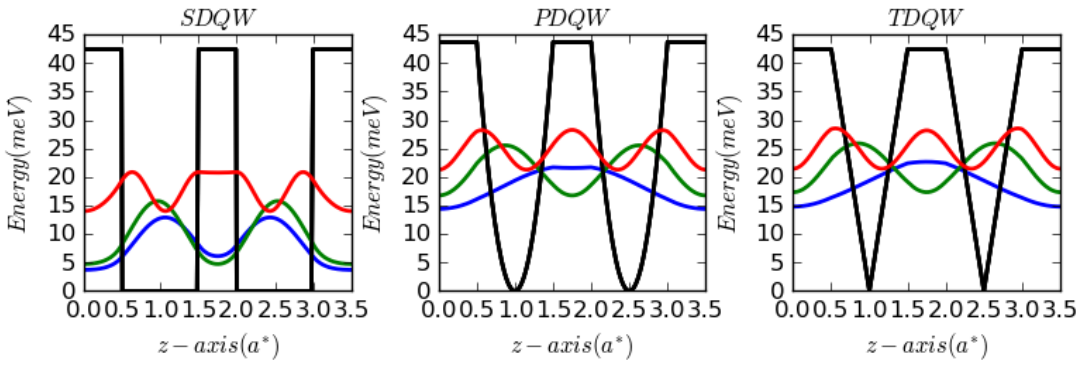


FIGURE 5.1: The potential profile, $V(z)$, and the electron probability densities of the ground and two low-laying states as a function of the growth direction ($z-axis$) for $L = 0.5, l = W = 1$ and $x = 0.2$ taking into account three different confinement profile: RDQW(left), PDQW(middle) and TDQW(right)

5.3.2 Electron transition energy

Fig.5.2 reveals the electron transition energy variation with respect to coupling barrier thickness for three different nanostructure's shapes. According to this figure, for fixed

barrier and well widths, the electron transition energy decreases with rinsing the coupling barrier regardless the structure's shape. It is noticed that this decrease is faster in

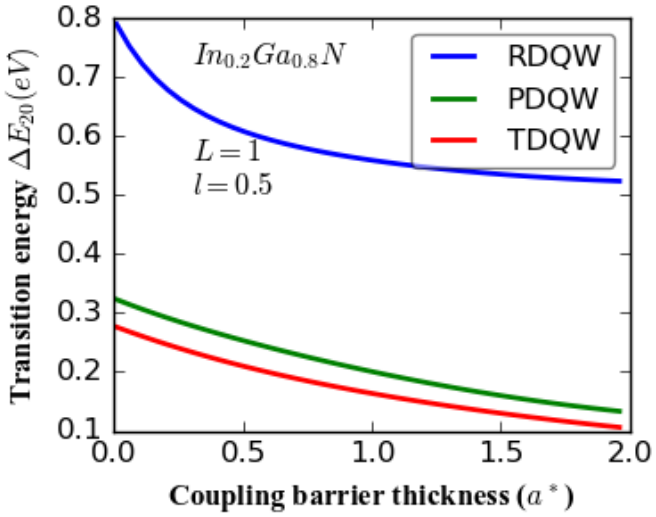


FIGURE 5.2: The variation of the transition energy between 1s-2p levels (E_{20}) as a function of coupling barrier with (W) for three different confinement profile: RDQW(blue), PDQW(green) and TDQW(red)

RDQW compared to those in PDQW and TDQW nanostructures. For example, within $0-2$ coupling barrier range, the transition energy decreasing rate is respectively about 15%, 10% and 9% for RDQW, PDQW and TDQW. In addition, for all coupling barrier values, the electron transition energy RDQW is always greater than those of PDQW and TDQW structures. Also, this quantity is the lowest in TDQW structure compared to the others. This can be explained by the fact that 1s-state is more affected than 2p-state for all shapes. Referring to RDQW, the 1s-state is more influenced in TDQW than PDQW compared 2p-state.

5.3.3 ISB optical absorption coefficients

It is well known that the OACs are strongly governed by the transition energy as well as the probability densities in such a system. Therefore, the change of those quantities has definitely an impact on the OACs profile. Fig.5.3 shows the variation of OACs with respect to the incident photon energy for three different nanostructure-shapes. For fixed structure size and chemical content, it is clearly observed that the OAC characteristics are hugely affected. Fig.5.3 illustrates that referring to RDQW, the resonant optical energy is more redshifted for TDQW compared to PDQW. This later, is about 96 meV

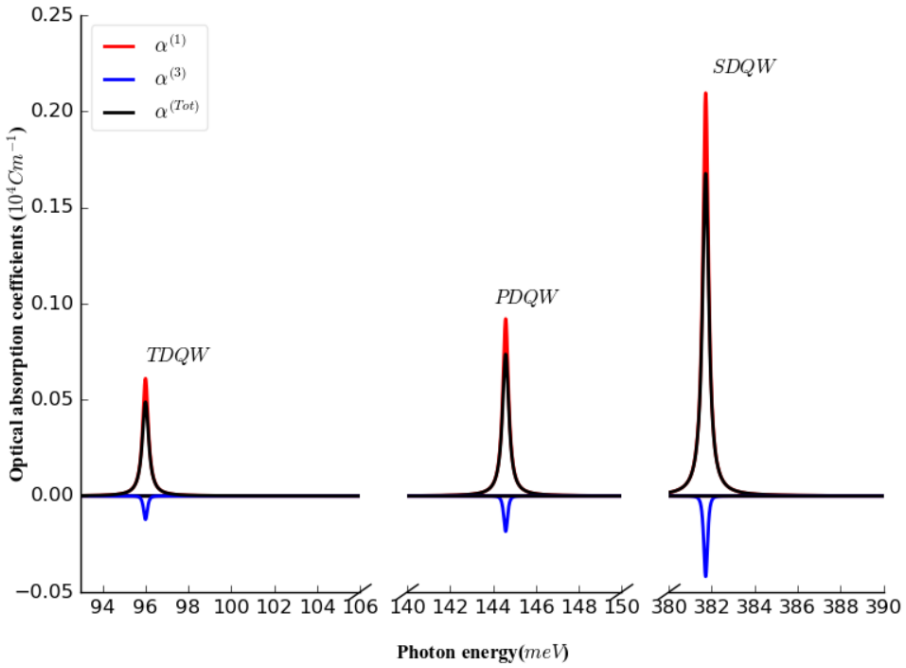


FIGURE 5.3: The variation of OACs as a function of the incident photon energy ($\hbar\omega$) taking into account the effect of the potential profile

and 144 meV for TDQW and PDQW, respectively. Moreover, the amplitude maximum is found to be more reduced in TDQW than PDQW referring to RDQW. This drop is about 60% and 50% for TDQW and PDQW, respectively compared to RDQW.

5.4 Number of QWs per nanostructure effect

5.4.1 Number of QWs effect on GaN-based LEDs characteristics

Charge carriers concentration has always been a research question for scientists in the field of materials science for a long time, until LEDs and quantum well solar cells finally appeared. The formation of quantum wells makes it possible to reduce the width of the active region of the device to a few nanometers[72]. In these systems, the charge carriers are confined more efficiently by the quantum wells and their concentrations are very high there. In GaN-based LEDs and solar cells, the alloy InGaN constitutes the quantum wells. The higher the indium composition, the lower the band-gap energy of the InGaN alloy is. The number of quantum wells has a great impact on the optical properties of a LED/ solar cell (SC). It is nearly proportional to the optical intensity of an LED and the quantum efficiency (QE) of the solar cell, as shown in Fig.5.4. At a given current intensity, we see an increase in optical intensity with the number of quantum

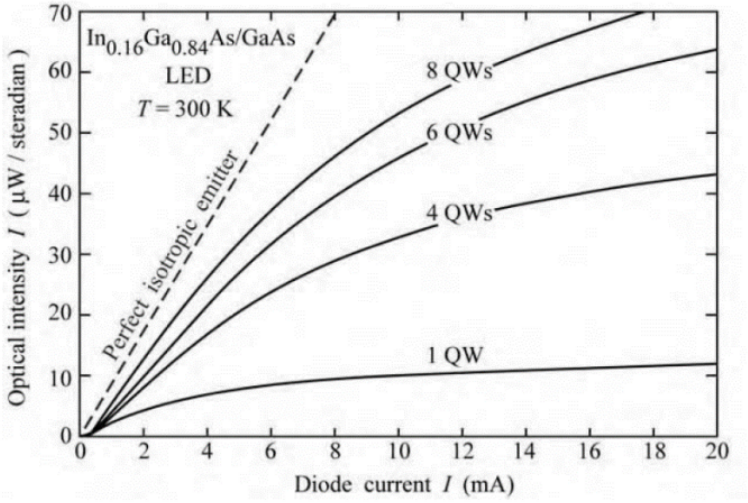


FIGURE 5.4: Example of the optical intensity of an LED in (In,Ga) depending on the intensity of the electric current and the number of quantum wells [59].

wells (QW) in GaInAs-based LEDs. Since optical intensity is a sub-linear function of current, the efficiency of (In,Ga)As LEDs drops with current like that of (In,Ga)N LEDs.

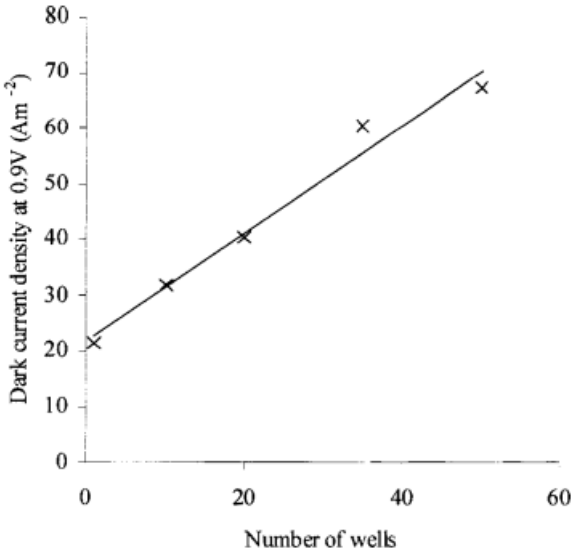


FIGURE 5.5: Dark current level at fixed bias (0.9 V) as a function of quantum well number [17].

As the number of QW increases, two competing effects are expected. First, the quantum efficiency (QE) in the spectral region covered by the QWs should rise linearly with increasing effective absorption thickness. Since absorption in a single well is generally low, this effect is should increase the short-circuit current by approximately linearly (Table5.1). However, it has been shown that there is also a significant increase

TABLE 5.1: The dependence of solar cell characteristics on the QW's number [17]

Number of QW	$V_{oc}(V)$	$J_{sc}(A/m^2)$	$FF(\%)$	$\eta_{AMO}(\%)$
1	0.963	302	85.8	18.4
10	0.976	305	84.8	18.4
20	0.952	314	83.8	18.5
35	0.959	325	81.4	18.7

in absorption at high energies in the QWs above the edge of the GaAs band where the absorption is already high and the increase is likely to be sublinear. with a good increase in the number of QW. Therefore, overall, the current enhancement might have a quite complicated dependence on the QWs number. The largest percentage increases in short-circuit current are expected in the absorption spectrum with a relatively large overlap with the QWs, as found in the optical spectrum of the GaAs-based junction of a cell in tandem. In addition to the optical effects, a larger number of wells should also increase the dark current because there will be a larger volume of low-bandgap QW material in which radiative and non-radiative recombinations can take place (Fig.5.5). Recombination in GaAsP barriers and bulk GaAs regions will be significantly lower due to their higher band gaps[17].

5.4.2 Number of QWs per nanostructure effect on OACs

It is obviously that the number of QWs per nanostructure has a significant influence on the fundamental characteristics of such devices such as the feathers of GaN-based LEDs discussed in the previous section. Indeed, without a doubt it will affect the optical absorption in nanostructures as well.

5.4.2.1 Electron wave functions

Fig.5.6 depicts the variation of both potential confinement profile and the probability densities corresponding to the ground (1s) and the two lowest-excited states (i.e., 2s and 2p) as a function of growth direction. The effect of QWs number per nanostructure (i.e., one or two QWs) is taking into account for three different nanostructure shapes. From this figure, it is clearly seen that both probability densities and the splitting energy between the allowed states have been changed by adding another QW. The probability densities became more localized symmetrically inside the QWs. However, the energy

difference between allowed states (E_{2p-1s}) decreases with adding QW for all shapes. For instance, E_{2p-1s} is approximately $4meV$, $2.5meV$ and $2meV$ for TDQW and PDQW, respectively.

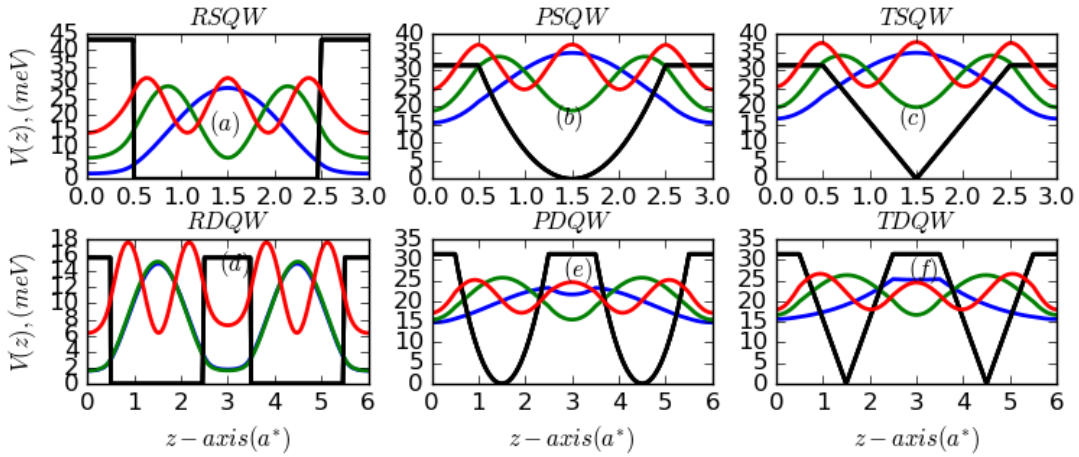


FIGURE 5.6: The schematic diagram of single and double QWs and the probability densities associated with the ground and two lowest-excited electronic states as a function of growth direction considering three different potential barrier: SQWs, panel (a, b, c) and DQWs, panels (d, e, f).

5.4.2.2 Transition energy and dipole matrix element

Panels (a) and (b) of fig.5.7 represent the variation of transition energy (E_{20}) and the square root of dipole matrix element ($|M_{20}|^2$) as a function of QW-thickness for three different nanostructure shapes, respectively. The impact of QWs number per structure is considered. Panel (a) shows that for all structures, E_{20} decreases with respect to QW width. We also notice that E_{20} is reduced by adding a QW for all the investigated structures. Moreover, for both cases, single and double QW-structures, the transition energy associated with rectangular QWs is always the greatest while that corresponding to triangular QW is the lowest for all QW thicknesses. It is also observed that this quantity diminishes faster in single QWs compared to that in double QWs for all the considered nanostructures. Our calculations show that E_{20} results are merged for thin QWs. Panel (a) shows a significant redshift which is more marked as we add another QW. This later is more pronounced for thin QW thick one. However, panel (b) shows that for all shapes, $|M_{20}|^2$ increases quasi-linearly with respect to QW width, especially in the case of single QWs. This can be explained by the fact that with the increase of QW thickness, the quantum confinement drops and then $|M_{20}|^2$ is improved. We also

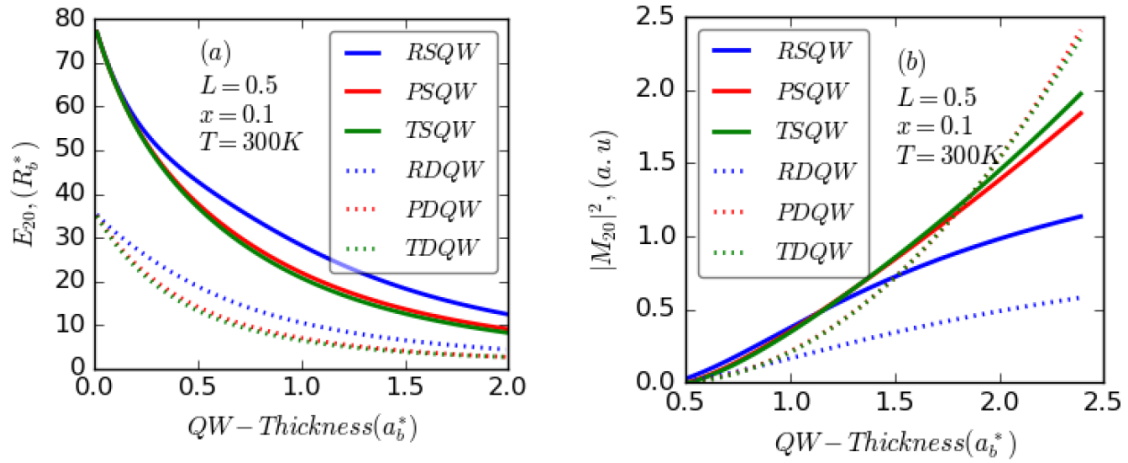


FIGURE 5.7: The variation of E_{20}, panel (a) and the $|M_{20}|^2$ in single and double QWs as a function of QW-thickness for three different nanostructures: The effect of number of QW per nanostructure is considered.

noticed that for small QWs-thicknesses, $|M_{20}|^2$ seems to be insensitive to the type of QW-shapes. Furthermore, it is almost the same in all considered systems regardless QW-width values less than $l = 1.3$. Moreover, for wide QWs, this physical parameter becomes more important in PSQW and TSQW compared to RSQW. Also, for double QWs, this quantity rose faster in large QWs. Whereas, for rectangular shape, it is always the lowest in DQWs compared to SQWs for all values of QW-width. This can be explained by the fact that the electron wave function spreads in two QWs instead of one.

5.4.2.3 ISB optical absorption coefficients

It is well known that, the linear and nonlinear optical absorption coefficients related to the ISB depend on the transition energy and the dipole matrix element. We have shown that these physical parameters vary according to the number of QW per nanostructure, which absolutely causes a variation of the optical absorption. Fig.5.8 represents the variation of the linear, third-order nonlinear and total optical absorption coefficients versus the incident photon energy for three different nanostructure shapes. The influence of QWs number is taking into account for $l = L = W = 1$ and $x = 0.2$. From this figure, it is obvious that the OACs are affected under the number of QWs per nanostructure effect. On the one hand, for all the studied systems, it is shown that with adding another QW, the resonance peaks have been moved to lower energy ranges (red-shifted) and their associated maxima have also been dropped. For instant, this

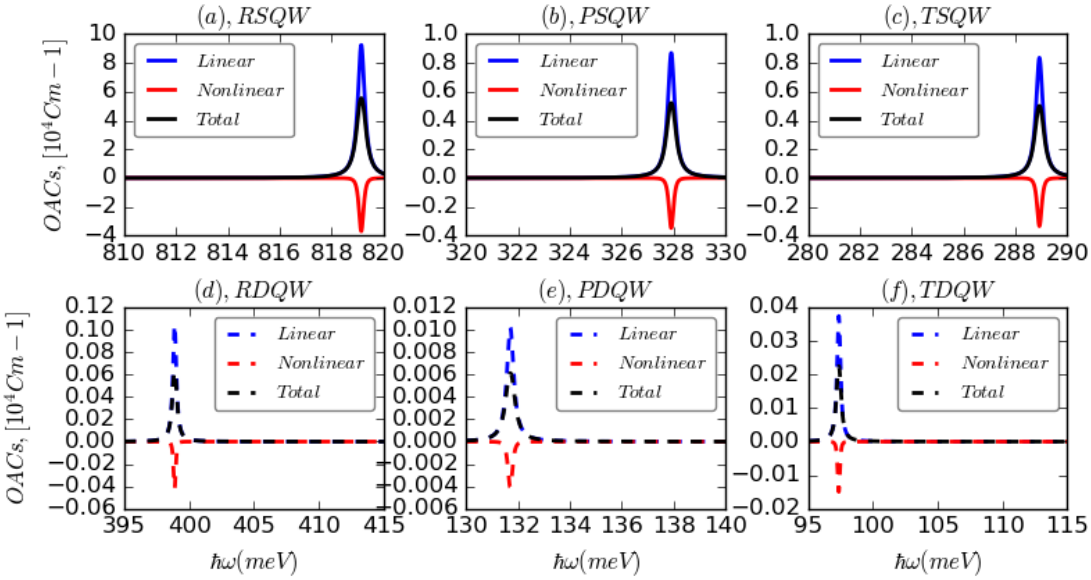


FIGURE 5.8: The variation of OACs versus the incident photon energy ($\hbar\omega$) for three different systems taking into account the effect of number of the QWs per nanostructure.

drop is approximately $421meV$, $196meV$ and $202meV$ for RDQW, PDQW and TDQW, respectively. It is also shown that the addition of another QW induces a remarkably drop of the maximum amplitudes for all shapes. This can be explained by the results presented in Fig.5.7.

5.5 Structure asymmetry effect on OACs

5.5.1 Electron wave functions

The number of QWs per nanostructure and the potential profile have a significant effect on the optical properties of nanostructures. Fig.5.9 shows the variation of confinement potential profile and the electron probability density of the ground and lowest excited-states with respect to the growth direction taking into account the asymmetry effect for three different nanostructure shapes. From this figure, for symmetric DQWs, the probability densities are localized symmetrically in the well regions for the three considered nanostructures, whereas, with reducing the size of right-QW (W), it has been seen that the electron probability densities are not much sensitive to the structures distortion, especially, PDQW and TDQW. They become more localized inside the wide wells (left QWs). This is due to the fact that, the quantum confinement is greater in narrow QW compared to that in wide one, which forces the particle to tunnel from narrow QW to

the large one through the coupling barrier. However, the splitting energy (E_{2s-1s}) is very sensitive to the structures distortion. For instance, with decreasing the right-well width from 2 to 0.5 this later is about $4.2meV$, $7meV$ and $8meV$ for RDQw, PDQW and TDQW, respectively.

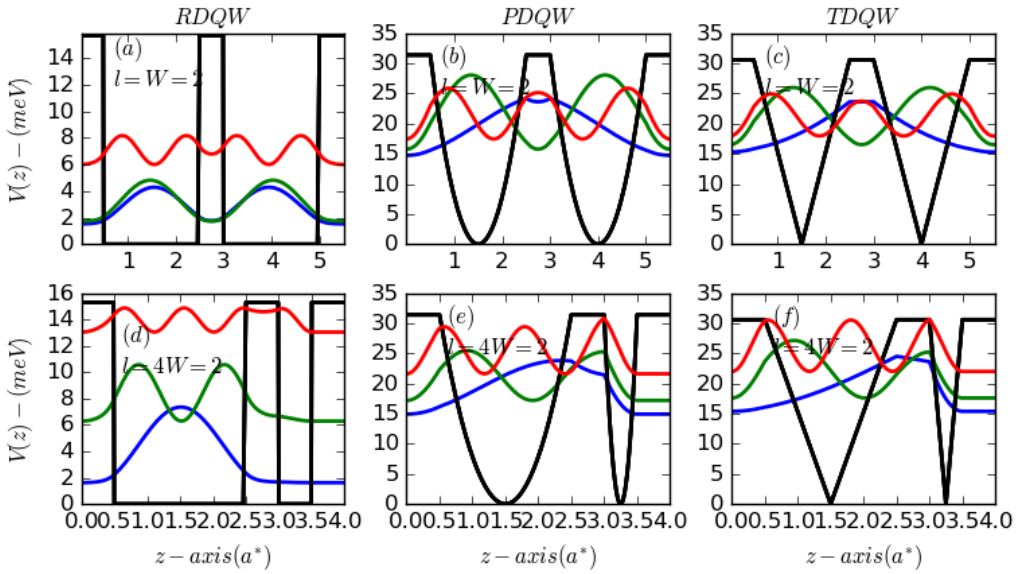


FIGURE 5.9: The schematic diagram of $V(z)$ and the probability densities of the ground ($1s$) and the two lowest excited electron states (i.e.,$2s, 2p$) as a function of the growth direction for three different nanostructure shapes: RDQW, PDQW and TDQW.

5.5.2 Electron transition energy and dipole matrix element

Fig.5.10 depicts the variation of transition energy (E_{20}), (panel (a)), and the square of transition matrix element $(|M_{20}|^2)$, (panel (b)) with respect to the right QW's thickness (W) for three different nanostructures. The principle feature of this figure, is that the transition energy and the dipole matrix element are not monotonic but present an extrimum around the effective Bohr radius. For thicknesses less than the critical width, E_{20} decreases for all considered shapes while it increases for thicknesses greater that the critical one. It is also seen that, the transition energy of RDQW is always greater than the others for all thicknesses less than the critical width while it becomes lower for thicknesses greater that the critical one. However, E_{20} corresponding to TDQW was the lowest one for thin right-well thickness and becomes the greatest for values greater that the critical thicknesses. It is obvious from panel (b) that $|M_{20}|^2$ increases to reach a maxima around critical well thickness approximately 0.8 then decreases dramatically,

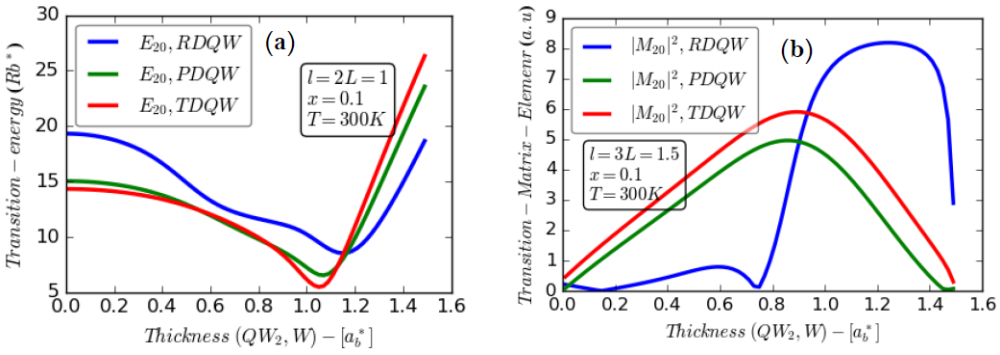


FIGURE 5.10: The variation of E_{20}, panel (a), and $|M_{20}|^2$, panel (b) with respect to the right QW's thickness (W) for three different nanostructure shapes: RDQW, PDQW and TDQW

especially for RDQW structure. Also, $|M_{20}|^2$ corresponding to this latest is always lower for all thicknesses less than the critical thickness while it is the highest for thicknesses greater than the critical width. In addition, $|M_{20}|^2$ related to TDQW shape is always greater than that of TDQW for all thicknesses. This can be explained by the fact that with reducing the right-well width, the overlapping between $1s$ and $2p$ states increases which is due to the fact that they are pushed to the left-well.

5.5.3 ISB optical absorption coefficients

Fig.5.11 depicts the variation of the linear, third-order nonlinear and total optical absorption coefficients according to incident photon energy considering the asymmetry effect for three different systems for $l = 4L = 2$ and $x = 0.1$. From this figure, it is obviously seen that the resonance peaks positions and their associated amplitudes have been changed significantly under the asymmetry of the structure for all the considered shapes. Moreover, it is seen that with increasing the right-QW's thickness, for all

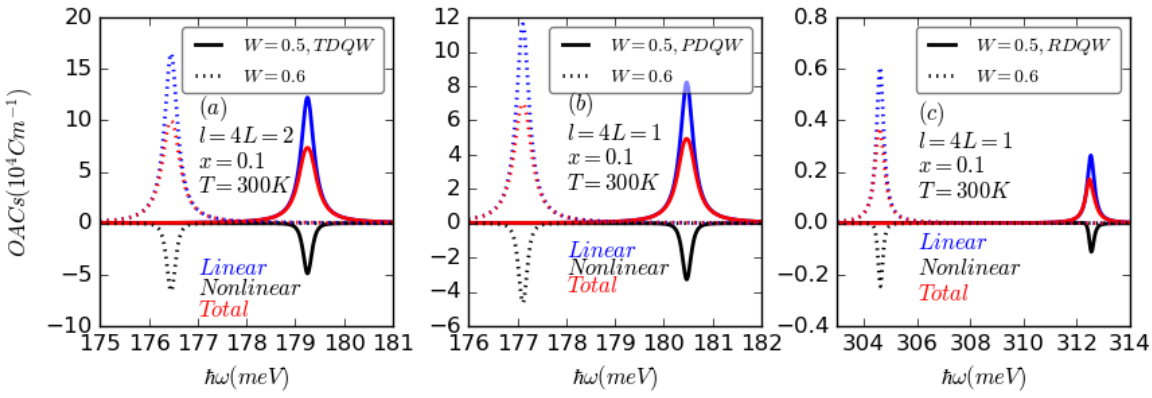


FIGURE 5.11: The variation of OACs versus the incident photon energy considering the asymmetry effect for three different nanostructure shapes: RDQW, PDQW and TDQW

shapes, the resonance peaks of the optical spectra moved towards lower energy range (redshift) while their associated amplitudes have been improved as well. Our results reveal that with increasing the right-well width, from 0.5 to 0.6, the redshift is about $3.2meV$, $3.7meV$ and $8.3meV$ for TDQW, PDQW and RDQW, respectively. However, the spectra maximum is highest in TDQW-structure compared to PDQW and RDQW structures while it is lowest in RDQW one for the same conditions. This is in good agreement with the results discussed above for concerning both E_{20} and $|M_{20}|^2$. Referring to rectangular shape, the OAC amplitude maxima are found to drop as the right-QW width is decreased.

5.6 Electric and magnetic field effects on OACs

In this section, we have adopted the same framework presented previously. The effective expressions of electric and magnetic fields intensities are given as $\mu = eFa^*/R_b^*$ and $\gamma = e^2B_z^2a^{2*}/2m^*c^2R_b^*$, respectively. F and B represent the electric field applied strength along the z-axis and that of the magnetic field applied perpendicular to the growth direction, respectively.

5.6.1 Electron wave functions

The linear and nonlinear optical absorption in single ad multiple QWs can be changed remarkably under the influence of applied electric and magnetic fields. Fig.5.12 shows the variation of confinement potential profile and the electron probability density corresponding to the ground and two lowest excited-states as a function of growth direction considering the applied electric and magnetic fields intensities effect for three different shapes (DQWs). From this figure, it can be seen that the application of external electric and magnetic fields influences both the confinement potential profile as well as the probability densities. It is noticed that without applied electric and magnetic fields (panels (a, b, c)), both the confinement potential and the probability densities show a perfect symmetry. Although, with an applied electric and magnetic fields (panels (d, e, f, g, h, i)), we noticed that neither the confinement potential profile nor the probability densities remain symmetrical. Now, without external applied magnetic

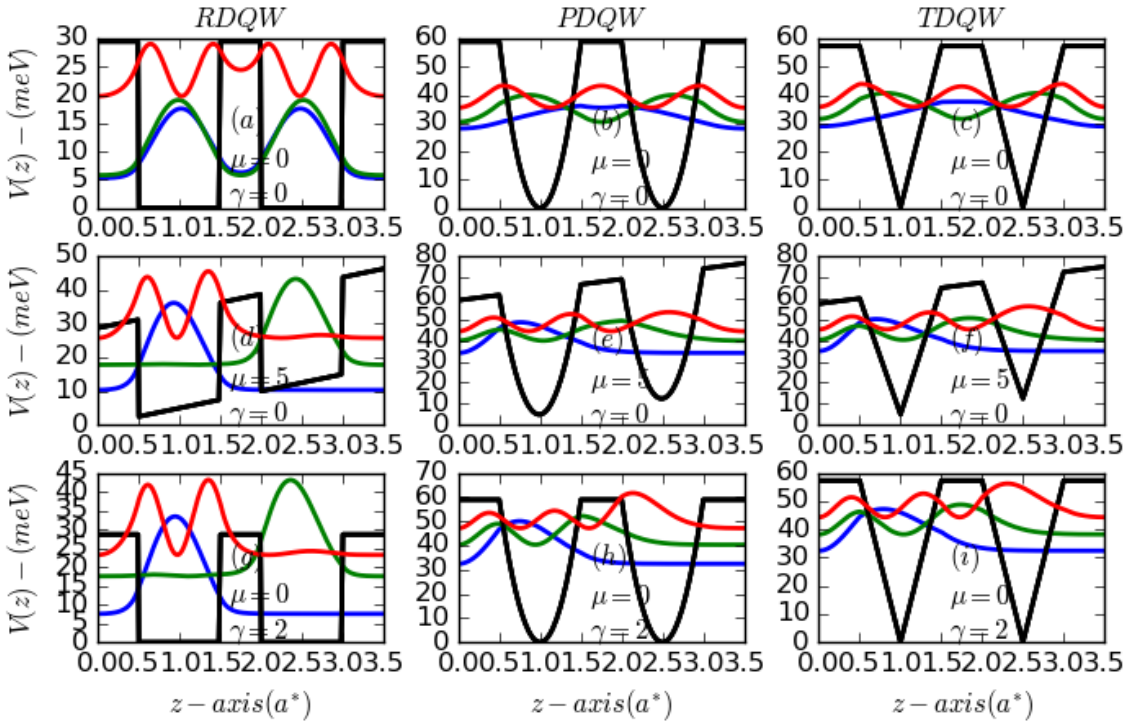


FIGURE 5.12: The schematic diagram of $V(z)$ and the probability densities of the ground ($1s$) and the lowest excited electron states (i.e.,$2s, 2p$) as a function of the growth direction considering the effects of the electric (μ) and magnetic (γ) fields for three different nanostructures: RDQW, PDQW and TDQW.

field ($\gamma = 0$) with $\mu = 5$ (panels (d, e, f)), it is shown that the all investigated structures have been misshaped and the probability densities become more localized at the left side of the structures, they moved in the opposite sense of applied electric field (along $z - axis$), which is expected. Overall, the probability density associated with the ground-state becomes more localized in the left QW well for all studied systems. It has been noticed than the QWs have distorted and the electron probability densities have been shifted towards the left side of the structures. In addition, with high applied electric and magnetic fields, the second-excited electron state ($2p$) becomes not allowed (outside the nanostructures), especially in RDQW one compared to the others.

5.6.2 Electric field effect

5.6.2.1 Electron transition energy and dipole matrix element

Fig.5.13 depicts both transition energy and dipole matrix element versus external applied electric and magnetic fields for three different systems. Panel (a) shows that

without applied magnetic field ($\gamma = 0$), it is noticed that E_{20} increases quasi-linearly for all values of the applied electric field. Moreover, for all values of the electric field, E_{20} associated with RDQW is always the highest compared to the other structures while that of TDQW-structure is the lowest. Also, for large applied electric field, E_{20} corresponding to both PDQW and TDQW becomes approximately the same. The physical reason behind this behavior is due to the $2p$state which is more affected by changing the electric field leading to E_{20} enhancement regardless all the shapes. Nevertheless,

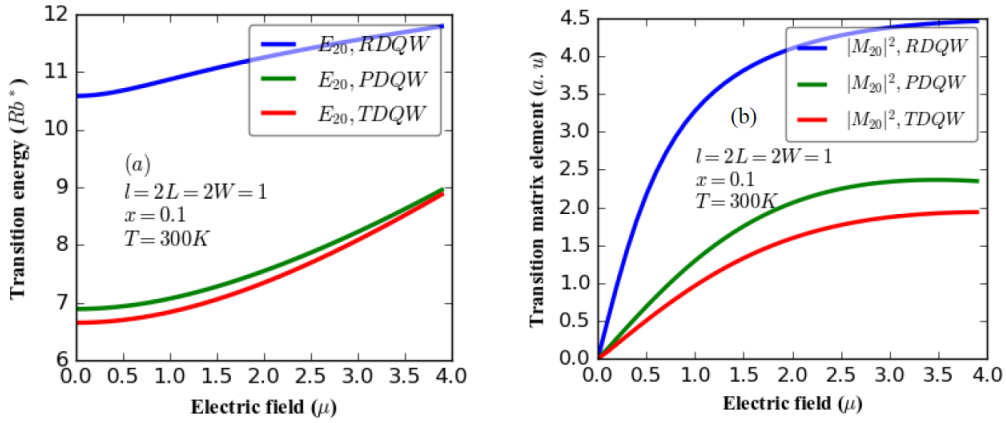


FIGURE 5.13: The variation of E_{20}, panel (a), and $|M_{20}|^2$, panel (b) according to the electric field intensity (μ) for three different nanostructures: RDQW, PDQW and TDQW

panel (b) shows that for the same above mentioned conditions, the square of dipole matrix element increases to reach a saturation regime for large applied electric field. It is also noticed that, $|M_{20}|^2$ is more sensitive to applied electric field in RDQW-structure compared to the others while that associated with TDQW is the less sensitive one.

5.6.2.2 ISB optical absorption coefficients

The key parameters that impact the optical absorption coefficients characteristics are discussed within the above subsections. Fig.5.14 represents the variation of linear, third-order nonlinear and total optical absorption coefficients as a function of incident photon energy taking into account the influence of external applied electric field (μ) for three different nanostructure shapes. It is obviously seen that with increasing the electric field intensity both the positions as well as the amplitude of the optical spectra are found to be strongly affected. Overall, it is obviously seen that the external applied electric field intensity has a significant impact on both the resonance peaks positions as well as their associated amplitudes. It is found that, for all the investigated systems, with increasing

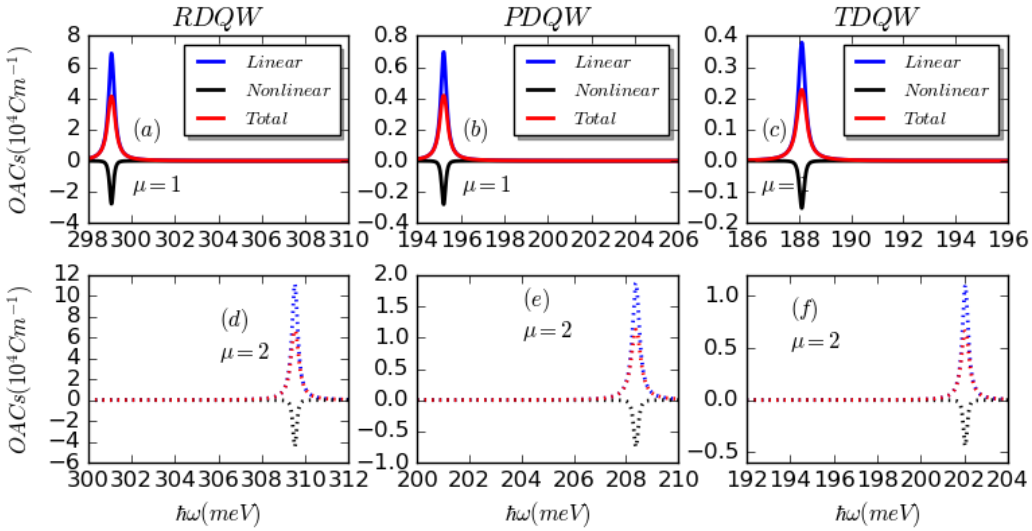


FIGURE 5.14: The variation of optical absorption coefficients versus the incident photon energy considering the electric field intensity effect (μ) for three different nanostructures: RDQW, PDQW and TDQW

the applied electric field, the resonance peaks positions has been moved towards higher energy range (blue-shoft) while their corresponding maximums showed a significant improvement. The reasons responsible for this behaviors are discussed thought the variation of E_{20} and $|M_{20}|^2$. The blue-shift is due to the improvement in the transition energy while the enhancement of the resonance peaks amplitude is interpreted by the improvement in square of the dipole matrix element for all considered systems.

5.6.3 Magnetic field effect

5.6.3.1 Electron transition energy and dipole matrix element

The variation of the transition energy and the square of the dipole matrix element with respect to the magnetic field intensity (γ) with $\mu = 0$ for three different shapes are depicted on panels (a) and (b) of Fig.5.15, respectively. It is obvious that for all values of applied magnetic field intensity, E_{20} increases quasi-linearly. Our results reveal that E_{20} tends to the same enhancement behavior for high values of magnetic field. This can be understood by the fact that with increasing the magnetic field intensity, the wave functions are forced to delocalized in the well center for all shapes. Moreover, we have observed that E_{20} associated with RDQW structure is always greater than the others for all magnetic field intensity, whereas, that of TDQW is the lowest one, especially for small values of magnetic field intensities. This is due to the increase of the magnetic

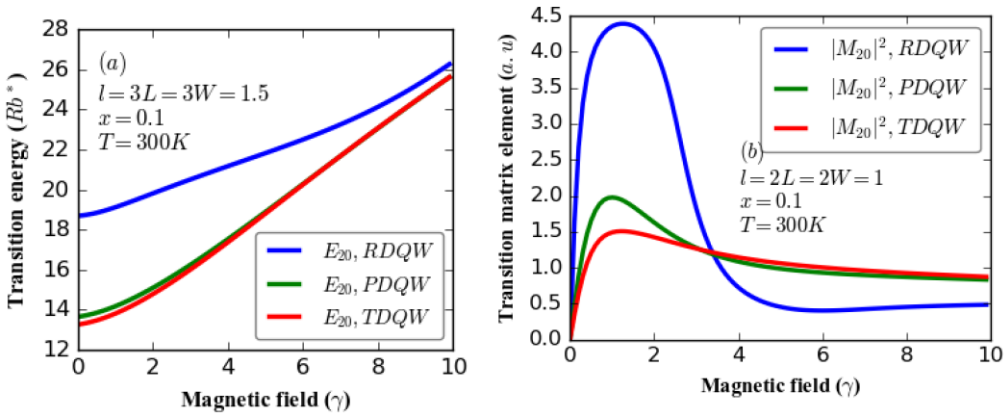


FIGURE 5.15: The variation of E_{20}, panel (a), and $|M_{20}|^2$, panel (b) according to the magnetic field intensity (γ) for three different nanostructures: RDQW, PDQW and TDQW

quantum confinement with increasing the magnetic field intensity in all types of the investigated nanostructures. Panel (b) shows that the dipole matrix element increases to reach a maxima around a critical magnetic field intensity ($\gamma \approx 1$) and then decreases to reach saturation regime for large intensities. It is also noticed that $|M_{20}|^2$ has two different behaviors. For small intensities lower than $\gamma = 4$, $|M_{20}|^2$ associated with RDQW-structure is always greater compared to the others and that of TDQW is the lowest one. For intensities greater than $\gamma = 4$, this behavior has been inverted.

5.6.3.2 ISB optical absorption coefficients

The linear and nonlinear optical absorption coefficients are strongly related to the transition energy as well as the dipole matrix element. The influence of magnetic field intensity on these parameters will definitely affects the OCAs. Fig.5.16 depicts the variation of the linear, third-order nonlinear, total optical absorption coefficients versus the incident photon energy taking into account the influence of magnetic field intensity (γ) for three different nanostructures. It is obviously seen that the increase of the magnetic field intensity influences both the positions as well as the amplitude of the optical spectra. It is found that with increasing the magnetic field intensity, the resonance peaks of the optical spectra have been moved towards higher energy range (blueshift) and their associated maximums have showed an important improvement for all studied systems. For example, for a fixed nanostructure with $\gamma = 1$, the transition energy is obtained to be around $323meV$, $243meV$ and $240meV$ for RDQW, PDQW and TDQW structures, respectively. For example, as the magnetic field intensity increases from 1 to 2, the

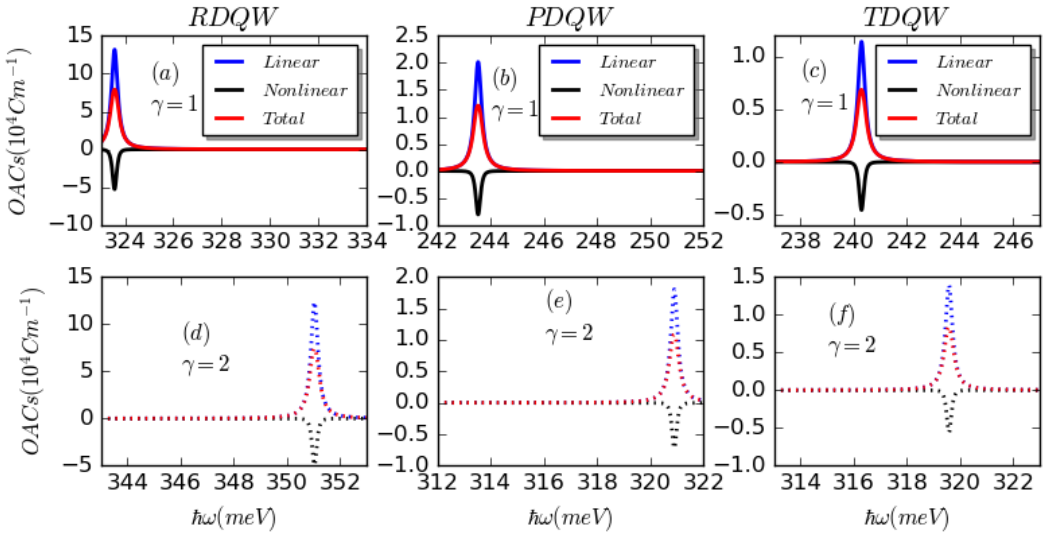


FIGURE 5.16: The variation of optical absorption coefficients versus the incident photon energy considering the magnetic field intensity effect (γ) for three different nanostructures: RDQW, PDQW and TDQW

blueshift is about $30meV$, $78meV$ and $79meV$ for RDQW, PDQW and TDQW structures, respectively. The reasons behind these behaviors are the same discussed above concerning the transition energy as well as the dipole matrix element depend on the applied magnetic field intensity.

Through this chapter, we deeply discussed and compared the OACs variation in different nanostructure shapes. We observed that the positions of the resonance peaks of OACs and their associated amplitudes were strongly affected by the structure-shape. An improvement and a drop in the optical spectra were observed associated with a noticeable red/blue shifts whatever the shape. The applied external electric and magnetic field have also remarkably affected those features. The deformation of the structure has redshifted the OACs with an important enhancement of their associated maxima. Moreover, the applied electric and magnetic fields have blueshifted the OCAs with a slight improve in their related maxima. According to this study, for a fixed structure, e.g., $l = 2L = 1$ and $x = 10\%$, we claim that the optimal nanostructure that offers the highest absorption rate is the rectangular double QWs (RDQW) one followed by parabolic (RDQW) and then triangular (TDQW) shapes, respectively. However, we have obtained that by referring to the inverted single parabolic QW (IPQW), the OACs were enhanced and its resonance peak positions were blue-shifted in ITQW. Although, it is noticed that OAC can be adjusted by varying one of the wells size and/or the external

applied electric and magnetic fields. It is observed that with reducing the righ-QW's size, the OAC rate has been improved for thick QWs while it is reduced for thin QW for all shapes.

5.7 Conclusion

This chapter has been devoted to the study of QW's number per structure, the structure asymmetry, shape (i.e., RDQW, PDQW and IPQW) and applied electric and magnetic fields effects on OACs. First, we explored the theoretical background adopted after a brief introduction, then we started the discussion of our results by showing the influence of electric and magnetic fields on the characteristics of OACs. Secondly, we discussed the results that show the impact of those parameters on the OACs. Our results suggest that all the above discussed parameters have a considerable influence on OACs. Finally, we end this chapter with a brief conclusion showing the optimal nanostructure for higher optical absorption rate.

Conclusion and perspectives

This thesis has reported a theoretical simulations of the optical and electrical properties of InGaN/GaN multiple-quantum-wells (MQWs) for photovoltaic and optoelectronic applications. All systems were studied taking into account the wurtzite crystal structure of GaN. A finite potential barrier at the interfaces between the QWs (InGaN) and the barriers (GaN) was considered in all cases. The one-dimensional Schrodinger equation in stationary regime was computed within the framework of the effective-mass approximation and the theory of envelope function numerically using the finite element method (FEM). The maximum In-composition in the well regions (InGaN) used in this study was less than 50%.

The main objective of this work was to study single and multiple InGaN/GaN quantum wells and to understand the influence of different confinement profiles and stress parameters such as temperature, In-compositions and electric field on the coefficients linear and non-linear optical absorption which affect device performance (solar cells, LEDs, Photodetectors, ...). The main results presented in this manuscript have been compared with previous work carried out over the last ten years and have shown good agreement with the literature.

In the first part of this thesis, we examined the influence of a donor impurity in a single QW InGaN/GaN taking into account the effects of the barrier/well thickness on the optical transitions band-to-band (CB-VB) and subband (ISB) related to the total optical absorption coefficient in this system. The detailed results obtained showed that the variation of these parameters has a remarkable impact on the optical properties of the studied system. The results obtained demonstrated that the optical absorption can be improved by choosing an optimized structure and adjusting the position of the impurity inside the QW as well as the In-composition in it, especially for a low indium content in InGaN for a fixed electronic density at room temperature. For the case of CB-VB transitions, although the inter-band transition energy showed a shift around 10

meV which is masked by the band-gap energy because it is the essential parameter responsible for the inter-band recombination. The maximum of the absorption spectra remains constant around the photon energy of about 2.67eV for all structure sizes. The only effect is that the amplitude of the resonance peak reaches approximately $4.10^4 cm^{-1}$ at room temperature and for a fixed barrier and well widths of 8nm(4nm), respectively. Whereas, in the case of ISB transitions, the resonance peaks have been shifted toward a higher (lower) energy range with the increase (decrease) of well (barrier) thickness, and their associated amplitudes have improved (dropped) as well. Moreover, increasing the In composition up to 50% induces a blue shift of the resonance peaks for the CB-CV and ISB optical transitions and induces an enhancement of their corresponding maxima which reaches approximately 25%[30].

The second part of this work was devoted to the study of the influence of the temperature, the coupling and the intensity of the electric field on ISB optical transitions within the conduction band related to the total optical absorption coefficient in the double quantum wells (DQW) InGaN/GaN taking into account a finite parabolic (rectangular) confinement potential. The obtained results showed that different parameters can affect the optical properties of such a studied system. For example, the increase in temperature induced a redshift in the optical spectra by about 5 meV while enhancing their associated maxima due to the increase in dielectric constant and decrease in the effective mass of electrons. Moreover, increasing the coupling parameter (the inner barrier between the QWs) led to an isolated system, which induced a blue-shift of the optical spectrum by approximately 4 meV and its associated maxima were improved by about 75%[28]. Besides, the increase of the external applied electric field has a significant impact on the optical properties of MQWs systems. The changes in the intensity of the electric field or the angle have also a remarkable influence on the position as well as on the maxima of the resonance peaks. With increasing electric field intensity, a slight decrease in resonance peak amplitudes (by about 6%) was noticed while their associated positions were blue-shifted (by about 3 meV) . The latter (TOAC) can also be affected by the change of position in the composition or impurities[31]. Moreover, the modeling confinement potential also has a noticeable influence on linear and nonlinear optical properties due to the change in the confinement strength. For example, changing the confinement potential from a parabolic to a triangular profile led to an improvement

in the maxima of the linear and nonlinear optical absorption coefficients (by about 5%) and also shifted them to a higher energy range (by about 3 meV)[27]. For now, it is clear that the optical properties can be changed under the change of all the parameters mentioned before, therefore, the efficiency and performance of the device will certainly be affected as well. it should also be mentioned that the indium content in InGaN alloys must be taken into consideration because for a rate greater than 20% of In in InGaN, it becomes difficult to obtain a good quality InGaN/GaN MQWs. Also, we couldn't get the allowed energy levels in dual QWs systems, so that, sometimes, we had to not exceed 10% of In-content to get up to five implied energy levels (conduction-ISB) with an optimized barriers/wells thicknesses[29] because for content higher than that, it start causing defect formation and quality degradation of the active region (QWs-system).

To conclude, the best structure for the device (solar cell, LED, ...) should include an optimized QW system to prevent the stress relaxation that appears in QWs thicker than a few nm from significantly altering the value of Voc (and also the conversion efficiency). Barriers should also be optimized to allow carrier tunneling as an additional mechanism to enhance charge carrier collection. Increasing in-composition is, of course, the most effective way to improve the performance of solar cells through better light absorption.

There are different ways to avoid loss of absorption efficiency due to a very thick active region and to maintain good absorption. One of them is to change the ratio between the thicknesses of barrier and wells to thicker QWs. This strategy is not always good because it leads to many born defects serving as recombination centers for carriers decreasing the value of V_{oc}. Deepening energy levels prevents carrier escape from QWs, which damages the external quantum efficiency (EQE) of devices. Therefore, increasing the QW thickness is not usually an effective way for device optimization. In 2015, Anna Mukhtarova has demonstrated that by decreasing the growth temperature and increasing the indium flux, they were able to incorporate 18% indium while preserving the good quality of the samples. The increase in the In content induces composition fluctuations in the quantum wells. Despite this and owning to better absorption, the value of J_{sc} has been significantly improved, reaching more than 2 mA/cm^2 for certain devices[61]. However, improving the performance of the device (solar cell) by about 2% requires an MQWs system that contains more than 16×QWs with an In content

in InGaN of about 18% while one can achieve an improvement of up to 2.95% with a 12×QWs system for an In ratio of around 35% [21]. The use of a less defective GaN template can also improves the performance of InGaN based devices, but increases the price as well.

It is true that InGaN/GaN can replace or be a complement to either GaAs or silicon based devices (solar cells, LEDs, Lasers, ...)[78]. Nevertheless, it still a huge work to do in order to make InGaN a great candidate to replace GaAs/Si-based devices. GaN/AlGaN nanostructures are promising for the development of ISB optoelectronic components that can cover the entire infrared range, eventually, inter-subband transitions (ISB) are energy transitions between electronic states in a quantum well. One more perspective for this work can be an extension of the present results on inter-subband transitions (ISB) for GaN components operating in the 5-10 THz band, which is forbidden for GaAs technologies[54]. Moreover, it is possible to use the results realized to study the optical absorption to investigate the characteristics and features (i.e., I(V), V_{oc}, J_{sc}, fill factor:FF and the external quantum efficiency: EQE) of InGaN-based LEDs and solar cells.

Bibliography

[1] V Akimov, DA Firsov, CA Duque, V Tulupenko, RM Balagula, M Ya Vinnichenko, and LE Vorobjev, "Temperature shift of intraband absorption peak in tunnel-coupled QW structure", *Optical Materials* 66 (2017), pp. 160–165. URL: https://doi.org/10.1016/j.optmat.2017.01.050.

[2] Hiroshi Amano, N Sawaki, I Akasaki, and Y Toyoda, "Metalorganic vapor phase epitaxial growth of a high quality GaN film using an AlN buffer layer", *Applied Physics Letters* 48.5 (1986), pp. 353–355. DOI: https://doi.org/10.1063/1.96549.

[3] Macho Anani, Hamza Abid, Zouaoui Chama, Christian Mathieu, Adlane Sayede, and B Khelifa, "InxGa1- xN refractive index calculations", *Microelectronics Journal* 38.2 (2007), pp. 262–266. URL: https://doi.org/10.1016/j.mejo.2006.11.001.

[4] Website Archieve, *Data base of relevant proprieties of semiconductor materials*. Last access:07/09/2021. URL: http://thepoussin.free.fr/TPE2003/TPE.htm.

[5] HS Aydinoglu, SERPİL Sakiroglu, HÜSEYİN Sari, FATİH Ungan, and I Sökmen, "Nonlinear optical properties of asymmetric double-graded quantum wells", *Philosophical Magazine* 98.23 (2018), pp. 2151–2163. URL: https://doi.org/10.1080/14786435.2018.1476785.

[6] Tewfik Baghdadli, "Etude des propriétés structurales et électroniques de nouveaux matériaux à base d'alliages III-N pour l'optoélectronique". PhD thesis. Université Paul Verlaine-Metz, 2009. URL: https://hal.univ-lorraine.fr/tel-01752638.

[7] G_ Bastard, "Superlattice band structure in the envelope-function approximation", *Physical Review B* 24.10 (1981), p. 5693. URL: https://doi.org/10.1103/PhysRevB.24.5693.

[8] G_ Bastard, "Superlattice band structure in the envelope-function approximation", *Physical Review B* 24.10 (1981), p. 5693. URL: https://doi.org/10.1103/PhysRevB.24.5693.

[9] Gerard Bastard, "Theoretical investigations of superlattice band structure in the envelope-function approximation", *Physical Review B* 25.12 (1982), p. 7584. URL: https://doi.org/10.1103/PhysRevB.25.7584.

[10] Nawal BENYAHYA et al., "Caractérisation et simulation des transistors HEMTs de la filière InAlN/GaN". PhD thesis. 2017. URL: http://hdl.handle.net/123456789/2100.

[11] Fabio Bernardini, Vincenzo Fiorentini, and David Vanderbilt, "Spontaneous polarization and piezoelectric constants of III-V nitrides", *Physical Review B* 56.16 (1997), R10024. URL: https://doi.org/10.1103/PhysRevB.56.R10024.

[12] Ashraful Ghani Bhuiyan, Kenichi Sugita, Akihiro Hashimoto, and Akio Yamamoto, "InGaN solar cells: present state of the art and important challenges", *IEEE Journal of photovoltaics* 2.3 (2012), pp. 276–293. DOI: 10.1109/JPHOTOV.2012.2193384.

[13] Pierre Bigenwald, Bernard Gil, F Benharrats, K Zitouni, and A Kadri, *Semiconductor Science and Technology* 27.2 (2012), p. 024009. URL: https://doi.org/10.1088/0268-1242/27/2/024009.

[14] Z Bougrioua et al., "Reduction of stacking faults in (11 -2 0) and (11 -2 2) GaN films by ELO techniques and benefit on GaN wells emission", *physica status solidi (a)* 204.1 (2007), pp. 282–289. URL: https://doi.org/10.1002/pssa.200673585.

[15] Tarik Bouragba, "Propriétés optiques de puits quantiques GaInAsN/GaAs". PhD thesis. Université Blaise Pascal-Clermont-Ferrand II, 2006. URL: https://tel.archives-ouvertes.fr/tel-00688818.

[16] MG Burt, "The justification for applying the effective-mass approximation to microstructures", *Journal of Physics: Condensed Matter* 4.32 (1992), p. 6651. URL: https://doi.org/10.1088/0953-8984/4/32/003.

[17] DB Bushnell et al., "Effect of well number on the performance of quantum-well solar cells", *Journal of applied physics* 97.12 (2005), p. 124908. URL: https://doi.org/10.1063/1.1946908.

[18] Fei Chen, Xiaohong Ji, and Shu Ping Lau, "Recent progress in group III-nitride nanostructures: From materials to applications", *Materials Science and Engineering: R: Reports* 142 (2020), p. 100578. URL: https://doi.org/10.1016/j.mser.2020.100578.

[19] L Chenini, A Aissat, and JP Vilcot, "Optimization of inter-subband absorption of InGaAsSb/GaAs quantum wells structure", *Superlattices and Microstructures* 129 (2019), pp. 115–123. URL: https://doi.org/10.1016/j.spmi.2019.03.015.

[20] Armin Dadgar et al., "MOVPE growth of GaN on Si (1 1 1) substrates", *Journal of Crystal Growth* 248 (2003), pp. 556–562. URL: https://doi.org/10.1016/S0022-0248(02)01894-8.

[21] R Dahal, J Li, K Aryal, JY Lin, and HX Jiang, "InGaN/GaN multiple quantum well concentrator solar cells", *Applied Physics Letters* 97.7 (2010), p. 073115. DOI: https://doi.org/10.1063/1.3481424.

[22] Hassen Dakhlaoui, "Linear and nonlinear optical absorption coefficients and refractive index changes in GaN/AlxGa (1- x) N double quantum wells operating at 1.55 μ m", *Journal of Applied Physics* 117.13 (2015), p. 135705. URL: https://doi.org/10.1063/1.4916752.

[23] V Yu Davydov et al., "Absorption and emission of hexagonal InN. Evidence of narrow fundamental band gap", *physica status solidi (b)* 229.3 (2002), r1–r3. DOI: https://doi.org/10.1002/1521-3951(200202)229.

[24] Haddou El Ghazi, Anouar Jorio, and Izeddine Zorkani, "Linear and nonlinear intra-conduction band optical absorption in (In, Ga) N/GaN spherical QD under hydrostatic pressure", *Optics Communications* 331 (2014), pp. 73–76. URL: https://doi.org/10.1016/j.optcom.2014.05.055.

[25] Haddou El Ghazi, Anouar Jorio, and Izeddine Zorkani, "Linear and nonlinear intra-conduction band optical absorption in (In, Ga) N/GaN spherical QD under

hydrostatic pressure", *Optics Communications* 331 (2014), pp. 73–76. URL: https://doi.org/10.1016/j.optcom.2014.05.055.

[26] Haddou El Ghazi and A John Peter, "Built-in electric field effect on optical absorption spectra of strained (In, Ga) N–GaN nanostructures", *Physica B: Condensed Matter* 470 (2015), pp. 64–68. URL: https://doi.org/10.1016/j.physb.2015.04.028.

[27] Redouane En-nadir, Haddou El Ghazi, Walid Belaid, Hassan Abboudi, Fath allah Jabouti, Anouar Jorio, and Izeddine Zorkani, "The Confinement Profile Effect on the Optical Properties in Different Inverse-shaped Single InGaN/GaN Quantum Wells", *Iraqi Journal of Physics* 20.1 (2022), pp. 1–13. DOI: https://doi.org/10.30723/ijp.v20i1.965.

[28] Redouane En-nadir, Haddou El Ghazi, Walid Belaid, Anouar Jorio, and Izeddine Zorkani, "Intraconduction band-related optical absorption in coupled (In, Ga) N/GaN double parabolic quantum wells under temperature, coupling and composition effects", *Results in Optics* (2021), p. 100154. URL: https://doi.org/10.1016/j.rio.2021.100154.

[29] Redouane En-nadir, Haddou El Ghazi, Walid Belaid, Anouar Jorio, Izeddine Zorkani, and Hamdi Şükür Kiliç, "Ground and first five low-lying excited states related optical absorption in In. 1Ga. 9N/GaN double quantum wells: Temperature and coupling impacts", *Solid State Communications* (2021), p. 114464. URL: https://doi.org/10.1016/j.ssc.2021.114464.

[30] Redouane En-nadir, Haddou El Ghazi, Anouar Jorio, and Izeddine Zorkani, "Inter and intra band impurity-related absorption in (In, Ga) N/GaN QW under composition, size and impurity effects", 330 (2020), p. 01017. URL: 10.1051/matecconf/202033001017.

[31] Redouane En-nadir, Haddou El Ghazi, Anouar Jorio, Izeddine Zorkani, and Hamdi Şükür Kiliç, "Intersubband optical absorption in (In, Ga) N/GaN double quantum wells considering applied electric field effects", *Journal of Computational Electronics* 21.1 (2022), pp. 111–118. DOI: https://doi.org/10.1007/s10825-021-01830-4.

[32] Y Fu, M Willander, and Wenlan Xu, "Optical absorption coefficients of semiconductor quantum-well infrared detectors", *Journal of applied physics* 77.9 (1995), pp. 4648–4654. URL: https://doi.org/10.1063/1.359432.

[33] Mohamed Hichem Gazzah, Bilel Chouchen, Abdelaali Fargi, and Hafedh Belmabrouk, "Electro-thermal modeling for InxGa1-xN/GaN based quantum well heterostructures", *Materials Science in Semiconductor Processing* 93 (2019), pp. 231–237. URL: https://doi.org/10.1016/j.mssp.2019.01.011.

[34] Bernard Gil, *Physics of Wurtzite Nitrides and Oxides*. Vol. 197. Springer, 2014. URL: https://doi.org/10.1007/978-3-319-06805-3.

[35] Bernard Gil, Pierre Lefebvre, and Hadis Morkoç, "Strain effects in GaN epilayers", *Comptes Rendus de l'Académie des Sciences-Series IV-Physics* 1.1 (2000), pp. 51–60. URL: https://doi.org/10.1016/S1296-2147(00)00101-3.

[36] Claire Gmachl, Hock M Ng, and Alfred Y Cho, "Intersubband absorption in degenerately doped GaN/Al x Ga 1- x N coupled double quantum wells", *Applied Physics Letters* 79.11 (2001), pp. 1590–1592. URL: https://doi.org/10.1063/1.1403277.

[37] M Goyal and M Singh, "Size and shape dependence of optical properties of nanostructures", *Applied Physics A* 126.3 (2020), pp. 1–8. URL: 10.1007/s00339-020-3327-9.

[38] T Hanada, "Basic properties of ZnO, GaN, and related materials", *Oxide and nitride semiconductors*. Springer, 2009, pp. 1–19. URL: https://doi.org/10.1007/978-3-540-88847-5_1.

[39] F Hartmann-Boutron, "Interactions de superéchange en présence de dégénérescence orbitale et de couplage spin-orbite", *Journal de Physique* 29.2-3 (1968), pp. 212–214. URL: https://hal.archives-ouvertes.fr/jpa-00206638.

[40] David Holec, Yucheng Zhang, DV Sridhara Rao, Menno J Kappers, Clifford McAleese, and Colin J Humphreys, "Equilibrium critical thickness for misfit dislocations in III-nitrides", *Journal of Applied Physics* 104.12 (2008), p. 123514. DOI: https://doi.org/10.1063/1.3033553.

[41] L Hsu and W Walukiewicz, "Modeling of InGaN/Si tandem solar cells", *Journal of Applied Physics* 104.2 (2008), p. 024507. DOI: https://doi.org/10.1063/1.2952031.

[42] SC Jain, A Nathan, DR Briglio, DJ Roulston, CR Selvakumar, and T Yang, "Band-to-band and free-carrier absorption coefficients in heavily doped silicon at 4 K and at room temperature", *Journal of applied physics* 69.6 (1991), pp. 3687–3690. URL: https://doi.org/10.1063/1.348485.

[43] Khalil Ebrahim Jasim, "Quantum Dots Solar Cells", *Solar Cells*. Ed. by Leonid A. Kosyachenko. Rijeka: IntechOpen, 2015. Chap. 11. DOI: 10.5772/59159.

[44] Warren C Johnson, JB Parson, and MC Crew, "Nitrogen compounds of gallium. iii", *The journal of physical chemistry* 36.10 (2002), pp. 2651–2654. DOI: https://doi.org/10.1021/j150340a015.

[45] Eli Kapon, *Semiconductor lasers I: fundamentals*. Academic Press, 1999. URL: https://www.sciencedirect.com/topics/engineering/quantum-confinement.

[46] İbrahim Karabulut and Sotirios Baskoutas, "Linear and nonlinear optical absorption coefficients and refractive index changes in spherical quantum dots: Effects of impurities, electric field, size, and optical intensity", *Journal of Applied Physics* 103.7 (2008), p. 073512. URL: https://doi.org/10.1063/1.2904860.

[47] MJ Karimi, A Keshavarz, and A Poostforush, "Linear and nonlinear intersubband optical absorption and refractive index changes of asymmetric double semi-parabolic quantum wells", *Superlattices and Microstructures* 49.4 (2011), pp. 441–452. URL: https://doi.org/10.1016/j.spmi.2011.01.003.

[48] ESİN Kasapoglu, FATİH Ungan, CA Duque, U Yesilgul, ME Mora-Ramos, HÜSEYİN Sari, I So, et al., "The effects of the electric and magnetic fields on the nonlinear optical properties in the step-like asymmetric quantum well", *Physica E: Low-dimensional Systems and Nanostructures* 61 (2014), pp. 107–110. URL: https://doi.org/10.1016/j.physe.2014.03.024.

[49] Eduard M Kazaryan, Artavazd A Kostanyan, and Hayk A Sarkisyan, "Impurity optical absorption in parabolic quantum well", *Physica E: Low-dimensional Systems*

and Nanostructures 28.4 (2005), pp. 423–430. URL: https://doi.org/10.1016/j.physe.2005.05.047.

[50] A Keshavarz and MJ Karimi, "Linear and nonlinear intersubband optical absorption in symmetric double semi-parabolic quantum wells", *Physics Letters A* 374.26 (2010), pp. 2675–2680. URL: https://doi.org/10.1016/j.physleta.2010.04.049.

[51] Ig-Hyeon Kim, Hyeong-Soo Park, Yong-Jo Park, and Taeil Kim, "Formation of V-shaped pits in InGaN/GaN multiquantum wells and bulk InGaN films", *Applied physics letters* 73.12 (1998), pp. 1634–1636. DOI: https://doi.org/10.1063/1.122229.

[52] Philip Kim, Li Shi, Arun Majumdar, and Paul L McEuen, "Thermal transport measurements of individual multiwalled nanotubes", *Phys. Rev. Lett.* 87.21 (2001), p. 215502. URL: https://doi.org/10.1063/1.4829674.

[53] SY Lei, ZG Dong, B Shen, and GY Zhang, "Intersubband transition in symmetric AlxGa1- xN/GaN double quantum wells with applied electric field", *Physics Letters A* 373.1 (2008), pp. 136–139.

[54] Caroline Botum Lim, "GaN/AlGaN heterostructures for infrared optoelectronics: polar vs nonpolar orientations". PhD thesis. Université Grenoble Alpes, 2017. DOI: https://tel.archives-ouvertes.fr/tel-01693891.

[55] Caroline Botum Lim, "Hétérostructures GaN/Al (Ga) N pour l'optoélectronique infrarouge: orientations polaires et non-polaires". PhD thesis. Université Grenoble Alpes (ComUE), 2017. URL: https://tel.archives-ouvertes.fr/tel-01693891.

[56] CJ Lu, Leonid A Bendersky, Hai Lu, and William J Schaff, "Threading dislocations in epitaxial InN thin films grown on (0001) sapphire with a GaN buffer layer", *Applied physics letters* 83.14 (2003), pp. 2817–2819. DOI: https://doi.org/10.1063/1.1616659.

[57] H Pi Maruska and JJ Tietjen, "The preparation and properties of vapor-deposited single-crystal-line GaN", *Applied Physics Letters* 15.10 (1969), pp. 327–329. DOI: https://doi.org/10.1063/1.1652845.

[58] Takashi Matsumoto and Masaharu Aoki, "Temperature dependence of photoluminescence from GaN", *Japanese Journal of Applied Physics* 13.11 (1974), p. 1804. URL: \url{https://doi.org/10.1143/JJAP.13.1804}.

[59] Hadis Morkoç, *Handbook of Nitride Semiconductors and Devices, Electronic and Optical Processes in Nitrides*. John Wiley & Sons, 2009.

[60] Anna Mukhtarova, "InGaN/GaN multiple quantum wells for photovoltaics". PhD thesis. Université Grenoble Alpes, 2015. DOI: https://tel.archives-ouvertes.fr/tel-01159686/.

[61] Anna Mukhtarova, "InGaN/GaN multiple quantum wells for photovoltaics". PhD thesis. Université Grenoble Alpes, 2015. DOI: https://tel.archives-ouvertes.fr/tel-01159686/.

[62] Shuji Nakamura, Naruhito Iwasa, Masayuki Senoh Masayuki Senoh, and Takashi Mukai Takashi Mukai, "Hole compensation mechanism of p-type GaN films", *Japanese Journal of Applied Physics* 31.5R (1992), p. 1258. DOI: https://doi.org/10.1143/JJAP.31.1258.

[63] Shuji Nakamura, Takashi Mukai, Masayuki Senoh Masayuki Senoh, and Naruhito Iwasa Naruhito Iwasa, "Thermal annealing effects on p-type Mg-doped GaN films", *Japanese Journal of Applied Physics* 31.2B (1992), p. L139. DOI: https://doi.org/10.1143/JJAP.31.L139.

[64] Shuji Nakamura, Masayuki Senoh, Naruhito Iwasa, Shin-ichi Nagahama, Takao Yamada, and Takashi Mukai, "Superbright green InGaN single-quantum-well-structure light-emitting diodes", *Japanese Journal of Applied Physics* 34.10B (1995), p. L1332. DOI: https://doi.org/10.1143/JJAP.34.L1332.

[65] Shuji Nakamura Shuji Nakamura and Takashi Mukai Takashi Mukai, "High-quality InGaN films grown on GaN films", *Japanese journal of applied physics* 31.10B (1992), p. L1457. DOI: https://doi.org/10.1143/JJAP.31.L1457.

[66] Seoung-Hwan Park, Doyeol Ahn, and Chan-Yong Park, "Intersubband absorption coefficients of GaN/AlN and strain-compensated InGaN/InAlN quantum well structures", *Superlattices and Microstructures* 100 (2016), pp. 508–513. URL: https://doi.org/10.1016/j.spmi.2016.10.001.

[67] XG Peralta et al., "Terahertz photoconductivity and plasmon modes in double-quantum-well field-effect transistors", *Applied Physics Letters* 81.9 (2002), pp. 1627–1629. DOI: https://doi.org/10.1063/1.1497433.

[68] Michael T Pettes and Li Shi, "Thermal and Structural Characterizations of Individual Single-, Double-, and Multi-Walled Carbon Nanotubes", *Adv. Funct. Mater.* 19.24 (2009), pp. 3918–3925.

[69] Adrien Robin, "Opto-électronique de boîtes et puits quantiques colloïdaux-Application au photo-transport". PhD thesis. Université Pierre et Marie Curie-Paris VI, 2016. URL: https://tel.archives-ouvertes.fr/tel-01512629.

[70] AE Romanov, TJ Baker, S Nakamura, and JS Speck, "ERATO/JST UCSB Group", *J. Appl. Phys* 100 (2006), p. 023522. URL: https://doi.org/10.1063/1.2218385.

[71] Daniel Rosales, "Etude des propriétés optiques de nanostructures quantiques semi-polaires et non-polaires à base de nitrure de gallium (GaN)". PhD thesis. Université Montpellier, 2015. URL: \url{https://tel.archives-ouvertes.fr/tel-02024725}.

[72] E Rosencher and B Vinter, *Optoélectronique Masson*. 1998.

[73] A Sali, M Fliyou, H Satori, and H Loumrhari, "The effect of a strong magnetic field on the binding energy and the photoionization process in quantum-well wires", *Journal of Physics and Chemistry of Solids* 64.1 (2003), pp. 31–41. URL: https://doi.org/10.1016/S0022-3697(02)00205-6.

[74] RD Shannon, "Shannon RD & Prewitt C T. Effective ionic radii in oxides and fluorides. Acta Crystallogr. B 25: 925-46, 1969.[Central Research Dept. Experimental Station, EI Du Pont de Nemours and Co., Wilmington, DE and Dept. Earth and Space Sci., SUNY, Stony Brook, NY]", *Acta Crystallogr. B* 25 (1969), pp. 925–46. URL: http://www.garfield.library.upenn.edu/classics1981/A1981LP44500001.pdf.

[75] Kun-Ching Shen, Tzu-Yu Wang, Dong-Sing Wuu, and Ray-Hua Horng, "High indium content InGaN films grown by pulsed laser deposition using a dual-compositing target", *Optics express* 20.14 (2012), pp. 15149–15156. DOI: https://doi.org/10.1364/OE.20.015149.

[76] H Teisseyre et al., "Temperature dependence of the energy gap in GaN bulk single crystals and epitaxial layer", *Journal of applied physics* 76.4 (1994), pp. 2429–2434. URL: \url{https://doi.org/10.1063/1.357592}.

[77] Jessica Thery, "Elaboration par MOCVD à injection pulsée d'oxydes de fer et de BIFEO3". PhD thesis. Université Joseph-Fourier-Grenoble I, 2006. URL: \url{https://tel.archives-ouvertes.fr/tel-00105575}.

[78] Nikholas G Toledo et al., "Design of integrated III-nitride/non-III-nitride tandem photovoltaic devices", *Journal of Applied Physics* 111.5 (2012), p. 054503. DOI: https://doi.org/10.1063/1.3690907.

[79] Lars Vegard, "Die konstitution der mischkristalle und die raumfüllung der atome", *Zeitschrift für Physik* 5.1 (1921), pp. 17–26. URL: \url{https://doi.org/10.1007/BF01349680}.

[80] Philippe Vennéguès, "Propriétés structurales de films de semi-conducteurs wurtzite hetéroépitaxiés selon des orientations non-et semi-polaires". PhD thesis. Université Nice Sophia Antipolis, 2009. URL: \url{https://tel.archives-ouvertes.fr/tel-00520457}.

[81] Guang-Hui Wang and Jin-Ke Zhang, "Optimizing effective phase modulation in coupled double quantum well Mach–Zehnder modulators", *Chinese Physics B* 27.2 (2018), p. 027801. URL: https://doi.org/10.1088/1674-1056/27/2/027801.

[82] Yongjin Wang, Fangren Hu, and Kazuhiro Hane, "Patterned growth of InGaN/GaN quantum wells on freestanding GaN grating by molecular beam epitaxy", *Nanoscale research letters* 6.1 (2011), pp. 1–7. URL: https://doi.org/10.1186/1556-276X-6-117.

[83] *WebSite, data base of relevant proprieties of semiconductor materials*. Last access:07/09/2021. URL: http://thepoussin.free.fr/TPE2003/TPE.htm.

[84] Benjamin S Williams, "Terahertz quantum-cascade lasers", *Nature photonics* 1.9 (2007), pp. 517–525. URL: https://doi.org/10.1038/nphoton.2007.166.

[85] J Wu, W Walukiewicz, K_M Yu, JW Ager III, EE Haller, Hai Lu, and William J Schaff, "Small band gap bowing in In 1- x Ga x N alloys", *Applied Physics Letters* 80.25 (2002), pp. 4741–4743. DOI: https://doi.org/10.1063/1.1489481.

[86] J Wu et al., "Superior radiation resistance of In 1- x Ga x N alloys: Full-solar-spectrum photovoltaic material system", *Journal of Applied Physics* 94.10 (2003), pp. 6477–6482. DOI: https://doi.org/10.1063/1.1618353.

[87] U Yesilgul, "Linear and nonlinear intersubband optical absorption coefficients and refractive index changes in symmetric double semi-V-shaped quantum wells", *Journal of luminescence* 132.3 (2012), pp. 765–773. URL: https://doi.org/10.1016/j.jlumin.2011.10.016.

[88] U Yesilgul et al., "Linear and nonlinear optical properties in an asymmetric double quantum well under intense laser field: Effects of applied electric and magnetic fields", *Optical Materials* 58 (2016), pp. 107–112. URL: https://doi.org/10.1016/j.optmat.2016.03.043.

[89] H Yoshida, T Mozume, A Neogi, and O Wada, "Ultrafast all-optical switching at 1.3/spl mu/m/1.55/spl mu/m using novel InGaAs-AlAsSb-InP coupled double quantum well structure for intersubband transitions", *Electronics Letters* 35.13 (1999), pp. 1103–1105. URL: https://doi.org/10.1016/j.physe.2011.09.023.

[90] Mouna Zouaoui, "Etude des propriétés électroniques des boîtes quantiques InAs/InP par spectroscopie de défauts profonds (DLTS) pour des applications optoélectroniques". PhD thesis. INSA de Lyon, 2013. URL: https://tel.archives-ouvertes.fr/tel-01066429.

[91] Radoslaw Zwierz, "Plasma enhanced growth of GaN single crystalline layers from vapour phase". PhD thesis. BTU Cottbus-Senftenberg, 2014. DOI: urn:nbn:de:kobv:co1-opus4-30710.

Appendix A

Numerical method and approaches

A.1 Finite difference method or FDM

In this appendix, we will give a detailed overview of the numerical calculation of one-dimensional Schrodinger equation in low-dimensional systems (or nanostructured) [Fig.A.2]. In some complicated cases, the Schrodinger equation is not easily solved manually because it has first and second order partial derivatives. so that, the finite difference method is one of the approaches proposed to solve this kind of problem. In numerical analysis, **finite-difference method (FDM)** is a class of numerical techniques for solving differential equations by approximating derivatives with finite differences. Both the spatial domain and time interval (if applicable) are discretized, or broken

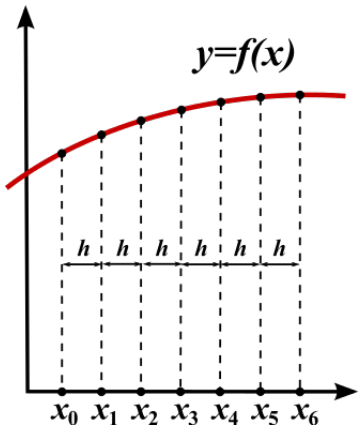


FIGURE A.1: The finite difference method relies on discretizing a function on a grid.
Ref:https://en.wikipedia.org/wiki/Finite_difference_method

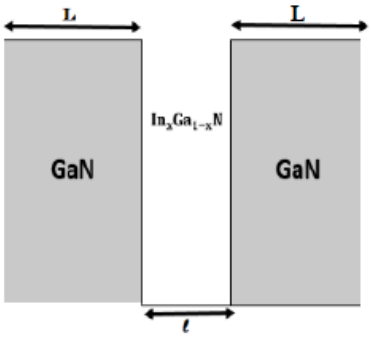


FIGURE A.2: A schematic representation of a single quantum well (SQW) made out of InGaN (well region) and GaN (barriers region).

into a finite number of steps, and the value of the solution at these discrete points is approximated by solving algebraic equations containing finite differences and values from nearby points [Fig.A.1].

A.2 Numerical solution of the uni-dimensional Schrodinger's equation

In the framework of the approximation of the effective mass and the nonparablity, the Hamiltonian of an electron confined along the growth axis (z) while it is capable of moving freely in the plane (xOy) is given as follows :

$$H = \frac{P^2}{2m^*} + V_c(z) \tag{A.1}$$

where $V_c(z)$ is the confinement potential along the growth direction (z-axes).
If we look at the Fig.A.2, we conclude that the Schrodinger must be solved in three different regions:

1. **In the barrier region**
2. **In the well region**
3. **In the interfaces region**

A.2.1 Case 1: In the barrier region (GaN)

In this region the confinement potential is not zero ($V_c = V_0$):

The Schrodinger equation that gives the egenvectors and their associated eigenvalues is given as fellows[Eq.A.2],

$$\left(-\frac{\hbar^2}{2m^*}\frac{\partial^2}{\partial z^2}\right)\psi(z) + V_c(z)\psi(z) = E\psi(z) \tag{A.2}$$

Now, Lets consider a mono-directional mesh (calculation grid) of 5N+1 points is considered and each layer (Well, barrier) is characterized by a different discretization step. $h_w = l/N$ and $h_b = L/N$ are used to characterize respectively the well, intermediate (central) barrier and left and right barriers. Therefore, the mesh's nodes of the studied structure are given respectively as $z_i = i * h_b, z_i = L + i * h_w, z_i = L + l + i * h_b$ for $0 < i < N$.

Assuming the function whose derivatives are to be approximated is properly-behaved, by Taylor's theorem. In 1D the Laplace operators are approximated as:

$$\left(\frac{\partial^2\psi(z)}{\partial z^2}\right)_{z=z_i} = \frac{\psi_{i-1} - 2\psi_i + \psi_{i+1}}{(z_{i+1} - z_i)^2}, \tag{A.3a}$$

$$\left(\frac{\partial\psi(z)}{\partial z}\right)_{z=z_i} = \frac{\psi_{i+1} - \psi_i}{(z_{i+1} - z_i)}, \tag{A.3b}$$

If we assume that $h_b = z_{i+1} - z_i$, the Eq.A.2 becomes as fellows:

$$\left(-\frac{\hbar^2}{2m^*}\right)\left[\frac{\psi_{i-1} - 2\psi_i + \psi_{i+1}}{h_b^2}\right] + V_0\psi_i = E\psi_i \tag{A.4}$$

Lets assume that $\Omega = -\frac{\hbar^2}{2m^*h_b^2}$. Thus, the Eq.A.5 becomes as fellwos,

$$\Omega\left[\psi_{i-1} + \psi_{i+1} + \left(\frac{V_0}{\Omega} - 2\right)\psi_i\right] = E\psi_i \tag{A.5}$$

The matrix that gives us the energy levels and their correspondent wave-functions in this particular region (barrier-region) can then be written as (Eq.A.6):

$$M_{Barrier} = \begin{pmatrix} 0 & 0 & 0 & 0 & 0 & 0 \\ \Omega & (V_0 - 2\Omega) & \Omega & 0 & 0 & 0 \\ 0 & \Omega & (V_0 - 2\Omega) & \Omega & 0 & 0 \\ 0 & 0 & 0 & 0 & \ddots & \vdots \\ 0 & 0 & 0 & 0 & 0 & \cdots \\ 0 & 0 & 0 & 0 & 0 & 0 \end{pmatrix} \tag{A.6}$$

A.2.2 Case 2: In the well region (InGaN)

In this region, we will applied the same principle that was applied in the case of barrier region (GaN) except that inside the well the confinement potential is zero ($V_c = 0$): Thus, the Eq.A.2 becomes as fellows (Eq.A.7),

$$\left(-\frac{\hbar^2}{2m^*}\frac{\partial^2}{\partial z^2}\right)\psi(z) = E\psi(z) \tag{A.7}$$

If we assume that $h_w = z_{i+1} - z_i$, and substituting Eq.A.3a in Eq. A.7, we get the the following equation (Eq.A.8):

$$\left(-\frac{\hbar^2}{2m^*}\right)\left[\frac{\psi_{i-1} - 2\psi_i + \psi_{i+1}}{h_w^2}\right] = E\psi_i \tag{A.8}$$

Now, lets assume that $\chi = -\frac{\hbar^2}{2m^* h_{w^2}}$, then the Eq.A.8 becomes as fellows (Eq.A.9):

$$\chi\left[\psi_{i-1} - 2\psi_i + \psi_{i+1}\right] = E\psi_i \tag{A.9}$$

So that, the matrix that gives us the energy levels and their correspondent wave-functions in this particular region (well-region) can then be written as (Eq.A.10):

$$M_{Well} = \begin{pmatrix} 0 & 0 & 0 & 0 & 0 & 0 \\ \chi & -2\chi & \chi & 0 & 0 & 0 \\ 0 & \chi & -2\chi & \chi & 0 & 0 \\ 0 & 0 & 0 & 0 & \ddots & \vdots \\ 0 & 0 & 0 & 0 & 0 & \cdots \\ 0 & 0 & 0 & 0 & 0 & 0 \end{pmatrix} \tag{A.10}$$

A.2.3 Case 3: At the interface between well/barrier (GaN/InGaN)

At the interface between two different semiconductors e.g. GaN and InGaN, the electron wave functions are not continued, so to ensure their continuity it is necessary to take into account the boundary conditions. The continuity of the wave functions and the probability current according to [8] are given by (Eqs.(A.11a),(A.11b)).

$$\psi_b(l) = \psi_w(l), \tag{A.11a}$$

$$\frac{1}{m_b^*}\left(\psi_b{}'\right)_{z=l} = \frac{1}{m_w^*}\left(\psi_w{}'\right)_{z=l}, \tag{A.11b}$$

with b denotes the barrier material (GaN) while w the well material (InGaN).
Now, lets use the second order Taylor's limited development near to l ($z \to l$):

$$\psi_b(l-h_b) = \psi_b(l) - h_b\left(\psi_b{}'\right)_{z=l} + \frac{h_b^2}{2!}\left(\psi_b{}''\right)_{z=l} + \cdots + \Theta(z^n), \tag{A.12a}$$

$$\psi_w(l+h_w) = \psi_w(l) + h_w\left(\psi_w{}'\right)_{z=l} + \frac{h_w^2}{2!}\left(\psi_w{}''\right)_{z=l} + \cdots + \Theta(z^n), \tag{A.12b}$$

Hence, from Eqs.(A.12a, A.12a), we get:

$$\frac{1}{m_b^*}\left(\psi_b{}'\right)_{z=l} = \frac{1}{m_b^* h_b}\left[\psi_b(l) - \psi_b(l-h_b) + \frac{h_b^2}{2!}\left(\psi_b{}''\right)_{z=l}\right], \tag{A.13a}$$

$$\frac{1}{m_w^*}\left(\psi_b{}'\right)_{z=l} = \frac{1}{m_w^* h_w}\left[\psi_w(l+h_w) - \psi_w(l) - \frac{h_w^2}{2!}\left(\psi_w{}''\right)_{z=l}\right], \tag{A.13b}$$

By the applying of the boundary condition given by Eq.A.11b, we get the following expression:

$$\left(\psi_w{}''\right)_{z=l}\left(\frac{h_b^2}{2} + \frac{m_b^* h_b}{m_w^* h_w}\frac{h_w^2}{2}\right) = \frac{m_b^* h_b}{m_w^* h_w}\left[\psi_w(l+h_w) - \psi_w(l)\right] - \psi_b(l) + \psi_b(l-h_b) \tag{A.14}$$

Now, using the boundary condition given by Eq.A.11a ($\psi_w(l) = \psi_b(l)$), and assume that $A = \frac{h_b^2}{2} + \frac{m_b^* h_b}{m_w^* h_w}\frac{h_w^2}{2}$, and $B = \frac{m_b^* h_b}{m_w^* h_w}$, the Eq.A.14 becomes as fellows:

$$\left(\psi_w{}''\right)_{z=l} = \frac{B}{A}\left[\psi_w(l+h_w) - \psi_w(l)\right] + \frac{1}{A}\left[-\psi_w(l) + \psi_b(l-h_b)\right] \tag{A.15}$$

Thus, after simplification, the Eq.A.15 becomes then as fellows:

$$(\psi_w{}'')_{z=l} = \frac{B}{A}\psi_w(l+h_w) + \frac{1}{A}\psi_b(l-h_b) - \psi_w(l)\left[\frac{B}{A}+\frac{1}{A}\right] \tag{A.16}$$

So that, the matrix that gives us the energy levels and their correspondent wave-functions in this particular region (interfaces) can then be written as (Eq.A.17):

$$M_{Interface} = \begin{pmatrix} 0 & 0 & 0 & 0 & 0 & 0 \\ \frac{1}{A} & -\left(\frac{B+1}{A}\right) & \frac{B}{A} & 0 & 0 & 0 \\ 0 & \frac{1}{A} & -\left(\frac{B+1}{A}\right) & \frac{B}{A} & 0 & 0 \\ 0 & 0 & 0 & 0 & \ddots & \vdots \\ 0 & 0 & 0 & 0 & 0 & \cdots \\ 0 & 0 & 0 & 0 & 0 & 0 \end{pmatrix} \tag{A.17}$$

Finally, the matrix of the system can be given as the sum of the three defined before. Lets assume that:

$$\alpha = \left(\Omega + \chi + \frac{1}{A}\right),$$

$$\beta = \left[V_0 - 2\Omega - \left(2\chi + \frac{B+1}{A}\right)\right],$$

and

$$\delta = \left(\Omega + \chi + \frac{B}{A}\right)$$

$$M_{System} = \begin{pmatrix} 0 & 0 & 0 & 0 & 0 & 0 \\ \alpha & \beta & \delta & 0 & 0 & 0 \\ 0 & \alpha & \beta & \delta & 0 & 0 \\ 0 & 0 & 0 & 0 & \ddots & \vdots \\ 0 & 0 & 0 & 0 & 0 & \cdots \\ 0 & 0 & 0 & 0 & 0 & 0 \end{pmatrix} \tag{A.18}$$

Example: If we considered a number of discretization ($N = 6$) and taken into account that the electron wave-functions are zero at the edges, the matrix above (A.18) becomes as fellows:

$$\begin{pmatrix} 0 & 0 & 0 & 0 & 0 & 0 \\ \alpha & \beta & \delta & 0 & 0 & 0 \\ 0 & \alpha & \beta & \delta & 0 & 0 \\ 0 & 0 & \alpha & \beta & \delta & 0 \\ 0 & 0 & 0 & \alpha & \beta & \delta \\ 0 & 0 & 0 & 0 & 0 & 0 \end{pmatrix} \begin{pmatrix} \psi_1 \\ \psi_2 \\ \psi_3 \\ \psi_4 \\ \psi_5 \\ \psi_6 \end{pmatrix} = \begin{pmatrix} E_1 \\ E_2 \\ E_3 \\ E_4 \\ E_5 \\ E_6 \end{pmatrix} \begin{pmatrix} \psi_1 \\ \psi_2 \\ \psi_3 \\ \psi_4 \\ \psi_5 \\ \psi_6 \end{pmatrix} \tag{A.19}$$

where ψ_n and E_n are the wave-functions and their associated energy-levels, respectively.

Remark: In this appendix, the calculations are performed without neither normalization nor calibration.

A.3 Software: *Python*

The numerical calculations to obtain the eigenvalues and their correspondent eigenvectors are performed using *Python* programming language. This Software can be used in numerical calculation using the most important numerical packages such as (*NumPy*, *SciPy*, *Matplotlib*, $\cdots$).

Exemple: The following figure [Fig.A.3] gives an exemple of a single quantum well (SQW).

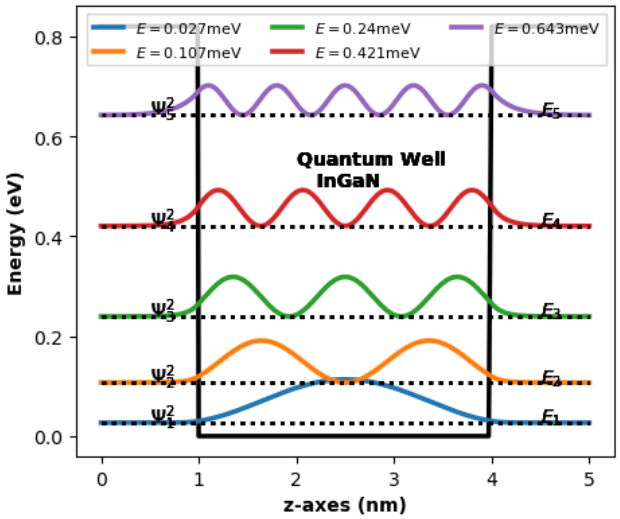


FIGURE A.3: Energy-levels of the first six-levels and their associated wave-functions in symmetric single InGaN/GaN quantum well.

List of publications and conferences

I Publications

I.1 Articles in peer-reviewed journals

1. Haddou El-Ghazi, **Redouane En-nadir**, Hassan Abboudi, Fathallah Jabouti, Anouar Jorio, and Izeddine Zorkani, *Two-dimensional electron gas modeling in strained InN/GaN hetero-interface under pressure and impurity effects*, Physica B: Condensed Matter(Elsevier); 582, 411951 (**2020**).
   [URL: https://doi.org/10.1016/j.physb.2019.411951].

2. **Redouane En-nadir**, Haddou El-ghazi,Walid Belaid, Anouar Jorio, Izeddine Zorkani, and Hamdi Şükür Kiliç, *Ground and first five low-lying excited states related optical absorption in $In_{0.1}Ga_{0.9}N$/GaN double quantum wells: Temperature and coupling impacts*, Solid State Communications(Elsevier), 2021, 114464 (**2021**).
   [URL: https://doi.org/10.1016/j.ssc.2021.114464]. (Chapter 3)

3. **Redouane En-nadir**, Haddou El-Ghazi, Walid Belaid, Anouar Jorio, and Izeddine Zorkani, *Intraconduction band-related optical absorption in coupled (In,Ga)N/GaN double parabolic quantum wells under temperature, coupling and composition effects*, Results in Optics (Elsevier); 2021, 100154 (**2021**).
   [URL: https://doi.org/10.1016/j.rio.2021.100154]. (Chapter 4)

4. **Redouane En-nadir**, Haddou El-Ghazi, Anouar Jorio, and Izeddine Zorkani, *Ground-state Shallow-donor Binding Energy in (In, Ga) N/GaN Double QWs Under Temperature, Size, and the Impurity Position Effects*, Journal of Modeling and Simulation of Materials (AJIR);4,1, 1-6 (**2021**).
   [URL: https://doi.org/10.21467/jmsm.4.1.1-6].

5. Fathallah Jabouti, Haddou El-Ghazi, **Redouane En-nadir**, Anouar Jorio, and Izeddine Zorkani, *Excitonic States and Related Optical Susceptibility in InN/AlN Quantum*

Well Under the Effects of the Well Size and Impurity Position, Advanced Nano Research (AJIR);4,1, 1-9 (**2021**).
[URL: https://doi.org/10.21467/anr.4.1.1-9].

6. Hassan Abboudi, Haddou El-Ghazi, Farid benhaddou, **Redouane En-nadir**, Anouar Jorio, and Izeddine Zorkani, *Temperature-related photovoltaic characteristics of (In,Ga)N single-intermediate band quantum well solar cells for different shapes*, Physica B: Condensed Matter (Elsevier), 413495, November 22 (**2021**).
[URL: https://doi.org/10.1016/j.physb.2021.413495].

7. **Redouane En-nadir**, Haddou El-ghazi, Anouar Jorio, Izeddine Zorkani, and Hamdi Şükür Kiliç, *Intersubband optical absorption in (In,Ga)N/GaN double quantum wells considering applied electric field effects*, Journal of Computational Electronics (Springer nature), 2022, 114464 (**2022**).
[URL: https://doi.org/10.1007/s10825-021-01830-4]. (Chapter 5)

8. **Redouane En-nadir**, Haddou El Ghazi, Walid Belaid, Hassan Abboudi, Fath allah Jabouti, Anouar Jorio, Izeddine Zorkani, *The Confinement Profile Effect on the Optical Properties in Different Inverse-shaped Single InGaN/GaN Quantum Wells*, Iraqi journal of physics (University of Baghdad), 20(1),1-13 (**2022**).
[URL: https://doi.org/10.30723/ijp.v20i1.965].

9. **Redouane En-nadir**, Haddou El Ghazi, Anouar Jorio, Izeddine Zorkani, Hassan Abboudi and Fath allah Jabouti, *Numerical Study of Temperature and Electric Field Effects on the Total Optical Absorption Coefficient Related-Conduction-Subband Optical Transitions in InGaN/GaN Single Parabolic QW*, fdmp-fluid dynamics and materials processing (Tech Science Press), 20(1),021759 (**2022**).
[URL: 10.32604/fdmp.2022.021759]

I.2 Articles in peer-reviewed conference proceedings

1. **Redouane En-nadir**, Haddou El Ghazi, Anouar Jorio, Izeddine Zorkani, *Inter and intra band impurity-related absorption in (In,Ga)N/GaN QW under composition, size and impurity effects*, MATEC Web of Conferences 330,01017 (2020), International

Conference on MATERIALS ENERGY (ICOME'19), Metz, France.
[URL: https://doi.org/10.1051/matecconf/202033001017]. (Chapter 2)

II Conferences

II.1 Oral Presentations

1. **Redouane En-nadir**, Haddou El Ghazi, *"Pure theoretical investigation of optical absorption phenomena in artificial nanocristals from iii-nitride (In, Ga)N elements for energy conversion applications and optoelectronic devices"*, **IBSCCS'21**, 7th International Black Sea Coastline Countries Symposiums, November 27-29, 2021 / University of Geography, Bucharest,Romania.
[URL: https://www.blackseacountries.org/symposium].

2. **Redouane En-nadir**, Haddou El Ghazi, *"The optical absorption phenomena in nanostructures based on III-Nitride elements (In,Ga)N for energy conversion and optoelectronic devices applications"*, **ICISA'21**, 6th International Congress on Innovative Scientific Approaches, December 19-20, 2021 / University of Samsun, Samsun, Turkey.
[URL: https://www.19mayis.org/].

3. **Redouane En-nadir**, Haddou El Ghazi, *"Modeling and Simulation of the Optical Transitions in Multi-Quantum-Wells in InGaN/GaN Using Finite Difference Method."*, **IMSRC'21**, Istanbul International Modern Scientific Research Congress, June 4-5, 2021 / University of Istanbul, Turkey.
[URL: https://www.istanbulkongresi.org/].

4. **Redouane En-nadir**, Haddou El Ghazi, Anouar Jorio, Izeddine Zorkani, Walid Belaid, *"Combined effects of coupling and band-edge nonparabolicity on linear, nonlinear and total optical absorption of (In,Ga)N-GaN multiple QW taking account an on center impurity-related."*, **N@NO'18**, 1^{st} International online conference on Nanosciences and Nanotechnology, held on December 29-30, 2018/ University of Johannesburg, South Africa.
[URL: http://www.proceedings.com/51003.html].

5. **Redouane En-nadir**, Haddou El Ghazi, Walid Belaid, *"Inter and Intra Band Absorption in (In,Ga)N/GaN QW under Composition, Size, and Impurity positions Effects."*, **IRSEC'20**, 8^{th} International Renewable and Sustainable Energy Conference (IRSEC'20), which is organized virtually via video conferencing application, November 25-28, 2020, University of Abdelmalek Essaâdi, Tetouan, Morocco (32 course hours).
   [URL: http://www.med-space.org/irsec20/].

6. **Redouane En-nadir**, Haddou El Ghazi, Anouar Jorio, Izeddine Zorkani, *"The Impact of Temperature, Size, and In-composition on the Total Optical Absorption Coefficient in Parabolic InGaN/GaN Double coupled QWs.."*, **EJONS**, Ejons 11^{th} International Conference on Mathematical, Engineering, Material and Medical Sciences, January 30-31, 2021/Mutah University, Karak, Jordan.
   [URL: https://en.iksadkongre.org/blank-1].

7. **Redouane En-nadir**, Haddou El Ghazi, Anouar Jorio, Izeddine Zorkani, *"Combined effects of size and temperature on the linear and nonlinear optical absorption coefficients in asymmetric InGaN/GaN coupled QWs."*, **ICONTECH**, International ICONTECH SYMPOSIUM-4 on Innovative Surveys in Positive Sciences July 18-19, 2021/Adana Institute of technology, Adana, Turkey.
   [URL: https://www.icontechsurveys.org/symposiumbooks].

8. **Redouane En-nadir**, Haddou El Ghazi, Anouar Jorio, Izeddine Zorkani, *"Different optical transitions in single parabolic QW made out of InGaN/GaN under the effects of temperature, size, and indium compositions."*, **ICOME'20**, International Conference On Materials and Energy ICOME2021"holded from June 9^{th} to 11th 2021 in The University of Lourraine, Metz, France.
   [URL: http://www.icome.ecam-epmi.fr/].

9. **Redouane En-nadir**, Haddou El Ghazi, *"Ground-state shallow donnor binding energy in (In,Ga)N/GaN Double coupled QWs under temperature, size, and impurity position effects."*, **AEGEANS**, International Aegean Symposium on Innovation Technologies and Engineering March 12-13, 2021/Izmir Institute of technology, Izmir, Turkey.
   [URL: https://www.aegeanconference.com/].

10. **Redouane En-nadir**, Haddou El Ghazi, *"Subband optical transitions insymmetric double QWs Mmade out of InGaN/GAN under size and temperature effects."*, **BILTEK-IV**, 4^{th} International symposium on current development in science, technology and social sciences, April 12-13, 2021, Gaziantep University, Gazi, urkey.
[URL: https://en.biltek.org/].

11. **Redouane En-nadir**, Haddou El Ghazi, Anouar Jorio, Izeddine Zorkani, *"Impurity-related nonlinear optical absorption undercombined effects of coupling and band-edge nonparabolicity on InGaN multiple QW."*, **EVF'18**, 5^{th} Symposium international "Energy et Villes du Futur EVF'18", Octobre 25-26, 2018, University of Sidi Mohamed Ben Abdellah, Fez, Morocco.
[URL: http://www.fsdmfes.ac.ma/Conference/EVF2018/].

12. **Redouane En-nadir**, Haddou El Ghazi, Anouar Jorio, Izeddine Zorkani, *"Two-dimensional electron gas modeling un strained InN/GaNhetero-interface under pressure and impurity effects."*, **APIOC'20**, Advances in Physics International Online Conference, April 11-12, 2020, ICTP Institute , Triest, Italy.
[URL: https://apioc.e-master.org/].

II.2 Presentations by Poster

1. **Redouane En-nadir**, Haddou El Ghazi, *"Two-dimensional electron gas modeling (2DEG) in strained InN/GaNhetero-interface under pressure and impurity effects."*, **APIOC'20**, Advances in Physics International Online Conference, April 11-12, 2020, ICTP, Triest, Italy.
[URL: https://apioc.e-master.org/].

2. **Redouane En-nadir**, Haddou El Ghazi, Anouar Jorio, Izeddine Zorkani, *"Impurity-related nonlinear optical absorption undercombined effects of coupling and band-edge nonparabolicity on InGaN multiple QW."*, **EVF'18**, 5^{th} Symposium international "Energy et Villes du Futur EVF'18", Octobre 25-26, 2018, Fez, Morocco.
[URL: http://www.fsdmfes.ac.ma/Conference/EVF2018/].